Integration of manufacturing and structural design of 3D concrete printed bridges

MSc. Thesis
M. J. Hoogeveen

TUDelft

Witteveen + Bos

MSc. Thesis

Integration of manufacturing and structural design of 3D concrete printed bridges

by

M.J. Hoogeveen

in partial fulfillment of the requirements for the degree of

Master of Science
in Structural Engineering

at the Delft University of Technology,
to be defended publicly on August 24, 2020 at 15:00.

Student number:	4288459
Project duration:	November 13, 2019 - August 24, 2020
Thesis committee:	Dr. ir. M. A. N. Hendriks, Delft University of Technology
	Dr. ir. H. R. Schipper, Delft University of Technology
	Dr. ir. H. W. M. Van der Ham, Delft University of Technology
	M. J. A. M. Bruurs MSc., Witteveen+Bos

This thesis is confidential and cannot be made public until August 24, 2022.

Cover Photo by Ricardo Gomez Angel retrieved from unsplash.com

Witteveen+Bos

TUDelft

Preface

About a year ago I first read about 3D concrete printing and the topic immediately interested me. I decided to explore the world of 3D concrete printing for my graduation thesis, of which the final result is this research report. It has been an amazing journey which was sometimes challenging but exciting and I hope you will enjoy reading the final piece of work from me being a student.

Conducting this research alone would not have been possible and therefore I would like to thank some people. I want to express gratitude to my thesis committee for sharing their knowledge, giving advice and for making time to discuss the research progress. Except for the kick-off meeting, all of the committee meetings took place online from our home-offices, but I have definitely had great supervision and guidance from you. First of all Marijn Bruurs, thank you for all the discussions we have had, for answering all my questions and for involving me in the research going on at Witteveen+Bos. Thank you Max Hendriks for reading my work, for being critical and giving constructive feedback. Thank you Roel Schipper for your supportive feedback and for showing me the relevance of my research in the field of 3D concrete printing. Herbert van der Ham, thank you for your enthousiasm, keeping the research practical and for helping me with the design. Also special thanks to Izik Shalom for your support, for answering all of my questions and for reading my work. Thank you Hans Laagland for involving me in the team and helping me with the 3DCP bridge design. To anybody else from Witteveen+Bos whom I have met: thank you for anwering my questions and making me feel welcome at the office. Finally, I would like to thank my friends, family, roommates and Thomas for your big support and for making working at home during the Corona times fun.

Graduation means my time as a student in Delft has come to an end. Looking back, I think I can say it could not have been any better. I have learned so much, both on and off campus, and have met great people. I am proud to be an engineer from Delft and ready to start the next chapter of my life.

Maartje Hoogeveen
Rotterdam, August 2020

Summary

3D concrete printing (3DCP) is a new, innovative construction method in which concrete structures are produced layer-by-layer using a 3D printer. The nozzle, from which the concrete material is extruded, is mounted at a robot-arm or gantry system which moves according to a predefined digital print-path. The printed structure can be self-supporting, which means that no formwork is necessary anymore, increasing the freedom of form while decreasing the total construction costs. Moreover, large material savings can be achieved, making 3DCP a potentially more sustainable construction method. Sustainability is important since the production of cement is responsible for 8% of the worldwide carbon dioxide (CO2) emission [1].

There are already a number of civil engineering structures realised using 3DCP as the main construction method. The design of these structures is influenced by the printing process, which introduces new design challenges and new and other design variables. The application of traditional reinforcement is not trivial and the fresh concrete structure must be sufficiently strong and stable to resist the self-weight of the subsequent layers, which is a function of the material properties, tool-path lay-out and process characteristics. Moreover, the material properties can be orthotropic. These factors increase the complexity of the design process which challenges structural engineers designing 3DCP structures. Therefore, the aim of this research is to establish a link between the manufacturing process and the structural design of a 3DCP structure, to find the key parameters influencing the design and provide guidelines for future research and optimization towards more cost-efficient and sustainable construction practice. This is done by developing a parametric model that is capable of performing the structural design validation in both fresh and hardened concrete state.

Based on an extensive literature study on the large spectrum of research related to 3DCP, the most important process characteristics that affect the global structural behaviour are selected. First of all, a fresh concrete element might fail if the strength and stiffness development in time is not fast enough to cope with the increasing self-weight. The maximum height to prevent failure is dependent on the object geometry, fresh material properties and process characteristics. Second, the mechanical strength of a 3DCP bridge can become anisotropic due to a decreased bond-strength between two subsequent layers. The most important cause of this decrease is drying of the concrete filament, mainly due to a large required time to print one layer. Third, the final layer-geometry strongly depends on the fresh concrete material properties. A more stiff, viscous material requires more pumping energy to pass the printer system, but the layer geometry is more or less equal to the nozzle dimensions. Material that is less viscous flows more easily through the printer system, but will deform after deposition resulting in a different layer geometry.

The structure that is analysed in this research is a simply-supported cyclist bridge, made out of multiple 3DCP elements that are connected by an epoxy joint material. The main load bearing structure is the deck, which consists of several 3DCP elements consisting of a box-girder cross-section topology. To limit the tensile stresses at mid-span, prestressing tendons are placed inside the openings and stressed at both ends through reinforced concrete anchor blocks. To assess the safety of a 3DCP bridge structure, a comprehensive overview of design validation checks (Unity Checks or UC's) is established. These are based on the guidelines described in Eurocode, which are partly proven to be suitable for calculating the resistance of 3DCP structures. In order to compare different 3DCP design alternatives, two performance indicators (PI's) are defined: the first one is a measure of cost and the second one reflects the sustainability of the design.

The parametric research model is used to perform an extensive parameter study and to help analysing the benefit of optimisation strategies. The main function of the parametric research model is to generate a bridge design, expressed as the design validation checks in both fresh and hardened state, the performance indicators and a design visualisation. The model input parameters describe the structural boundary conditions, the print-path geometry, material properties and process characteristics. Because a large number of design alternatives is analysed, the model is constructed without the use of any Finite Element (FE) software in order to limit computation time. The structural performance of the fresh concrete structure is assessed using the analytical prediction model developed by Suiker [2]. The performance of the final, hardened structure is assessed based on stress resultants calculated using analytical equations assuming a 1.5D beam model. After valida-

tion of this simplified approach by performing a set of FE analyses, it is concluded that the parametric model serves as a sufficiently accurate and fast tool for designing and analysing the feasibility and performance of 3DCP structures.

Using the research model, an extensive parameter study is carried out. First, the model is analysed qualitatively to check if no inconsistencies are present and to obtain a first impression of the model characteristics. Next, a global sensitivity analysis using the Sobol' method is performed to obtain the relative parameter importance for the value of the UC's and PI's. The study shows that the span and cross-sectional dimensions are predominant for most output quantities, only the shear resistance design check is influenced by the concrete tensile strength. The required amount of prestress to limit tensile stresses is also dominated by the geometry. This implies that for improving the design, changing the geometry is most effective. Improving the material strength will only improve the shear resistance.

In a third study, the absolute effect of a decreased inter-layer bond-strength is obtained by analysing the effect on the design for three different bond-strength reduction functions derived from literature: no decrease, a moderate or a high decrease. It turned out that a moderate and high degree of bond-strength in time results in a 14% and 50% increase of the shear strength design check respectively, at a low print speed of 80 mm/s. The required amount of prestress increases with 11% and 28% for the moderate and high decrease, respectively. These results imply that the degree of decreasing bond-strength is more influential than the print speed. Therefore, it is important to accurately characterise the bond-strength reduction function of time.

In literature, it is recognised that the material properties of 3DCP samples typically contain large scatter. Therefore, an uncertainty analysis is conducted to identify 1) the scale of the parameter uncertainty due to process effects and 2) to quantify the effect of this uncertainty on the model output. Material property data from tests conducted on 3DCP specimens shows that the main source of uncertainty can be allocated to a difference between the different printing days. The printing process facility itself is well controlled. After analysing the uncertainty propagation through the model, it is concluded that this material spread is not causing a higher uncertainty than accounted for by the safety factors defined in Eurocode.

The research is concluded with the analysis of a case study. The design for a 3DCP bridge in Noord-Holland, a Dutch province, is optimised for minimising both cost and environmental footprint. This is done using the second order constrained Trust-Region optimisation algorithm. The constraints are defined as the design validation checks. The design variable set contains all geometry- and process parameters, the material parameters are left constant. These two optimisation objectives clearly yield two different designs. For the cost-efficient design, the performance in the fresh concrete state is most important, since additional joints are relatively expensive. Therefore, the algorithm will force the design to maximise the printable height which results in a high layer-width. This increases the self-weight which requires a large amount of prestress. For the sustainable design, the number of joints is of lesser importance, yielding a more slender design which allows for decreasing the required amount of prestress. Second, for the same case-study, a feasibility study for increasing bridge span is conducted. Redesigning the structure shows that a bridge having a span of $L = 19.4$m is feasible, but due to the slenderness an additional dynamic verification check should be conducted.

In the previous analyses it has been assumed that the tensile strength of the joints is higher than that of the concrete. Therefore, a scenario in which the joints between the subsequent 3DCP elements have no strength is analysed. This causes the development of a kinematic mechanism when tensile stresses are introduced. The bending moment capacity of this mechanism is fully delivered by the prestressing steel and its internal lever arm. To satisfy the bending moment capacity design check, a higher amount of prestress is required, which implies that accurately describing the joint tensile strength is important.

Finally, two different future optimisation solutions are discussed. It is shown that introducing a kinked tendon-profile is beneficial for large span ($L > 16m$) bridges if it is assumed that the joints have no strength. Introducing a non-prismatic bridge cross-section by curving the bottom-line can yield a reduction of the required amount of prestress up to 40%.

The integration of the printing process into the structural design of a 3DCP bridge into one analytical parametric research model proves to be a useful method to analyse and design 3DCP structures. Analyses using this model show that the geometry of the cross-section and the structure's boundary conditions are most influential for the feasibility and performance of a 3DCP bridge design. The novel design and analysis method developed in this research serves as a basis for further research and design optimisation for which a set of recommendations is proposed.

Contents

Nomenclature

Abbreviations

3DCP   3D Concrete Printing

AM   Additive Manufacturing

c.a.   Centroidal axis of cross-section

FE   Finite Element

GWP   Global Warming Potential

LB   Lower Bound

LCA   Life Cycle Assessment

OPC   Ordinary Portland cement

PI   Performance Indicator

RC   Reinforced Concrete

SA   Sensitivity Analysis

SI   Sensitivity Index

SLS   Serviceability Limit State

SLS_0 Prestress design scenario requiring a compression-only structure in SLS

SP   Shadow Price

UB   Upper Bound

UC   Unity Check

ULS   Ultimate Limit State

ULS_{fctd} Prestress design scenario requiring the tensile stress in ULS to be smaller than f_{ctd}

Latin Symbols

$\dot{l}$	vertical building rate	[m/s]
$€_C$	shadowprice per m^3 of concrete	[€/m^3]
$€_M$	price per h of printing	[€/h]
$€_M$	price per kg of concrete	[€/kg]
$€_P$	shadowprice or cost-price per kg of prestressing steel	[€/kg]
$\bar{l}_{cr}$	dimensionless critical buckling height of fresh concrete element	[-]
$\bar{l}_p$	dimensionless height of fresh concrete element at which plastic collapse occurs	[-]
A	concrete cross-sectional area	[m^2]
a	reduction of cross-sectional height at mid-span (yielding a non-prismatic beam)	[m]
A_p	total cross-sectional area of prestressing tendons	[m^2]
A_{thix}	structuration rate of fresh concrete	[Pa/s]
b	layer width	[m]

b_w	total width of webs	[m]
$C(t)$	cohesion of fresh concrete at time t	[Pa]
C_0	cohesion at time t=0	[Pa]
d	layer height	[m]
D_0	initial bending stiffness of fresh concrete wall part	[Nm]
E	Young's Modulus of hardened concrete	[MPa]
$E(t)$	Young's Modulus of fresh concrete at time t	[Pa]
E_0	Young's Modulus of fresh concrete at time t=0	[Pa]
e_p	tendon eccentricity	[m]
$f_1(\mathbf{x})$	performance indicator 1: material and printing costs	[€]
$f_2(\mathbf{x})$	performance indicator 2: shadow price	[€]
F_{AR}	strength correction factor	[-]
f_{cd}	design compressive strength	[MPa]
f_{ck}	characteristic compressive strength	[MPa]
f_{ctd}	design tensile strength	[MPa]
f_{ctk}	characteristic tensile strength	[MPa]
g	gravitational acceleration	[m/s^2]
$G_{k,j}$	characteristic value of permanent action j	[-]
H	cross-sectional height	[m]
I	moment of inertia of the cross-section	[m^3]
k	stiffness of structure	[N/m^3]
L	bridge span	[m]
l	height of one 3DCP element	[m]
l_{cr}	critical buckling height of fresh concrete element	[m]
$l_{k,s}$	length of sloped part in case of kinked tendon profile	[m]
l_p	height of fresh concrete element at which plastic collapse occurs	[m]
M	total mass of concrete	[kg]
M_P	required amount of prestressing steel	[kg]
M_{Ed}	design value of acting bending moment	[m^3]
M_{Rd}	design value of bending moment resistance	[m^3]
N	number of bridge elements	[-]
n	number of cells in cross-section	[-]
N_L	number of layers in one bridge element	[-]
P	prestressing force	[kN]
P_{m0}	prestressing force after initial losses	[kN]
$P_{m\infty}$	working prestressing force (after time-dependent losses)	[kN]
P_{max}	maximum allowed prestress force during stressing	[kN]
q_{fk}	characteristic vertical distributed variable load	[kN/m^2]

Q_{fvd}	characteristic concentrated variable traffic load	[kN]
$Q_{k,i}$	characteristic value of variable action i	[-]
Q_{serv}	load representing a service vehicle	[kN]
R_{thix}	re-flocculation rate of fresh concrete	[Pa/s]
RH	relative humidity	[%]
S	length of print-path	[m]
S	static moment	[m^3]
s	longest unsupported part of print-path	[m]
S_i	first-order sensitivity index of parameter i	[-]
S_{Ti}	total sensitivity index including interaction effects	[-]
T	temperature	[°C]
T	total printing time	[h]
t	element age	[s]
t_{rf}	time frame in which re-flocculation takes place (fresh concrete)	[s]
ti	time gap between two subsequent layers	[s]
UC_M	UC for the bending moment capacity	[-]
UC_V	UC for the shear strength	[-]
$UC_{f_{cd}}$	UC for the concrete compression strength	[-]
$UC_{f_{ctd}}$	UC for the concrete tensile strength	[-]
$UC_{f_{ctk}}$	UC for concrete crushing due to the prestressing force	[-]
UC_P	UC for the prestressing steel strength	[-]
UC_w	UC for the deflection	[-]
v	horizontal print speed	[m/s]
V_c	total volume of concrete	[m^3]
V_{Ed}	acting shear force	[kN]
$V_{Rd,c}$	shear force capacity	[kN]
W	width of bridge	[m]
w	deflection at mid-span	[m]
$W_{top/bot}$	section modulus at top or bottom of cross-section	[m^3]
deg	degree of bond-strength reduction: none, moderate or strong	[-]
dx	element size	[m]

Greek Symbols

α	angle of sloped part of kinked tendon profile	[°]
α_T	thermal expansion coefficient	[1/°C]
α_σ	linear strength increase in time	[Pa/s]
$\alpha_{cc,pl}$	compressive strength reduction factor for unreinforced concrete structure	[-]
$\alpha_{ct,pl}$	tensile strength reduction factor for unreinforced concrete structure	[-]
α_C	linear cohesion increase in time	[Pa/s]

α_E	linear Young's Modulus increase in time	[Pa/s]
γ_σ	strength ratio	[-]
γ_C	partial factor for concrete	[-]
$\gamma_{G,f}$	partial factor for permanent action j	[-]
γ_P	partial factor for prestressing actions	[-]
$\gamma_{Q,i}$	partial factor for variable action i	[-]
λ_c	conductivity	[W/(m °C)]
ν	Poisson's ratio	[-]
ω	eigenfrequency	[Hz]
$\overline{\zeta}_\sigma^l$	dimensionless linear curing rate for the strength	[-]
$\overline{\zeta}_E^l$	dimensionless linear curing rate for the stiffness	[-]
ϕ	angle of internal friction of fresh concrete	[rad]
ψ_0	factor for combination value of a variable action	[-]
ψ_1	factor for frequent value of a variable action	[-]
ψ_2	factor for quasi-permanent value of a variable action	[-]
ρ	density of hardened concrete	[kg/m^3]
$\rho_c c_c$	thermal capacity	[J/(m^3°C]
ρ_f	density of fresh concrete	[kg/m^3]
$\sigma(t)$	compressive strength of fresh concrete at time t	[Pa]
σ_0	compressive strength of fresh concrete at time t=0	[Pa]
$\sigma_n(t)$	normal stress in fresh concrete at time t	[Pa]
$\sigma_{c,p}$	acting compressive stress from prestress or normal force	[MPa]
$\sigma_{p,max}$	maximum allowed prestress during stressing	[MPa]
$\sigma_{p\infty}$	working prestress	[MPa]
$\tau_S(t)$	static shear yield strength of fresh concrete at time t	[Pa]
τ_y	pressure-dependent yield shear strength of fresh concrete at time t	[Pa]
τ_D	dynamic yield strength of fresh concrete at time t	[Pa]
$\tau_{S,i}$	initial static yield strength of fresh concrete at time t	[Pa]
ζ	reduction factor	[-]
ζ_σ^e	exponential curing rate for the strength	[1/min]
ζ_σ^l	linear curing rate for the strength	[1/s]
ζ_E^l	linear curing rate for the stiffness	[1/s]

1

Introduction

1.1. Context

3D concrete printing (3DCP) is a new Additive Manufacturing (AM) technique in which structures are built-up by subsequent deposition of cementitious material in a layer-wise fashion. The material is extruded through a print-head, steered by a digitally controlled robot-arm. Unlike conventional concrete construction, a structure is built without the use of formwork, increasing the freedom of form. Material can be placed where (structurally) needed only, which allows for achieving large material savings. This advantage can be used to design more sustainable structures. Moreover, 3DCP construction enables a fully automated digital manufacturing process, since digital design models can be translated into tool-paths which can be sent to the printer directly. This increases construction speed, while production cost, labor cost and construction waste decrease. In the past 10 years, this new technique has been in development and many projects have shown the potential it has for large-scale application in the construction industry [3]. One of these projects is the world's first 3DCP bridge, located in Gemert, the Netherlands (see fig. 1.1). This pedestrian- and cyclistbridge was opened in October 2017 and is constructed using 3DCP in combination with post-tensioning for the load-bearing structure.

Figure 1.1: World's first 3DCP bridge in Gemert, the Netherlands (from [4]).

Designing a bridge using such an innovative construction method is challenging. Regulations or guidelines related to 3DCP structures are non-existent in current design codes yet. Therefore, the design calculations performed for the Gemert bridge were based on the guidelines specified in Eurocode parts NEN-EN 1990, NEN-EN 1991 and NEN-EN 1992. However, given the empirical nature of computing the concrete's material resistance, the calculation procedures in these codes are likely not fully applicable to calculating the printable concrete material resistance. Therefore, a 1:2 scale model of the bridge was printed and tested prior to construction to prove the design was safe. This design approach is called 'Design by testing'. The destructive scale-model test demonstrated that the bearing capacity was well above the design capacity as failure did not occur and first cracks appeared at higher load levels than expected. In addition, the load-bearing capacity

1

of the bridge was tested on-site, since also the 3D concrete printing production process is not yet certified. Loading the bridge with the ULS design load did not induce any cracking at all, after which the bridge was proven safe. For details about these tests, reference is made to [5].

Next to the previously mentioned issues related to the structural design of a 3DCP bridge, many challenges arise regarding the process of printing the bridge elements. Because no formwork is present to support the growing fresh concrete structure after deposition, the material should be strong, stiff and stable enough to carry the self-weight of subsequent layers. At the same time, the fresh concrete material should be soft enough to provide sufficient bond with the following layer and to flow through the printing system without congestion. For the Gemert bridge, suitable printer settings have been found through an extensive research program (carried out at TU/e). The bottle-shaped cross-section topology of the bridge is designed such that failure of the fresh concrete structure during printing is prevented, by providing sufficient internal supports in the cross-section [5].

1.2. Problem statement

Designing 3DCP structures is different from designing conventional concrete structures. The fresh concrete structure can be self-supporting, so formwork is not necessary which gives the designer more freedom. However, the material should be strong and stable enough to resist the increasing self-weight. Furthermore, due to the layer-wise build-up of the structure, the hardened material properties can become anisotropic and traditional reinforcement strategies cannot be applied in 3DCP structures. Hence, the structural design of these structures is influenced by the printing process which introduces additional design variables and constraints. Moreover, the effect of the 3D printing process on the global structural behaviour is unknown yet. This makes designing 3DCP structures more complex, facing the structural engineer with new challenges.

1.3. Research objective

In this research, a connection is established between the printing process and structural performance of a 3DCP structure. Starting point is the design of a post-tensioned 3DCP cyclist bridge, similar to the design shown in fig. 1.1. A parametric research model will be developed in which a 3DCP bridge design can be generated for user-defined parameter input. Using this model, the influence of each parameter on a 3DCP bridge design can be analysed in a systematic way, yielding increased understanding in the relationships between printing process parameters and structural design. Subsequently, optimal parameter sets are sought for, by considering a cost-minimization and an environmental impact-minimization objective. This project will provide design- and research guidelines to enable cost-effective and sustainable future 3DCP bridge designs.

The following research question and corresponding set of sub-questions will be answered:

"What is the influence of printing process parameters and 3D printable concrete material properties on the structural design of a 3DCP cyclist bridge and how can this design be optimised to unlock the potential of cost-effective and sustainable bridge structures?"

1. How does the printing process affect the global behaviour of a 3DCP bridge structure and how can these effects be incorporated in a structural design model?

2. Which criteria should be considered for assessing the feasibility of a 3DCP bridge design and how can these be modelled?

3. What are the key parameters determining the performance and feasibility of a 3DCP bridge design both during printing and after hardening?

4. What is an optimal 3DCP bridge design considering cost and sustainability?

1.4. Scope

- This thesis restricts itself to the parametric modelling and optimisation of simply supported, post-tensioned 3DCP cyclist- and pedestrian bridge designs, built in the Netherlands.

- This thesis is about extrusion-based concrete printing only. No particle-bed approach will be discussed.

- In this research, the concrete mix design will not be optimised. Existing mortar of which the properties

are known are used throughout the research. However, depending on the resulting influence of the material properties on the bridge design validation, suggestions can be done for improving the mix design.

- Finally, because Witteveen+Bos collaborates with BAM Infra and SG Weber Beamix, the research will be calibrated to the specifications of the printer facility of these parties.

1.5. Research methodology & thesis outline

1.5.1. Knowledge phase
A literature study is conducted to answer parts of the research questions defined in section 1.3. First, an thorough study is performed to understand the 3DCP process and material behaviour. Subsequently, the design criteria in the fresh and hardened concrete state should become clear together with the design and manufacturing process parameters that influence these criteria. In addition to the published literature, experts in the field of 3D concrete printing from Witteveen+Bos (structural design and engineering) and Weber Beamix + BAM (print mortar supplier and manufacturing of printed elements) will be consulted. The study is separated in a part related to 3D concrete printing described in chapter 2 and in a part related to 3DCP bridge design explained in chapter 3.

1.5.2. Create and validate research model
To analyse the underlying relations between parameters and 3DCP bridge design, a parametric model is developed. The design criteria and performance indicators are modelled as a function of the input parameters. In chapter 4 the adopted structural model for calculating these functions is described. The parameter set used as input is derived from the knowledge collected in chapters 2 and 3. The parametric model serves as a tool for generating a design based on a given set of input parameters. It visualizes the design and provides information about the feasibility and performance of the design.

1.5.3. Parameter study
In this phase, the underlying relations between each design variable and the set of criteria and performance indicators are analysed by means of a parameter sensitivity analysis. It will gain insight in the influence each parameter has on the design. Initially, this knowledge is used to check and potentially simplify the parametric model and eventually yields insight in the design sensitivity to the set of parameters. Additionally, the influence of parameter uncertainties induced by the process on the design is studied by means of an uncertainty analysis.

1.5.4. Case-studies
To show the potential of cost-effective and sustainable future bridge designs, two case-studies are conducted. In the first case-study, several optimisations of a reference design for a 3DCP bridge in Noord-Holland are proposed. The benefit of several design variations is analysed and an optimal parameter set is sought for, considering two parameter indicators. The results provide guidance in the design of future 3DCP bridges. The second case-study is a comparison between the bottle-shaped and box-girder design, applied to the bridge design of Gemert.
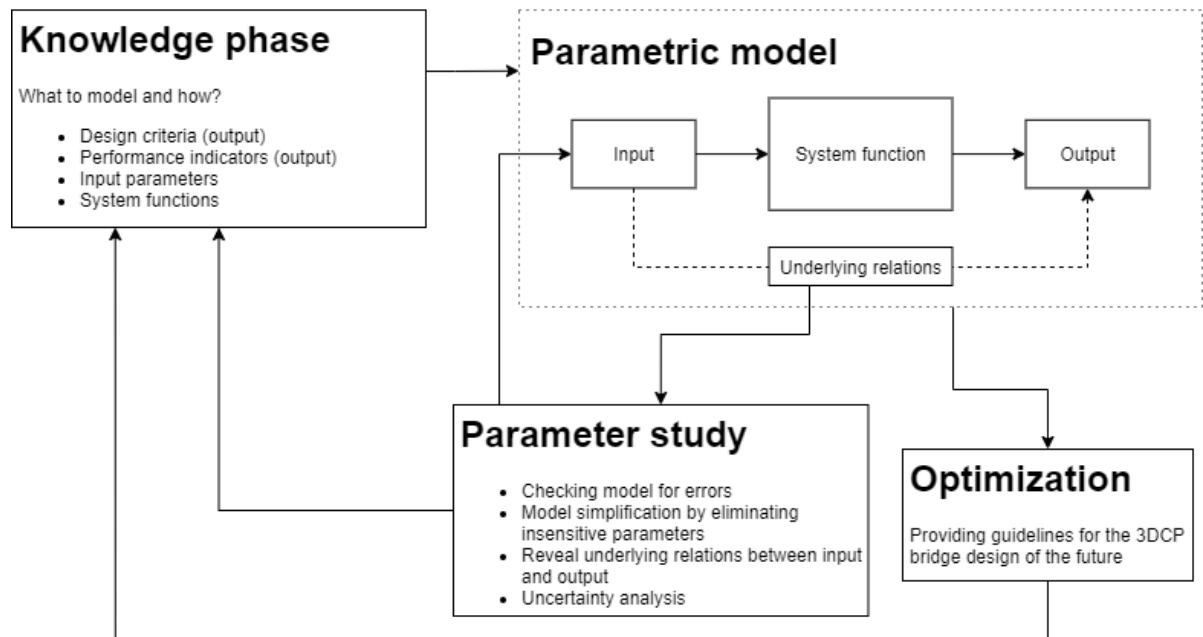
Figure 1.2: Schematic overview of methodology.

A schematic overview of the methodology is presented in fig. 1.2.

2

Introduction to 3D concrete printing

2.1. How does it work

2.1.1. The printing facility

Today many research institutes and engineering companies have opened 3DCP facilities for both research and commercial purposes. Each printer facility is different, having specific dimensions and features. Most 3D printing facilities are located inside in a controlled environment. However, in the future, printing robots might be located on site yielding a production process similar to in-situ concrete casting. In fig. 2.1, the printing facility of BAM Infra and SG Weber Beamix in Eindhoven is shown.

Figure 2.1: 3D concrete printing facility BAM Infra and SG Weber Beamix, from [6].

A 6-dof robot-arm is mounted on a 10m rails, from which it can serve a print-area of lxwxh = 11x3.5x3.5m. Dry concrete mix is stored in a large silo, mixed with water and pumped through a 30 meter long hose connected to the printer head. At the printer head a circular or a rectangular nozzle is mounted with which layers of varying sizes can be printed. The horizontal printing speed v with which the printer-head moves varies between 80-180 mm/s. The robot arm moves according to a digitally defined tool-path and upon subsequent stacking of multiple layers, a structure arises. The vertical print speed or building rate $\dot{l}$ can be derived from the layer geometry, tool-path length and horizontal print speed. See fig. 2.2 for a geometrical representation of the previously mentioned printer variables.
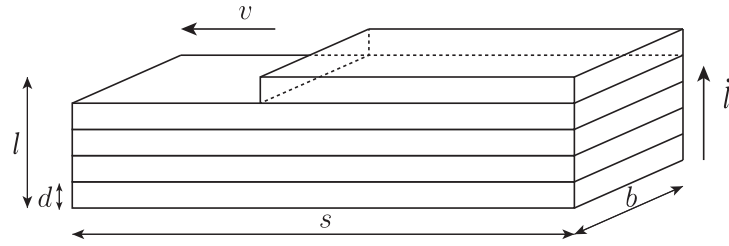
5

Figure 2.2: Layer-wise build-up of straight 3DCP wall structure with length s using a rectangular nozzle with dimensions bxd

2.1.2. Geometrical freedom

The most important benefit of using 3D concrete printing as a construction method is the large geometrical freedom. Because no formwork is required anymore, thin-walled and curved structures can be created easily without the need for making customised moulds. However, the shape, size and topology of a 3DCP structure is inherent to the properties and practical limitations of the printer and therefore certain limitations do exist. In this section, three aspects are discussed briefly.

On site printing vs. prefab

The printing facility shown in fig. 2.1 is located at a production hall. After hardening, the elements are transported to the building site and assembled, similar to the use of traditional prefabricated elements. Printing inside a facility is beneficial, since the environment of the hardening concrete can be controlled. However, there are transportation limits that should be taken into account: there is a maximum element size and there is a risk for cracking of the concrete structure during handling. Using a printer located on site solves this problem and can be compared to traditional in-situ concrete casting. However, this is challenging and therefore not done very often because the hardening concrete suffers from external environmental conditions which affects the concrete quality.

Double curved surfaces

The creation of double-curved surfaces is possible, but not trivial. The fresh concrete material is unsupported and stacking layers in a cantilevering fashion decreases the stability of a printed structure. This requires a high stiffness of the material. Engineers of Twente Additive Manufacturing recently published a video with an arch spanning more than 0.5 meters without the use of any support, see fig. 2.3a. If the material is less stiff, the use of a temporary infill support material is a solution. Schipper et al. created a thin shell structure using a combination of printing and casting. The edge of the structure is printed on an adaptable mould of which the geometry can be defined using Grasshopper. Subsequently, concrete is cast into the printed border. Connecting several panels having a slightly different geometry yields a double-curved shell structure [7]. In fig. 2.3b the resulting structure consisting of multiple panels is shown.

(a) 0.5m span created with cantilevering layers without using support material, from [8].

(b) Creating a double-curved shell structure using a combination of 3DCP and casting on an adaptable mould, from [7].

Figure 2.3: Double-curved surfaces using different approaches.

Nozzle type

Next to the fresh material properties, the width of the print-path strongly depends on the type and size of the nozzle that is used. Two types of nozzles can be distinguished: rectangular or circular, each having advan-

tages and disadvantages. A problem might arise for square or rectangular nozzles if corners are introduced in the tool-path. The material deposition rate increases at the inside and decreases at the outside of the corner, which may result in tearing at the outer edge. To prevent this, the nozzle should remain tangent to the concrete filament, which may require a larger corner radius [9]. Using circular nozzles this problem does not arise, however, in this nozzle the material is sheared prior to deposition due to the conical shape (more on this in section 2.2.1). This makes the concrete filament material flow, yielding a deformed shape (see fig. 2.4b). Concrete filaments extruded using rectangular nozzles are unsheared in the nozzle, able to develop a more stiff material consistency. Therefore, the layer has a shape practically equal to the nozzle opening (see fig. 2.4a) [10]. The filament shape can also be adjusted by using a down-flow nozzle, in which the material is slightly 'pressed' in the previous layer, resulting in a deformed shape. A nozzle using back-flow is more shape-consistent, but might result in poor inter-layer bond because the filament is more stiff, unable to intermix with the subsequent layer [5]. Hence, the final shape of the concrete filament depends on the interplay between material viscosity, print speed, pump pressure and nozzle size and geometry.

(a) Printing with a rectangular nozzle, from [11].

(b) Printing with a circular nozzle, from [12].

Figure 2.4: Different nozzle types

2.1.3. Printable concrete mix composition

Because no formwork or mold is present, a fresh printed concrete structure is unsupported and therefore, the material itself should be able to maintain shape after deposition. Additionally, the initial strength of the material should be sufficient to carry its own self-weight. However, this 'buildability' requirements on the fresh concrete material are contradicting the concept of 'pumpability'. After mixing, the concrete should be fluid enough to pass through the system without causing blockages due to seggregation of the concrete mix. This balance is mainly determined by the viscosity of the fresh concrete material, the printing speed, pump pressure and nozzle geometry. A highly viscous material will be strong and stiff enough to carry the subsequent layers, but requires high pump-pressure and can result in poor inter-layer bond. A concrete material with lower viscosity will be easily pumpable, but might be too weak to carry the self-weight of subsequent layers [10].

Printable concrete mixtures are different than conventional concrete mixtures. The properties are derived from self compacting concrete and spray concrete, typically having a high cement content and low aggregate size (max. 2mm). Chen et al. [13] provided an overview of the composition of concrete mixtures as reported by various research groups. Although some mixtures contain alternative binders such as silica fume, fly ash and limestone filler, CEM I Portland cement (Ordinary Portland Cement, OPC) takes op the highest portion in all mixtures, yielding a relatively high cement content compared with conventional concrete. Furthermore, the material should be low to zero slump and fast setting to maintain shape after deposition, which is achieved by decreasing the water content. Consequently, printable concrete mixtures have a low water to binder ratio, ranging from 0.26 [14] to 0.39 [15]. At the same time, the workability or pumpability of the material should be sufficient to prevent congestion in the printer system, which can be achieved by adding a superplasticizer. Adding a retarder increases the open time, while the concrete setting can be increased by an accelerator - a desired property in terms of buildability. To reduce plastic shrinkage cracking and initial deformation, a small amount of polypropylene fibers can be added. Glass, carbon and steel fibres can possibly be included to enhance the ductility of the concrete (see section 2.3.2).

To decrease the OPC content of the mixture and thereby decreasing the environmental impact, several research groups focus on the development of printable geopolymer mixtures. In most printable concrete mixtures, only part of the OPC is replaced by industrial by-products such as fly ash, blast furnace slag or silica fume, making the mixture more eco-friendly. Panda et al. [16] studied the mechanical properties of a geopolymer mixture in which the OPC content has been fully replaced by fly-ash activated by an alkaline solution, yielding a cementitious material. Paul et al. [17] compared the fresh and hardened material performance of a printable geopolymer mix with a printable OPC mix and a fiber-reinforced mixture. It turned out that the 100% geopolymer mix showed a larger strength increase in the fresh state, but reached a lower mechanical compression strength.

2.2. Fresh concrete

2.2.1. Material rheology

Fresh printable concrete materials can be characterized as a visco-plastic Bingham (non-Newtonian) fluid: the material flows when subjected to a stress higher than a certain threshold value equal to the static yield strength $\tau_{S,i}$ of the material. If the material is sheared, it starts flowing as a viscous fluid. When at rest i.e. directly after deposition, the material is able to build-up an internal structure because of its thixotropic behaviour, while still being in the dormant phase prior to setting. This thixotropic property is key for printable concretes: the material is able to flow during pumping when sheared by the mixer and after deposition the material is at rest, being able to acquire strength and stiffness. When using a rectangular-shaped nozzle, the bulk material in the nozzle remains unsheared, yielding a rather stiff concrete filament shaped by the nozzle. Concrete material extruded through a circular nozzle is sheared prior to deposition and spreads out on the print-bed before it starts building an internal structure and acquiring shape [10]. Three different models describing the thixotropic behaviour of the fresh concrete were found in literature, which are discussed below.

- Roussel [18] proposed a thixotropy model (eq. (2.1)) assuming a linear evolution of the shear yield strength in time $\tau_S(t)$. The stress increase is devoted to the structuration rate A_{thix} due to the formation of CSH-bridges between cement grains. The CSH-bridge formation is assumed constant because the heat of hydration is constant in the dormant phase, resulting in a linear yield stress increase.

$$\tau_S(t) = \tau_{S,i} + A_{thix}t \tag{2.1}$$

- An expansion of this linear stress evolution to a bi-linear thixotropy model is proposed by Kruger et al. [19], adding a second branch related to the material re-flocculation (see fig. 2.5). In the first few hundreds of seconds after the material has left the nozzle, the static yield stress τ_S is restored from the dynamic yield stress τ_D (the yield stress present in the pump-system when mixed) with a rate R_{thix}. After reaching the static yield shear stress, the strength increases with the structuration rate A_{thix}, following the model of Roussel.
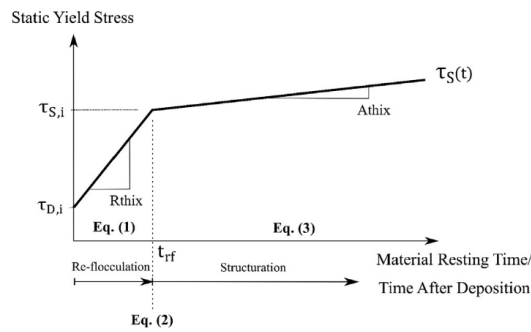

Figure 2.5: Bi-linear static yield stress evolution in time, proposed by [19], characterised by a re-flocculation phase followed by structuration. From [19].

Relation related to Eq.(1) in fig. 2.5:

$$\tau_S(t) = \tau_D + R_{thix}t \tag{2.2}$$

Relation related to Eq.(3) in fig. 2.5:

$$\tau_S(t) = \tau_{S,i} + A_{thix}(t - t_{rf}),\tag{2.3}$$

where $\tau_{S,i}$ is the initial static yield stress of the material and t_{rf} the time frame in which re-flocculation takes place: $t_{rf} = (\tau_{S,i} - \tau_D)/R_{thix}$.

• Perrot et al. [20] reported an exponential increase of the yield strength, after an initial linear increase up to about 40 minutes concrete resting time. This exponential increase is devoted to an increase of the solid volume fraction, resulting in an exponential yield stress increase. Figure 2.6 shows the deviation between the linear and exponential branch at about 40 minutes.
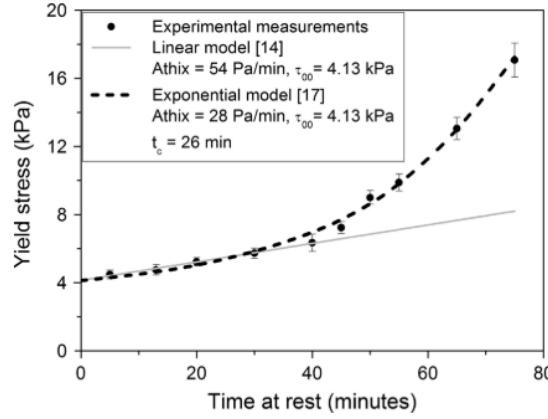

Figure 2.6: Exponential vs. linear increase of static yield stress, from [20].

The time frame in which the re-flocculation rate described in the bi-linear model [21] is taking place is negligible (first hundred seconds) relative to the time frame of the structuration rate (order of thousand seconds). The exponential model requires more material input which introduces additional uncertainties and is less conservative than the linear model.

2.2.2. Mechanical properties

Material yielding of a fresh concrete structure can be described based on the behaviour of soils [22]. The material fails due to the sliding of particles rather than crushing of particles [23]. Therefore, the material yield strength can be described as a pressure-dependent shear stress, according to the Mohr-Coulomb criterion as follows:

$$\tau_y(t) = C(t) + \sigma_n(t)\tan\phi,\tag{2.4}$$

where $C(t)$ is the cohesion of particles bonded by cement, ϕ the angle of internal friction delivered by friction and mechanical interlocking between internal particles, $\sigma_n(t)$ is the acting normal stress equal to the self-weight and $\tau_y(t)$ is the shear yield stress, determined at time t. The time-dependency is added to account for the thixotropic build-up of the concrete. Material properties describing the stiffness of the material are the Young's Modulus of elasticity $E(t)$ and the Poisson ratio ν, again enhanced with a time dependency. These material parameters can be derived by conducting experiments on fresh concrete specimens at several ages. A direct shear test (DST) allows for deriving the Mohr-Coulomb parameters and an unconfined uni-axial compression test (UUCT) allows for determining the Young's Modulus, Poisson's ratio and also the compressive strength $\sigma(t)$. A triaxial compression test (TCT) can be used to derive all parameters. Wolfs et al. performed a set of DST's and UUCT's [22] and a set of TCT's [24] for three different concrete mixes (Weber 3D 115-1, 145-1 and 145-2) to determine the previously mentioned material parameters. In all experiments, cylindrical fresh concrete specimens of ages up to 90 min were tested, because this time-frame is critical for failure of the fresh concrete structure. The properties of the Weber 3D 160 have been determined using a 'reverse engineering' approach. A straight wall was printed and by modelling the buckling failure of this wall in a numerical model, the corresponding material properties could be derived [25]. In table 2.1 an overview of the average material properties for each mixture is presented. For the Weber 3D 115-1 mixture, a typical

stress-strain diagram for various concrete ages together with a plot of the linearly increasing shear strength, compressive strength and Young's Modulus in time are given in section 2.2.2.

The cohesion, Young's Modulus and compressive strength all increase linearly in time, corresponding to the linear thixotropy model proposed by Roussel [10]. Note that there are substantial differences in initial values and structuration rates between these three mixes. Furthermore, a constant value for the angle of internal friction was reported although the experiments showed that strengthening under confining pressure is age dependent. For the W145-2 mixture, the young samples showed almost no strengthening, but the older samples of age 60 and 90 min did show strengthening with an angle of internal friction of about 6-7°. In this research, a constant value of 1°is assumed, corresponding to the younger samples which is conservative. The angle of internal friction of the W115-1 shows a less pronounced age-dependency as this mixture is already quite stiff at a young age. Note that for a low angle of internal friction, the Mohr-Coulomb criterion approaches the Tresca failure criterion.

In [24], among others, it is emphasized that the fresh concrete material properties are difficult to predict given the dependence on additional parameters such as temperature, system friction and the presence of imperfections. As a consequence, the material properties may vary for each print session, given the influence of the printing environment and material composition on the previously mentioned parameters. This might explain the large experimental spreads that were reported, typically about 20% [22, 26]. Therefore, in chapter 5, the influence of the uncertainty in material properties on the final design is investigated.

Table 2.1: Fresh concrete material properties of different Weber mixtures, increasing linearly in time up to t = 90 minutes.

|		**Weber 3D 115-1** UUCT+DST [22]	**Weber 3D 145-1** UUCT [26]	**Weber 3D 145-2** TCT [24]	**Weber 3D 160** numerical model [25]
$C(t)$	[kPa, min]	$3.05 + 0.058t$	-	$2.60 + 0.06236t$	-
ϕ	[°]	20°	-	1°	-
$E(t)$	[kPa, min]	$77.912 + 1.227t$	$17.369 + 3.423t$	$48.564 + 2.609t$	$55.0 + 2.31t$
ν	[-]	0.3	0.3	0.3	0.3
ρ_f	[kg/m^3]	2070	2175	2100	2100
$\sigma(t)$	[kPa, min]	$5.984 + 0.147t$	$1.109 + 0.314t$	$4.414 + 0.172t$	-

2.2.3. Failure of a fresh concrete structure

Failure of the fresh concrete structure can be characterised by two failure modes: elastic buckling and plastic collapse. The first failure mode is caused by a loss of stability of the structure, resulting in local or global buckling failure. The second is a strength-based failure where it is assumed that the structure fails if the yield strength in the bottom layer is reached by the increasing self-weight of the structure. For structures with a large aspect ratio i.e. slender structures, elastic buckling is more likely to occur. Global failure by plastic collapse is more likely for structures with enhanced stability. The characterization of both failure modes is discussed hereafter based on different prediction models presented in literature.

- Suiker [2] presented a mechanistic model to predict the maximum object length considering both plastic collapse and elastic buckling, given a linear or exponential curing process i.e. a linear or exponential strength- and stiffness increase in time. Elastic buckling is described for given boundary conditions of a printed wall: free, simply supported, clamped or something in between e.g. a spring. Failure by plastic collapse can be characterized by two failure criteria: compressive failure upon reaching the maximum compressive stress or a shear failure described by the Mohr-Coulomb criterion. The model is also capable of predicting the type of failure mode by introducing a number of dimensionless constants.

- Based on rheology and a linear thixotropy model, Roussel [10] derived the minimal required structuration rate A_{thix} to prevent plastic collapse of the structure. Secondly, an equation for predicting the critical height at which buckling of a free wall initiates is presented.

- Kruger [23] presented a buildability model to compute the maximum possible number of layers based on the bi-linear thixotropy model, considering solely plastic collapse.
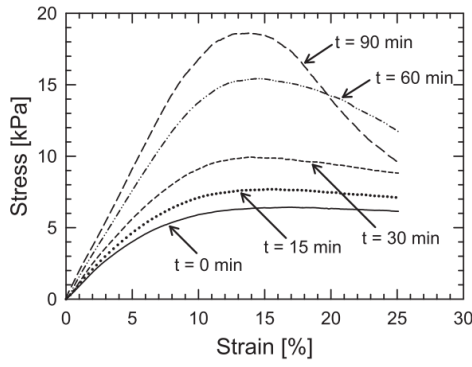
(a) Average compressive stress-strain relations for various concrete ages.
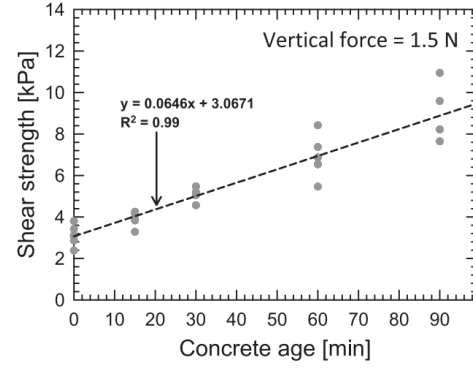
(b) Shear strength development up to 90 min derived from the DST with a vertical load of 1.5N. The grey marks indicate the individual test results and the dashed black line represents a linear fit based on the average test results.
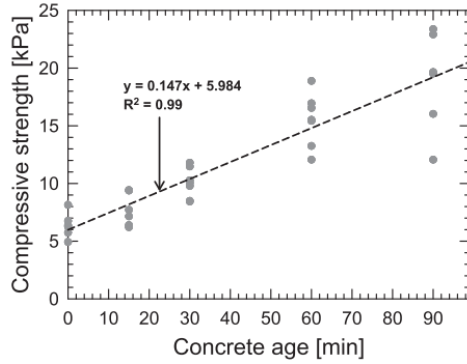
(c) Compressive strength development up to 90 min derived from the UUCT. The grey marks indicate the individual test results and the dashed black line represents a linear fit based on the average test results.
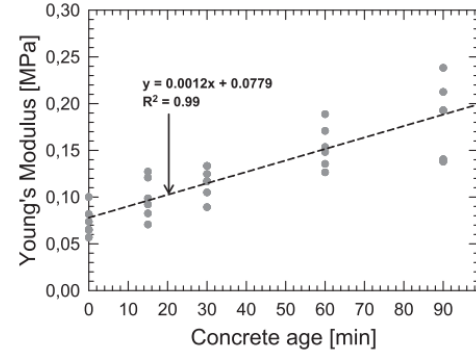
(d) Development of Young's Modulus up to 90 min derived from the UUCT. The grey marks indicate the individual test results, the dashed black line represents a linear fit based on the average test results.

Figure 2.7: Material properties for the Weber 3D 115-1 mixture. All figures are adopted from [22].
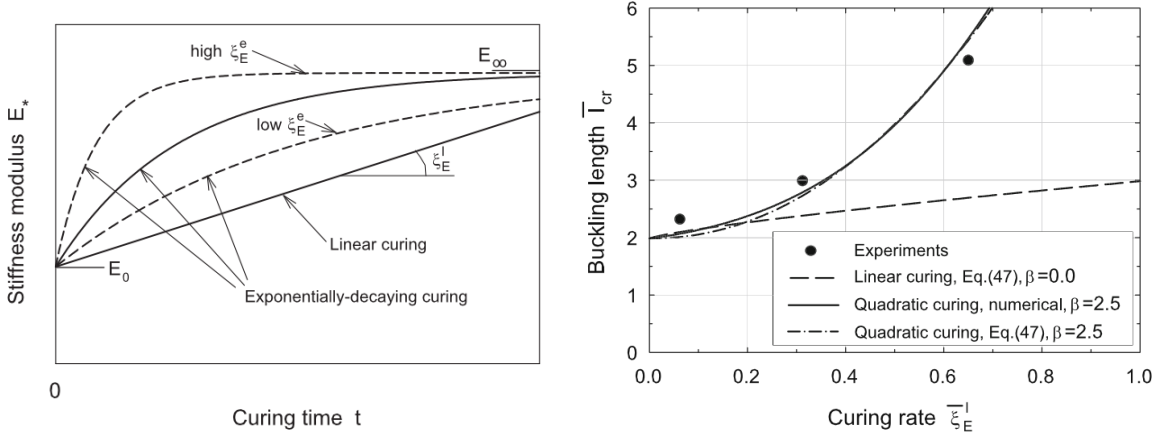
Elastic buckling

Failure by elastic buckling is initiated by a loss of stability. Both Suiker [2] and Roussel [10] developed a model to predict the critical object height l_{cr} at which buckling first initiates. Roussel's model is valid for a straight, vertical wall structure and can be calculated relatively easy with one single equation. The model underestimates the critical buckling height, but can be used to obtain a first, conservative estimate. The prediction model of Suiker is more comprehensive and will therefore be discussed in more detail. It allows for defining the support configuration of a printed wall, provided by the adjacent walls, being free, simply-supported, fully clamped or something in between. The buckling mode is described by a fourth order differential equation and a set of boundary conditions and can be solved in a purely numerical fashion. Next to the object geometry, the buckling mode is a function of the curing rate ζ_E which is defined as the stiffness increase after deposition of the material. This increase can be described as linear, exponentially decaying or quadratic. An exponentially decaying increase shows an initial accelerated curing when adding accelerators and subsequently converges to a horizontal asymptote, see fig. 2.8a. The quadratic increase initially follows a linear path, but diverges at larger printing time due to heating up of the printer system, see fig. 2.8b [27]. The linear or quadratic increase of the elastic modulus, respectively, can be described as:

$$E(t) = E_0 \left(1 + \zeta_E^l t \right) \tag{2.5a}$$

$$E(t) = E_0 \left(1 + \zeta_E^l t + \beta (\zeta_E^l)^2 t^2 \right) \tag{2.5b}$$

where E_0 is the initial elastic stiffness, t is the curing time, ζ_E^l is the linear curing rate and β is a calibration factor. Experiments performed by Wolfs and Suiker [27] on the Weber 3D 145-2 mixture found a good fit for $\beta = 2.5$, see fig. 2.8b. This result is contrast with the linearly increasing stiffness found in fig. 2.7d. This is

because the tests were performed on cylindrical cast specimens, not subject to influences from the printing process. Assuming a linear increase yields a conservative result, because in reality the curing rate will increase in time due to the heating up of the printer system.

(a) Linear or exponentially decaying curing processes for the Young's Modulus of elasticity, also applicable to the strength of the material. Figure adopted from [2].

(b) Critical buckling length for a free wall assuming a linear and quadratic curing rate. Assuming the linear increase is conservative, while the quadratic curing more accurately fits the experimental results. Figure adopted from [27].

Figure 2.8: Three possible curing regimes: linear, exponentially decaying or quadratic.

For calculating the critical height of free wall, the closed-form approximation presented in eq. (2.6) can be used. For a simply supported and fully clamped wall, the design graphs in fig. 2.9 are presented in the corresponding publication to derive the critical buckling height as a function of the dimensionless linear curing rate and the wall length s. Note: be aware of the different notations adopted in this research. The parameter $\overline{b}$ in fig. 2.9 refers to the parameter $\overline{s}$ being the length of the wall (see fig. 2.2), which can be calculated using eq. (2.7f). From fig. 2.9 it is obvious that for a clamped-clamped configuration, the critical buckling height goes to ∞ for higher values of $\overline{b}$, especially for higher curing rates. If a rectangular 3DCP structure is analysed, the simply-supported configuration provides a lower-bound, without the need for calculating the degree of restraint provided by the supporting walls.

$$\overline{l}_{cr} = 1.98635 + c\left(\overline{\zeta}_E^l\right)^m \tag{2.6}$$

where:

$$c = 0.996 + 2.328\beta + 0.268\beta^2 \tag{2.7a}$$

$$m = 0.793 + 1.300(1 - \exp(-2.762\beta)) \tag{2.7b}$$

$$\overline{l}_{cr} = \left(\frac{\rho_f g b}{D_0}\right)^{1/3} l_{cr} \tag{2.7c}$$

$$\overline{\zeta}_E^l = \left(\frac{D_0}{\rho_f g b}\right)^{1/3} \frac{\zeta_E^l}{i} \tag{2.7d}$$

$$D_0 = \frac{E_0 b^3}{12(1 - v^2)} \tag{2.7e}$$

$$\overline{s} = \left(\frac{\rho_f g b}{D_0}\right)^{1/3} s \tag{2.7f}$$

The model is validated by comparing the analytical, experimental and numerical results of a free wall and a rectangular box structure. The results showed that the prediction model yields a reasonably accurate and conservative value for the critical buckling height (which was governing in the validation study). The somewhat lower result can be explained by the reported significant spread in the material properties that were measured. To conclude, it is noted that the model can only be applied to linear, prismatic structures i.e.
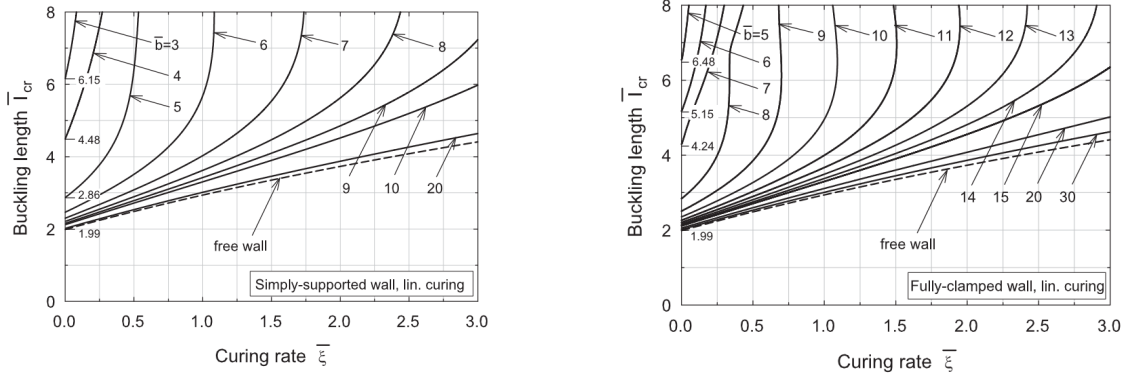
(a) Dimensionless buckling height $\overline{l_{cr}}$ for a simply supported wall as a function of $\overline{\zeta_E^l}$ (2.7d) for various wall lengths $\overline{b} = \overline{s}$ (2.7f).

(b) Dimensionless buckling height $\overline{l_{cr}}$ for a clamped wall as a function of $\overline{\zeta_E^l}$ (2.7d) for various wall lengths $\overline{b} = \overline{s}$ (2.7f)

Figure 2.9: Design graphs to obtain the critical buckling height for two support configurations, both figures are from [2].

without cantilevering layers. For more complex wall lay-outs, predicting the maximum element height using numerical modelling is preferred.

Plastic collapse
Plastic collapse refers to reaching the yield strength in the bottom layer of the structure, at which point it is assumed the structure has failed. Three different strength-based failure models are found in literature and briefly discussed hereafter.

- The model of Suiker allows assuming a linear (eq.(2.8)) or exponential curing process (not discussed in detail here):

$$\sigma(t) = \sigma_0 \left(1 + \zeta_\sigma^l t\right) \tag{2.8}$$

  For a linear curing process and when assuming a compression failure, the maximum object height is equal to:

$$l_p = \frac{\sigma_0}{\rho g - \zeta_\sigma^l \sigma_0 / \dot{l}}, \tag{2.9}$$

  with σ_0 the material compressive yield strength at the onset of printing, $\dot{l}$ is the vertical building rate equal to $d \cdot v / S$ with S the layer contour length and ζ_σ^l the linear curing rate of the strength. When assuming a shear-based failure according to eq. (2.4) instead of a compression-based failure i.e. when $\sigma(t) = \tau(t)$, the terms ρg in eq. (2.9) should be replaced by $\rho g / \sqrt{3}$.

- Rewriting the thixotropy requirement derived by Roussel [10] yields the following expression for the maximum object height before plastic collapse:

$$l_p = \frac{\tau_0}{\rho g / \sqrt{3} - A_{thix} / \dot{l}} \tag{2.10}$$

  which is similar to eq. (2.9) after substitution of $A_{thix} = \zeta_\sigma^l \sigma_0$.

- Based on the bi-linear thixotropy model discussed in the previous section, Kruger et al. [23] developed an analytical model to predict the maximum number of layers before failure occurs, again based on rheological characteristics. The plastic collapse model described by Suiker [2] using the Mohr-Coulomb failure criterion requires several input parameters which can be determined based on experiments. This is a labor-intensive task and therefore, Kruger proposed a simplified model based on the principal stress state. For larger aspect ratios, unconfined regions are present due to uniaxial stress states, resulting in a lower resistance (see left part of fig. 2.10). This effect is accounted for by a strength correction factor as a function of the aspect ratio (right part of fig. 2.10).

  The yield strength must keep up with the increasing self-weight of the structure, yielding the following buildability criterion. If:

$$\frac{\rho g h_l v \cdot 10^{-3}}{2 S F_{AR}} \geq \frac{\tau_{S,i} R_{thix}}{\tau_{S,i} - \tau_D} \tag{2.11}$$
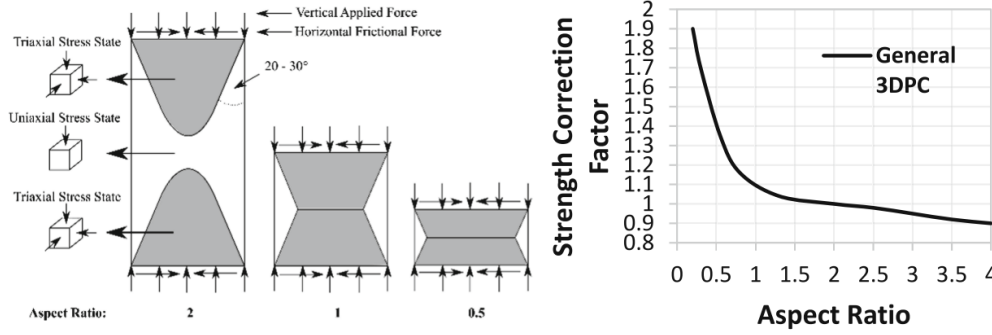
Figure 2.10: Left: presence of unconfined regions for larger aspect ratios. Right: strength correction factor accounting for this effect, as a function of the aspect ratio. Both are from [23].

then use:

$$N_L = -\frac{\tau_D}{\frac{R_{thix}S}{v} - \frac{\rho g h_l}{2\cdot 10^3 F_{AR}}} \tag{2.12}$$

else use:

$$N_L = -\frac{\tau_{S,i} + \frac{A_{thix}(\tau_D - \tau_{S,i})}{R_{thix}}}{\frac{A_{thix}S}{v} - \frac{\rho g h_l}{2\cdot 10^3 F_{AR}}} \tag{2.13}$$

with F_{AR} the strength correction function in fig. 2.10 which can be derived from experiments or approximated as follows [21]:

$$F_{AR} = -0.067x^5 + 0.5852x^4 - 2.1837x^3 + 4.0386x^2 - 3.8195x + 2.535 \tag{2.14}$$

where $x = d/b$. This approximation is especially accurate for aspect ratios smaller than 2, which is not expected to be problematic as low aspect ratios are typical for 3DCP processes.

Note that this model can also be applied when assuming a linear thixotropy model, by using eq. (2.12). Then, $R_{thix} = A_{thix}$ and $\tau_D = \sigma_0$. By doing so and after substituting $l_p = N_L d$, this model is similar to the previously described models. The only deviation is the difference between the strength correction factor and the factor $\sqrt{3}$. Generally, for larger aspect ratios, this model prediction is more conservative.

Before concluding this section, two closing remarks are made.

- It must be noted that the parameters describing the layer-geometry in the models that have been discussed are defined as the actual layer-geometry after deposition, independent of the nozzle size. In reality however, the layer will deform after deposition. The material flow after extrusion is a very complex mechanism, depending on the material rheology, nozzle geometry and pump-pressure. It is possible to model this flow and thereby predict the final layer-geometry, but this requires the aid of complex computational flow dynamics simulations.

- The plastic collapse length is dependent on the material properties and layer-dimensions only. If the layer print time is large, this length reaches towards infinity if the increase in self-weight in time is smaller than the time-dependent strength increase. The critical buckling length however is dependent on the wall geometry as well, thereby not able to reach this asymptote. Therefore, it is expected that failure by elastic buckling is governing for large print-paths i.e. large layer printing times.

2.2.4. Inter-layer bond strength
The findings from the previous sections might suggest that a rapid strength and stiffness development in time is always favourable. However, if the concrete structuration develops fast, or if the time-gap between two subsequent layers is low, poor inter-layer bond is obtained [10, 28–30]. A weak inter-layer bond is due to the limited intermixing of layers and presence of micro-pores. The direct consequence of a reduced inter-layer bond strength is the formation of cold joints, resulting in an orthotropic material behaviour in the final, hardened state. Typically, structures printed with a material having a high thixotropy i.e. stiff materials experience weak interlayer bond strengths. This can be solved by changing the thixotropic properties of the

material, by limiting the time-gap between the deposition of two subsequent layers or by covering the exposed layer, although this is not a very practical solution.
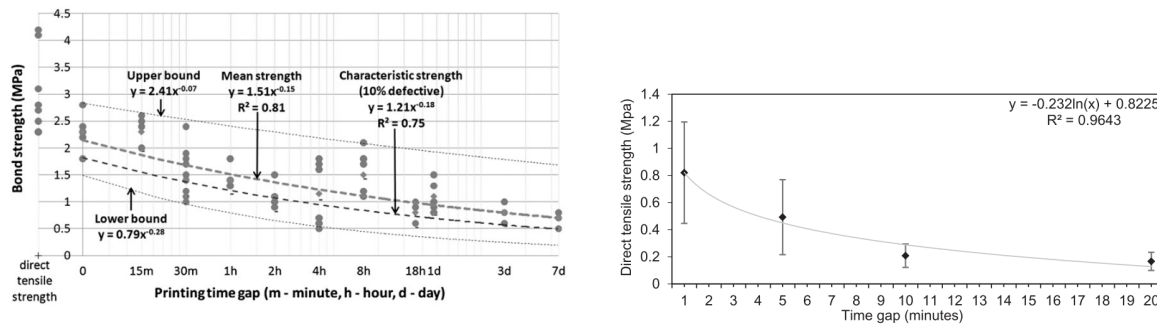
(a) Decreasing bond strength for increasing time intervals (high-performance fiber reinforced mix), from [28].

(b) Decreasing bond strength for increasing time intervals, from [30].

Figure 2.11: Two different relations for a decreasing bond-strength as a function of the interval time between two subsequent layers.

Several researchers studied the potential decrease in bond strength for samples printed with increasing layer print times. Le at al. [28] reported the relations shown in fig. 2.11a and Tay et al. [30] derived the relation between direct tensile strength and time gap from rheological experiments as shown in fig. 2.11b. Note that the decrease reported by Tay et al. is more pronounced than the decrease reported by Le at al.. This emphasizes the fact that the inter-layer bond strength does not solely depend on time, but also on the fresh material properties and process characteristics. A few factors reported in literature that influence the degree of the decrease in inter-layer bond strength in time are highlighted hereafter.

- According to [31], the moisture content on the surface has a large effect on the inter-layer bond strength. Specimens with dry surfaces develop a lower inter-layer strength. Similar conclusions were drawn by Wolfs et al. [32], who reported a higher direction dependency for sample surfaces that were suscept to drying. Keita et al. [33] additionally reports the influence of temperature and relative humidity (RH) on the drying rate. Printable concretes typically contain accelerators to increase the structuration rate, leading to a heat increase at early ages and consequently increasing the drying rate yielding a lower bond strength. In practice, slightly colder water is used for concrete mixing, compensating for the generated heat. Roussel [10] showed that covering the exposed layer surfaces solves this problem, as after a resting time of 5h a strength reduction of only 10% was obtained.

- Nerella et al. [15] reported a lower bond-strength decrease for a concrete mixture with pozzolanic additives compared to a mixture containing Portland cement as binder material only.

- A positive effect of a lower nozzle stand-off distance on the bond strength was reported by Panda et al. [29]. The increased pressure from slightly pushing the printer head into the concrete filament improves compaction and bond-strength. Wolfs et al however, did not find any relation between the nozzle stand-off distance and the bond-strength [32]. A potential bond-strength decrease is due to a higher porosity between two layers, especially for highly thixotropic materials.

- The same researches [29] reported the influence of the initial yield strength of the material rather than the structuration rate. A lower initial strength i.e. more fluid material can more easily intermix with the previous layer, resulting in a higher bond-strength than obtained for a more stiff material.

It can be concluded that the inter-layer bond strength is a function of the interval time between two subsequent layers. The degree of this decrease is affected by many parameters such as room temperature, RH, nozzle stand-off distance and superficial drying (e.g. due to hydration heat generation) and the precise relations are still an open field for research.

In addition to the horizontal interface between two vertically stacked layers, a vertical interface might be present between two adjacent layers. If these layers have a certain overlap, a monolithic cross-section can be achieved because the material is pressed into the previous layer. However, the length of this minimal required overlap is not known yet and therefore, a decreasing bond-strength between two adjacent layers is not considered.

2.3. Hardened concrete

2.3.1. Mechanical properties

Conventional, plain concrete typically has a relatively low tensile strength compared to its compressive strength and the failure mechanism is typically brittle. The properties of hardened 3D printable concretes are comparable, however the strength properties are not always isotropic. Le et al. [28] found a directional dependency of hardened material properties, due to effects induced by the manufacturing process. Due to limited inter-mixing of subsequent layers, a lower tensile strength and, to a smaller extent, a lower compressive strength perpendicular to the print direction in vertical plane is obtained (orientation I for compressive strength and orientation III for flexural and tensile strength in fig. 2.12). As discussed in section 2.2.4 and reported by Wangler et al. [34], a large number of parameters influence the inter-layer bond strength, while results from the large number of researches quite often contradict and show large scatter [34]. Therefore, deriving a potential reduced strength in vertical direction for given manufacturing process parameters is complicated without performing material tests.

In table 2.2 the hardened material properties are given for three different concrete mix generations of Weber Beamix (currently used in designs made by Witteveen+Bos). The properties for the Weber 3D 115-1 are acquired from Salet et al. [5], who reported anisotropic material properties. The material data of the second mixture generation, the Weber 3D 145-2 are obtained from [35], which turn out to be isotropic. The mechanical properties of a third mixture, the Weber 3D 160 are derived from experiments performed by Weber Beamix (data available to the author). These material properties also show no directional dependency and are therefore assumed isotropic. For the derivation of the material properties based on the data, reference is made to appendix F. The Weber 3D 115-1 is more stiff at t = 0 than the other mixtures, which limits the concrete to properly intermix at the interface. This decreases the bond-strength as discussed in section 2.2.4. Note that the material properties listed in table 2.2 are based on tests performed on small-sized samples printed with small layer print times.
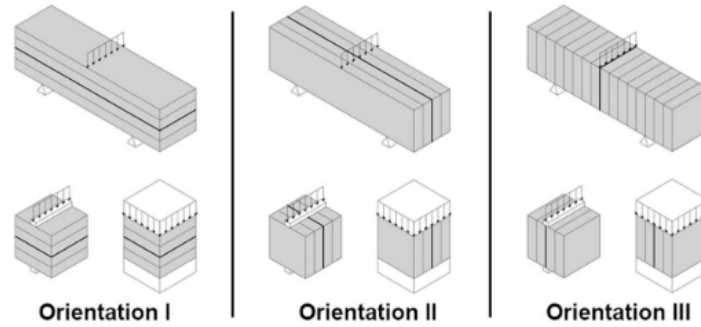

Figure 2.12: Print-layer orientations for testing the flexural tensile strength, tensile strength and compression strength, from [32].

Table 2.2: Hardened material properties of three generations of Weber 3D mixtures. The directional dependent properties for the W-115-1 are sorted as Orientation III; Orientation II; Orientation I in fig. 2.12.

Parameter	Weber 3D 115-1 [5]	Weber 3D 145-2 [35]	Weber 3D 160 (appendix F)
ρ [kg/m^3]	2000	2100	2120
f_{ck} [MPa]	23.3; 21.5; 21.0	28.51	30
f_{ctk} [MPa]	1.9; 1.6; 1.3	3.68	4.86
E [MPa]	19000	30000	30000

For a building sequence in which the element is rotated 90°i.e. when an element is loaded in bending according to Orientation III in fig. 2.12, a decreased inter-layer bond strength directly influences the flexural tensile strength and shear strength of the structure. As the tensile strength is typically a critical parameter in concrete design, it is important to study the effect of a potentially reduced bond-strength on the structural performance.

2.3.2. Reinforcement

Because concrete has a low tensile strength and fails in a brittle behaviour, it is desired to add steel reinforcement to the structure to increase ductility. However, the application of traditional reinforcement bars in 3D concrete printed structures is not trivial. Therefore, other methods for obtaining ductility are proposed, such as the in-process printing of a steel reinforcing cable or the addition of steel fibres in the concrete mix. These two methods are discussed hereafter, for other solutions see [36].

In-print reinforcement cable

In this reinforcement solution, a steel wire cable with diameter of about 1mm is embedded in the concrete filament during printing. This is only possible when using a rectangular nozzle using back-flow. A wire coil is mounted at the printer-head and the steel cable must be flexible enough to follow the complex lines of the printing-path. Experimental results show that significant post-crack behaviour could be achieved using the cable, but with substantial scatter. The scatter might be caused by the inclusion of small voids under the cable due to poor compaction of the concrete around the cable. However, the bond strength between the cable and printed concrete is low, which may cause slipping of the reinforcement cable. If the concrete is stronger than the cable, which is likely, cable breakage might occur [37]. An additional, more practical disadvantage is that when printing with an in-print reinforcement cable, the horizontal printing velocity is limited to 120 °/s. This means that for a sharp bend (i.e. radius = layer width) in the print-path with an angle of 90 °and a layer width of 50 mm, the maximum print velocity is equal to 52.4 mm/s, which is much smaller than the maximum print speed of 180 mm/s reported in section 2.1.

Figure 2.13: Entrainment of reinforcement cable in concrete filament during printing, from [37].

Printable fibre reinforced concrete

In conventional concretes, the concept of reinforcing with fibres has already been used to improve ductility without the need for reinforcement, or to reduce shrinkage cracking. The same concept could be applied to printable concrete to achieve ductility, as long as the fibres are small enough to pass through the nozzle. Panda et al. [16], found a significant increase in flexural and tensile strength for a concrete with the inclusion of 1% glass fibres. However, the strength was highly directional dependent due to the orientation of the fibres into the print direction. Bos et al. [38] reported an increase in flexural strength with the inclusion of steel fibres in the Weber 3D 115-1 mixture yielding a behaviour similar to cast fiber-reinforced concrete specimens.

2.4. Time dependent material behaviour

When restrained, shrinkage strains which occur upon the material's response to external load and environment, lead to tensile stresses resulting in concrete cracking. Moreover, the combined effect of shrinkage and creep leads to prestress losses which should be accounted for in design. In this section, the basic concepts are described and some important material properties are derived. All information is derived from the books of Mehta et al. [39] and van Breugel et al. [40].

During concrete hardening, the following shrinkage mechanisms can be distinguished.

- In a fresh cast (or printed) specimen, the heavy particles of the mix move down upon which water travels to the surface, forming a thin water layer. This water evaporates to the surroundings, which can happen quite fast, depending on the temperature and wind. This causes **plastic shrinkage**, yielding tensile stresses in the young concrete, quite often leading to cracks. It can be prevented by keeping the surface wet or by preventing moisture loss by covering the surface with e.g. a foil. An other measure is adding a small amount of polypropylene fibres to the mixture, which prevents cracking (not the shrinkage itself).

- During concrete hardening, which is the exothermic reaction between cement compounds and water, a substantial temperature rise can be observed, especially for high cement contents. Upon the subsequent cooling of the fresh structure, **thermal shrinkage** strains are induced. Because printable concretes typically have a high cement content, high temperature rises can be expected. However, a 3DCP structure is typically rather hollow with a relatively large surface area, so it is expected that the excess heat can be exchanged with the environment relatively easy. Thermal shrinkage can be controlled by a) precooling the initial concrete by using chilled aggregates or colder water or b) by controlling the adiabatic temperature rise. The latter is a function of the amount, composition and fineness of the cement. For example, the replacement of Type I OPC with a pozzolanic binder reduces the temperature rise with about 10 °C. The thermal properties of printable concrete are mainly dependent on the cement content. The values are based on relations from literature and are summarized in table 2.3. The adiabatic

| property	symbol	value	motivation
thermal expansion	α_T	1e-5 1/ °C	common adopted conservative value [39]
conductivity	λ_c	2.75 W/(m °C)	strongly depends on aggregate size, so based on saturated sand [41]
thermal capacity	$\rho_c c_c$	$1.6 \cdot 10^6$ J/(m^3 °C)	assuming $c_c = 1$ for low water content [40]

Table 2.3: Estimated thermal properties of printable concrete

  temperature rise of a 3DCP specimen has not been measured yet (to the best of the author's knowledge), but the adiabatic heat curve (b) shown in fig. 2.14 for a high strength concrete (HSC) mortar is likely applicable since HSC mixtures typically contain a high cement-content as well.

- Because the volume of hydration products is smaller than the initial volume of water+binders, **chemical shrinkage** occurs. In general, this does not result in a gross volume decrease, but in the formation of pores in the micro-structure, thereby not generating significant stresses.

- **Autogeneous shrinkage** is the result of a contraction of the structure, where the water loss is attributed by the cement that reacts with the available water. Especially for low water to binder ratios, autogeneous shrinkage may be substantial. The degree of autogeneous shrinkage strongly depends on the concrete mixture.

After hardening, the structure is prone to **drying shrinkage**, which can continue during the entire lifetime. It is caused by the drying of the structure due to a reduction in RH in the structure. The magnitude of the shrinkage mainly depends on the cement content and the rate depends on the RH of the surroundings and the structure's dimensions. Small sized structures experience very rapid shrinkage deformation, while large structures might crack faster at the surface due to a restriction from the large inner core. If the strains and thus stresses develop slowly, it is likely that these stresses will be partly reduced by relaxation.

Figure 2.14: Adiabatic heat curves for a) a normal strength concrete (C=350 kg/m^3), b) a high strength concrete (C=475 kg/m$^{3)}$ and c) a Granulate blast furnace slag+CEMIII/B concrete.
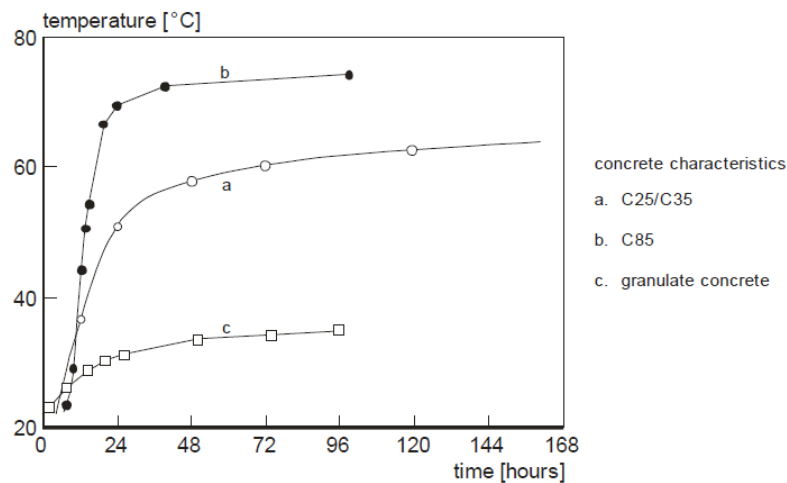
Creep can be defined as the phenomenon of a gradual increase in strain with time under a sustained stress. The phenomenon of a gradual decrease in stress with time under a sustained strain is called **relaxation**. These mechanisms can be attributed to the visco-elastic material behaviour that concrete is associated with. The amount of creep is dependent on the ambient RH, the structural dimensions and the concrete mix composition.

Generally, 75 to 80 % of creep and shrinkage strains develop in the first year, but deformations can increase during the entire lifespan of the structure, up to 100 years. In appendix C.1.1, an overview of the required equations for calculating the creep- and shrinkage deformation as a function of the environmental conditions, geometry and material properties is given. These models have been established through empirical relations. However, due to the high cement content and thin-walled geometry, the applicability of these models is questionable.

2.5. Summary

This chapter provides a summary of a thorough literature study on the printing process and the material properties of printable concrete. The most important findings are listed below.

- The printable concrete is extruded through a nozzle, mounted at a digitally controlled robot arm or gantry system. The mix typically contains a relatively high cement content and a low aggregate size < 2 mm. The printer can be located off site or on site. Using 3D concrete printing as a construction method, the freedom or form increases due to the absence of formwork, but certain geometrical limitations do exist.

- Because a fresh 3DCP element is unsupported, the structure must be strong, stable and stiff enough to carry the weight of the subsequent layers. After extrusion, the concrete material starts developing strength and stiffness in time due to the thixotropic material behaviour. If this development is not fast enough, the structure fails by elastic buckling or plastic collapse. The maximal object height before failure can be predicted based on the material properties, process characteristics and geometry. Analytical models have been developed to predict the object height at failure. For elastic buckling, the use of numerical prediction models is preferred in case of more complex geometries.

- The material properties of the final, hardened structure can be isotropic if the layer print time is short enough. However, depending on the environmental conditions, fresh material properties, tool-path geometry and print velocity, the bond-strength between two subsequent layers may decrease, yielding orthotropic material behaviour.

- The inclusion of traditional reinforcement in 3DCP structures is not trivial. It is possible to provide ductility by embedding a small reinforcement cable into the concrete filament or by adding fibers into the concrete mixture.

- Because the cement content of printable concretes is high with small aggregate sizes, the time dependent deformations are expected to be higher than for conventional concretes. Existing creep- and shrinkage models are established using empirical relations and therefore, the applicability of these models is questionable.

3

3D concrete printed bridge design

3.1. Design concept

3.1.1. Introduction: existing bridges

As mentioned in chapter 1, a prestressed 3DCP cyclist bridge is the type of structure that is analysed in this research. 3DCP as a construction method for cyclist bridges has hitherto been applied on simply-supported systems only. In this section, the design principle of two existing 3DCP bridges in Gemert and Nijmegen will be elaborated on. In these hybrid structures, 3DCP deck elements are combined with conventional concrete anchor blocks and post-tensioned prestressing tendons. Large benefit of using 3DCP elements over prefab elements for the deck is the possibility of having curved, aesthetic details, which can be created easily using 3DCP. The gross cross-section is kept simple, since this part is not visible on the outside. A similar design will be applied to new cyclist bridges that are currently being designed for the Dutch province of Noord-Holland. This existing bridge design concept is the starting point for the bridge designs treated in this research.

Gemert

The 3DCP bridge in Gemert is a simply supported cyclist- and pedestrian bridge opened for public in 2017 (see fig. 1.1 and fig. 3.1a). It has a 6.5 m span and is 3.5 m wide, consisting out of 6 printed elements of 89-90 concrete layers size 60x12mm. After printing, the elements are rotated 90 degrees, connected with an epoxy-based binder and pressed together using 16 straight prestressing Dywidag (Ø15.7 mm, Y1860 steel grade) cables. Prestressing is necessary to create a compression-only structure as the concrete is unreinforced and therefore has very limited tensile capacity. The tendons are placed in openings in the cross-section and an initial force of 150 kN is introduced through traditional reinforced concrete anchor blocks at both ends. Additionally, a thin reinforcement cable was embedded in the concrete filament to increase the ductility (see section 2.3.2). The cross-section has a bottle-shaped topology which is designed to provide resistance against buckling during printing of the fresh concrete, see fig. 3.1b. The two anchor blocks at the ends of the bridge rest on two traditional abutments with a pile foundation. A 90mm traditional concrete compression layer with reinforcement mesh (Ø8mm-#100) was added, providing some diaphragm action and distributing local loads. Finally, a thin wear layer is added. The bridge is printed with the Weber 3D 115-1 print mortar from concrete mix supplier Weber Beamix and printed at the printing facility at TU/e [5].

Nijmegen

A second bridge structure using 3DCP material is designed for the Dutch city Nijmegen. To show the possibility of creating freeform structures using 3DCP, a design similar to the Verlengde Waalbrug was made (see fig. 3.2). This bridge contains many double-curved surfaces, which is labour intensive and expensive to built using conventional concrete. The 3DCP version has a length of 29m, consisting of four supports. The cross-section is similar to the one in Gemert, having a bottle-shaped topology and is printed with the Weber 3D 160 mortar. The bridge elements have already been printed and will be assembled soon.

3.1.2. New design

The 3DCP bridge designs analysed in this research are based on a new design proposed by Witteveen+Bos for a project in the Dutch province Noord-Holland. Four new bridges are to be built, all of them made of

(a) Artist impression, from [5]

(b) 3D concrete printing of bridge elements Gemert at TU/e, from [42]

Figure 3.1: 3D concrete printed bridge Gemert

Figure 3.2: Artist Impression of the 3DCP bridge project in Nijmegen, from [43].

3D printed concrete, but each having different design requirements. Unlike the previously applied bottle-shape, these bridges will have a box-girder cross-section topology. This more slender design is considered to be a more economical alternative and this type of cross-section is applied in numerous existing bridges made of both steel and concrete. The shear stresses are taken by the webs and the normal stresses by the flanges. These cross-section topologies have a high torsional stiffness, which is beneficial in case of eccentric loading.

3DCP allows for printing curved details at the bridge edges, which improves the aesthetics of the structure without the production of complex formwork, see the left part of fig. 3.3. The basic, load bearing structure is a straight box-girder. For simplicity, the curved details are modelled as straight parts in this research, see the right part of fig. 3.3. In this research it is assumed that the parapet is mounted at the anchor blocks. In fig. 3.4 a simplified 3D representation of the bridge design is shown. Apart from the cross-section topology, the design concept is similar to the existing designs. Tensile stresses will be reduced by prestressing introduced at two RC anchor blocks and the bridge elements (in total N elements) are connected using an epoxy binder. Local loads are distributed via a concrete compression layer, finished with a wear layer (not drawn in fig. 3.4). The basic design variables of the bridge geometry are indicated symbolically in fig. 3.4, together with the linear prestressing tendons having an eccentricity e_p. The parameter a denotes a certain offset at mid-span with which the height of the structure is reduced, yielding a non-prismatic beam. The value of this parameter is initially set to zero and analysed more in-depth in chapter 6. The toolpath lay-out for this geometry is depicted in fig. 3.5. The outer webs are printed once and the inner webs are printed twice, yielding a doubled thickness.

3.1.3. Assembly
The 3DCP bridge consists of N elements of length l which are printed in longitudinal y-direction, rotated 90 degrees and then assembled on site. The number of elements depends on the maximum possible object height to prevent failure during printing. The total manufacturing process of the structure is as follows:
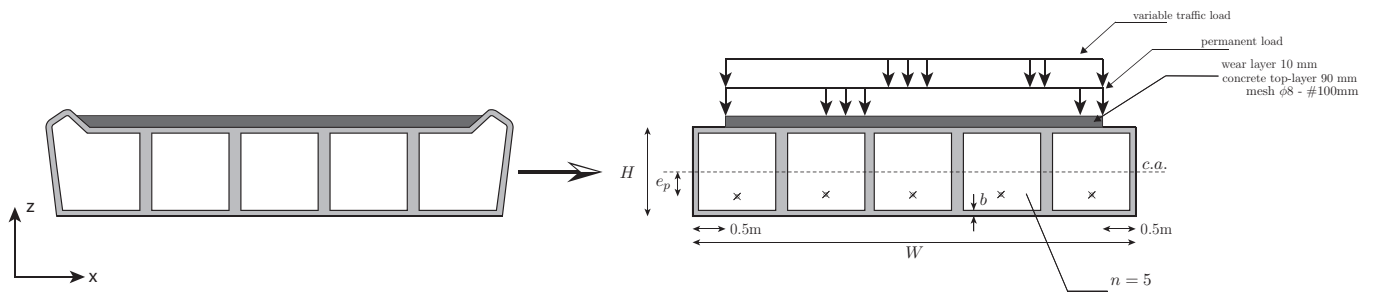
Figure 3.3: Transverse cross-section of a 3DCP box-girder bridge. Left: including aesthetic, curved details and right: simplified model including vertical load definitions.
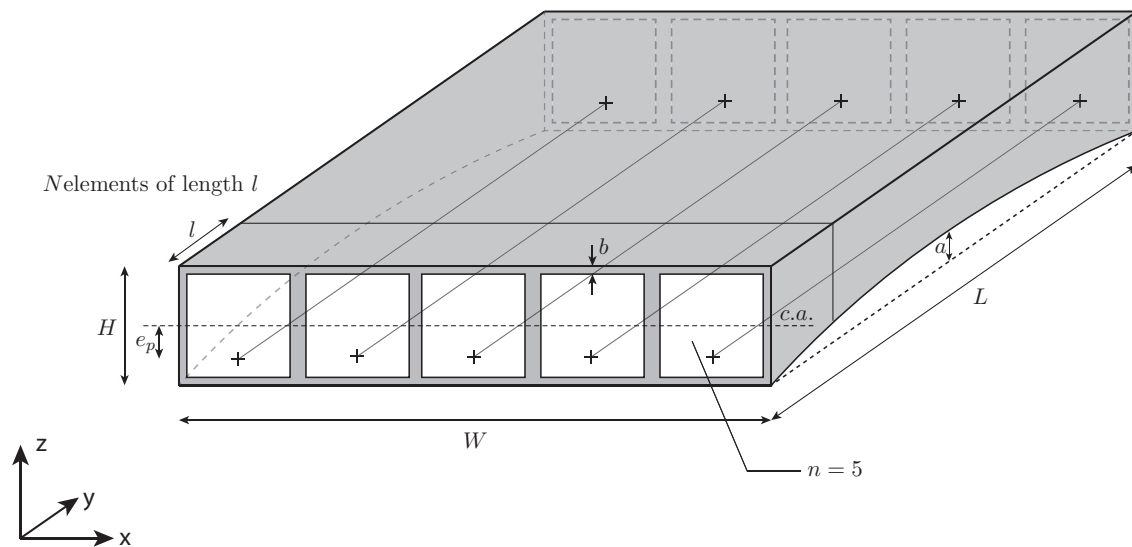

Figure 3.4: 3DCP bridge having a box-girder topology, consisting out of N 3D printed elements with length l.

1. the 3DCP elements are printed, cured and stored in the printing facility hall;

2. the elements are transported to a site close to the final bridge location, rotated 90 degrees and aligned in place;

3. the anchor blocks are placed at the bridge ends and all elements are connected with an epoxy-based binder;

4. prestressing tendons are introduced in the structure and stressed at the anchor blocks;

5. the structure is hoisted into place;

6. finishing of the structure: applying the reinforcement mesh, the concrete top-layer and wear layer and installing the parapet.

3.2. Design validation criteria

3.2.1. Starting points

Each bridge design must satisfy 1) the requests stated in the Design Brief provided by the client (NL: Programma van Eisen) and 2) the design rules and guidelines stated in the Eurocode to guarantee safety. The design loads acting on the bridge are based on the following codes:

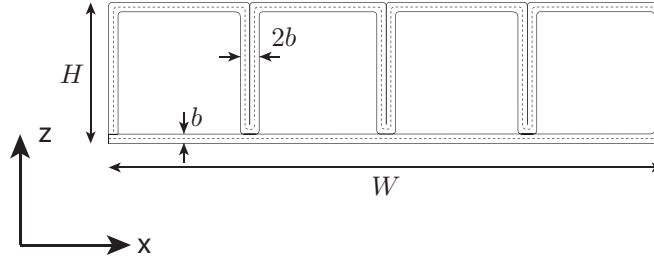- NEN-EN 1990. Eurocode: Basis of structural design [44] and

Figure 3.5: Toolpath of box-girder cross-section topology with length *S*.

- NEN-EN 1991-2. Eurocode 1: Actions on structures - Part 2: Traffic loads on bridges [45].

Since no specific design codes exist for determining the resistance of 3DCP structures, existing guidelines for concrete structures will be used instead, which have been partly proven to be applicable. These are:

- NEN-EN 1992-1-1. Eurocode 2: Design of concrete structures - Part 1-1: General rules and rules for buildings [46] and

- NEN-EN 1992-2. Eurocode 2: Design of concrete structures - Concrete bridges: Design and detailing rules [47].

The Consequence Class is CC2 and the structure is designed for a lifetime of 100 years. Because there is no experience yet with long term effects on 3DCP structures, the degradation process of the bridge structure should be monitored very closely. The considered environment classes for the 3D printed concrete deck are XF and XA to prevent concrete damage, the environment classes XC and XD to prevent corrosion damage are not relevant since the structure is unreinforced. As the prestressing tendons are not embedded in the concrete and can therefore not be protected by the concrete, these must be covered with a plastic hose.

In the remainder of this section, an overview is given from the loads that are acting on the bridge, followed by the calculation of the structural resistance. The dimensioning and design validation of the RC anchor blocks and parapet is not considered in this research; focus is on the 3DCP part.

3.2.2. Design loads
Permanent loads
The following permanent loads are present:

- self-weight of the concrete material;

- 90mm concrete + 10mm wear layer, for which a total load of 5 kN/m^2 is assumed. This is a conservative value to account for the curved parts that have been neglected.

The permanent load is acting between the curbs which have a width of 0.5m on both sides of the bridge, see fig. 3.3.

Variable loads
According to NEN-EN 1991-2, the following traffic loads and corresponding characteristic values should be considered:

- a uniformly distributed load q_{fk} = 5 kN/m^2;

- a concentrated load Q_{fvd} = 7 kN, acting on an area of 0.10m x 0.10m;

- a load representing a service vehicle Q_{serv}:

  1. two axles with a 3m base;

  2. characteristics value for each axle load is 25 kN;

3. each axle contains two wheels spaced 1.75m;

4. 0.25m x 0.25m loading area for each wheel.

The distributed variable load is acting between the curbs which have a width of 0.5m on both sides of the bridge, see fig. 3.3.

If a service vehicle with load Q_{serv} is present, Q_{fvd} does not need to be considered. Only local effects induced by Q_{serv} need to be assessed.

Furthermore, a vertical wind-load equal to 0.5 kN/m^2 and a snow-load equal to 0.56 kN/m^2 are considered. However, it will turn out that these loads are not governing.

Horizontal loads
For pedestrian bridges a horizontal load Q_{flk} needs to be taken into account, acting in longitudinal direction at the level of the top-layer, equal to the maximum of:

- a load corresponding to 10% of the total distributed load, or,

- 60% of the total weight of the service vehicle (if present).

It is assumed that these loads will be distributed to the supports directly via the concrete top layer and will therefore not be considered in detail.

Finally, a horizontal wind-load equal to 0.5 kN/m^2 in transverse direction should be considered. However, it is expected that the bridge is stiff and strong enough in horizontal direction. Therefore, this horizontal load will not be considered.

Imposed deformations
Next to external loads acting on the structure, imposed deformations resulting from shrinkage ϵ_{cs}, creep ϵ_{cc} and temperature gradients ϵ_T must be considered in SLS. In longitudinal direction, the structure shortens due to shrinkage and creep under the prestressing force. The total axial imposed deformation is equal to:

$$\epsilon_{c,y}(t) = \epsilon_{cs} + \epsilon_{cc}, \tag{3.1}$$

which will lead to a decrease in the initial amount of prestress ΔP.

Additionally, a temperature gradient can develop over the height of the structure upon heating up of the asphalt, equal to:

$$\kappa(\Delta T_b) = \frac{\alpha_T \Delta T_b}{\frac{1}{2}H}. \tag{3.2}$$

However, as the bridge is simply-supported this deformation is unrestrained, not causing any stresses.

In vertical (z) and transverse (x) direction shrinkage strains $\epsilon_{c,xz}$ develop. Depending on the degree of restraint these might induce tensile stresses causing the structure to crack.

To calculate the magnitude of these imposed strains, it is assumed that design guidelines for conventional concrete structures can be applied. These strains can be calculated as a function of the structural dimensions, cement type, aggregate type and RH. The corresponding formulas can be found in appendix C.1. It is noted that in reality, the time dependent deformations are likely to be larger, since these formulas are based on standard concrete compositions having larger aggregates. However, these relations will give a rough estimate of the imposed strains.

Prestressing
To control the tensile stresses at the bottom side of the bridge at mid-span resulting from the loads acting on the structure, the structure is prestressed using post-tensioned tendons. The total applied initial prestress is equal to P_{m0} and is introduced at both ends through conventional concrete blocks with spiral reinforcement to distribute the spalling forces from prestress-introduction. As a consequence, the prestressing load is introduced at the 3DCP structure as a uniformly distributed load over the width of the beam. In the design, strands of steel quality Y1860S7 are used. In each inner core, a linear tendon is installed, with a tendon eccentricity e_p (see fig. 3.6). Because of the size of the anchors, the tendon must be located at least 100 mm from the bottom of the cross-section.
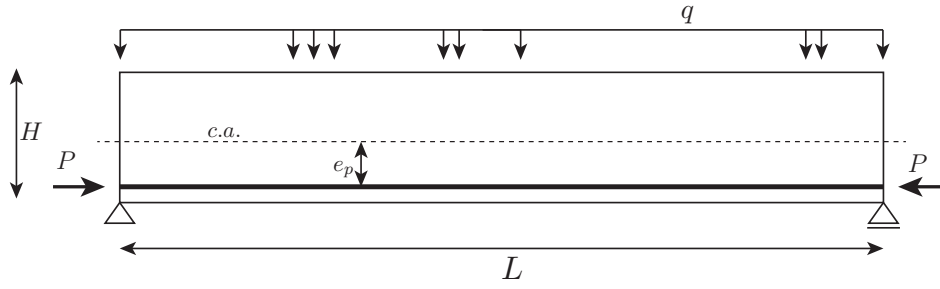
Figure 3.6: Longitudinal cross-section of 3DCP bridge in case of a linear tendon profile

In time, the prestressing force P_{max} decreases due to direct losses upon anchoring and due to time dependent stress losses. In this early design stage, it can be assumed that the initial elastic losses are compensated for by overstressing and that the total prestress losses due to time-dependent deformation of the concrete are 20% of the initial force: $P_{m,\infty} = 0.8 P_{m0}$. Friction does not need to be taken into account, as the tendons are fully unbonded.

The minimal amount of prestressing is calculated based on the design requirements at mid-span specified by the client. Two different possibilities can be assumed:

- requiring a compression-only structure in SLS under the frequent load-combination (common practice) or;

- ensuring that the tensile stress in ULS is nowhere larger than the concrete design tensile strength f_{ctd}.

For determining these stress-levels, the full load should be present together with the working prestress force P_m. In addition, it must be verified if the tensile stress due to the tendon eccentricity e_P at the top-fiber at support-level does not exceed the tensile strength requirement. For this check the construction stage is governing in which only the self-weight and the initial prestress P_{m0} are present.

Finally, to prevent failure of the tendons and local crushing of the concrete during stressing, there is a maximum amount of prestress that can be applied to the structure. The following guidelines are provided by clauses 5.10.2.1 and -2 of NEN-EN 1992-1-1:

- during prestressing, the prestressing force must be lower than $P_{max} = A_p \sigma_{p,max}$ with $\sigma_{p,max} = 1488$ MPa;

- the concrete compressive stress during stressing of the tendons must remain below $\sigma_c \le 0.6 f_{ck}$;

Load combinations
The less favourable of following two equations should be considered as the governing load combination in ULS (Ultimate Limit State) (NEN-EN 1990+A1+A1/C2 6.4.3 (6.10)):

$$\sum_{j\ge1} \gamma_{G,j} \cdot G_{k,j} + \gamma_P \cdot P + \gamma_{Q,1} \cdot \psi_{0,1} \cdot Q_{k,1} + \sum_{i>1} \gamma_{Q,i} \cdot \psi_{0,i} \cdot Q_{k,i} \tag{3.3a}$$

$$\sum_{j\ge1} \xi_j \cdot \gamma_{G,j} \cdot G_{k,j} + \gamma_P \cdot P + \gamma_{Q,1} \cdot Q_{k,1} + \sum_{i>1} \gamma_{Q,i} \cdot \psi_{0,i} \cdot Q_{k,i} \tag{3.3b}$$

The values for γ and ψ_0 in eq. (3.3) are specified in the NA and given in fig. 3.7 and fig. 3.8, respectively.

In the NA for NEN-EN 1992-1-1, it is stated that $\gamma_P = 1.0$ if it has a favourable effect and that $\gamma_P = 1.2$ when it has an unfavourable effect.

According to NEN-EN 1990+A1+A1/C2 6.5.3 (6.14b), the characteristic load combination in SLS (used for reversible limit states such as checking deflections and discomfort of the structure) is formulated as:

$$\sum_{j\ge1} G_{k,j} + P + Q_{k,1} + \sum_{i>1} \psi_{0,i} \cdot Q_{k,i} \tag{3.4}$$

Tabel NB.13 – A2.4(B) — Belastingsfactoren voor wegverkeersbruggen en bruggen voor langzaam verkeer en voetgangers- en fietsbruggen STR/GEO) (groep B)

Gevolgklasse	β	G			Verkeer (met $\psi = 1$)	Overig veranderlijk (met $\psi = 1$)
		$\gamma_{G,j,sup}$		$\gamma_{G,j,inf}$		
		6.10a	6.10b (incl. ξ)	6.10a en 6.10b		
CC1	3,3	1,20	1,10	0,9	1,20	1,35
CC2	3,8	1,30	1,20	0,9	1,35	1,5
CC3	4,3	1,40	1,25	0,9	1,5	1,65

γ = 0 voor gunstig werkende veranderlijke belastingen

Voor γ_P zie de aanbevelingen in de desbetreffende materiaalgebonden Eurocodes 1992 t.m. 1999.

Voor de berekening van het effect van ongelijkmatige zettingen geldt dat $\gamma_{G,set}$ = 1,20 in het geval van een lineaire berekening en $\gamma_{G,set}$ = 1,35 in het geval van een niet lineaire berekening. Gunstig werkende zettingsverschillen worden niet in rekening gebracht. De grootte van de zettingen is bepaald op basis van de karakteristieke belastingscombinatie en de karakteristieke waarden voor de grondeigenschappen.

OPMERKING   De factor K_{FI} volgens B 3.3 is in de waarden van γ verwerkt; voor de zettingsberekening blijft de betrouwbaarheidsdifferentiatie achterwege.

Figure 3.7: NEN-EN 1990 table NB.13-A2.4(B): γ-factors for pedestrian- and cyclistbridges.

According to NEN-EN 1990+A1+A1/C2 6.5.3 (6.15b), the frequent combination in SLS (used for checking crack widths and thus calculating the required prestress) is formulated as:

$$\sum_{j \geq 1} G_{k,j} + P + \psi_{1,1} \cdot Q_{k,1} + \sum_{i > 1} \psi_{2,i} \cdot Q_{k,i} \tag{3.5}$$

3.2.3. Design requirements
SLS: deformations
NEN-EN 1992-1-1 7.4.1 (4) states that deflections (induced under the characteristic load combination) larger than L/250 mitigate the appearance and functionality of the structure. This criterion is adopted as a limit to the maximum allowed deflection at mid-span.

SLS: dynamic behaviour
In NEN-EN 1990 Annex A2.4.3.2 it is stated that a detailed dynamic validation must be performed if the eigen-frequency ω_n is smaller than:

- 5 Hz for vertical vibrations;

- 2.5 Hz for horizontal vibrations.

If it does turn out that for slender structures with a lower natural frequency a dynamic analysis is required, this will be mentioned but the analysis itself is considered to be out of this research' scope.

SLS: cracking
In longitudinal direction, high tensile stresses are compensated for by applying sufficient prestress. However in *transverse* and *vertical* direction, no prestressing can be applied to control tensile stresses. Inspections performed on the 3DCP bridge in Gemert have shown that cracks are present in the structure, see fig. 3.9. It is feasible that the cracks are induced by restrained shrinkage strains. Therefore, it must be validated if these strains can lead to cracking of the structure.

Finally, the probability of cracking in the young, hardening concrete should be investigated. As the cement content is high, tensile stresses induced by thermal- and autogeneous shrinkage are likely to be rather high. Moreover, a strain gradient might develop over the webs if the drying conditions on the inside and outside can be different. As the webs are thin, cracks might easy propagate through the entire web. It is desired to separately address the probability of cracking in the young concrete element.

Figure 3.8: NEN-EN 1990 table NB.10-A2.2 - ψ-factors for pedestrian- and cyclistbridges.

ULS: shear strength

The equations in the Eurocode for calculating the shear resistance $V_{Rd,c}$ of a concrete member are based on empirical relationships from tests performed on reinforced concrete members. Therefore, the applicability of these relations for unreinforced 3D concrete printed members is questionable. Moreover, aggregate interlock delivers an important contribution to the concrete shear capacity, while 3D printable concretes typically have low aggregate sizes. However, these relations will be used as a starting point. Several relations from Eurocode based on different assumptions are listed below:

- NEN-EN 1992-1-1 eq. (6.2.a), elements without shear reinforcement:

$$V_{Rd,c} = \left[C_{Rd,c} k (100 \rho_l f_{ck})^{1/3} + k_1 \sigma_{cp} \right] b_w d \tag{3.6}$$

with a minimum of:

$$V_{Rd,c} = \left(v_{min} + k_1 \sigma_{cp} \right) b_w d \tag{3.7}$$

where $\rho_l = 0$ (no reinforcement), $k_1 = 0.15$, $\sigma_{cp} = P/A$ (normal stress from prestress), $d = h$ in the absence of reinforcement and b_w is the smallest width (lateral direction) of the tensile zone. v_{min} is the minimum shear force resistance for plain concrete:

$$v_{min} = 0.035 k^{3/2} f_{ck}^{1/2} \tag{3.8}$$

where $k = 1.0$.

- NEN-EN 1992-1-1 eq. (6.4), uncracked elements without shear reinforcement: if the tensile stresses in a member are smaller than f_{ctd} i.e. uncracked, the shear resistance is:

$$V_{Rd,c} = \frac{I b_w}{S} \sqrt{f_{ctd}^2 + \alpha_l \sigma_{cp} f_{ctd}} \tag{3.9}$$

in which $\alpha_l = 1.0$, I is the moment of inertia and S is the section modulus of the cross-section.

(a) Crack close to the support of the bridge due to tensile stresses in vertical direction

(b) Crack at the bottom of the bridge due to tensile stresses in transverse direction

Figure 3.9: Cracks present in 3DCP bridge, Gemert (pictures from an internal maintenance report written by BAM).

Equation (3.6) is more conservative and therefore, it is more economical to use eq. (3.9). This is allowed when it can be shown that the structure is uncracked. Assuming eq. (3.9) is applicable is non-conservative and therefore, experiments are currently being designed by Witteveen+Bos to test this assumption on 3DCP box-elements. The maximum shear force is present close to the support so this is the critical location for validating the shear resistance.

ULS: bending
As discussed in the previous section, the prestressing is designed to compensate for the tensile stresses at mid-span. Depending on the tensile strength in the joints between the elements, two different situations can develop upon which the bending resistance is determined. The tensile capacity of the joints depends on numerous aspects, like the tensile strength of the epoxy material, the bond between concrete and epoxy, the roughness of the surface, etc. Because the determination of the exact joint strength is considered out of the scope of this research, two different scenarios are considered.

(A) The tensile strength of the joints is ***higher than*** the concrete strength. When the load is increased, the concrete element at mid-span will crack when reaching the concrete tensile strength. Because no reinforcement is present to redistribute the cracks, this failure is in a brittle, uncontrollable post-crack behaviour. Therefore, in this scenario, it is required for the tensile stress at mid-span to be smaller than the concrete tensile strength. According to NEN-EN 1992-1-1, 12.3.1, due to the low ductility, the bending resistance of an unreinforced concrete structure must be reduced as follows:

$$f_{ctd} = \alpha_{ct,pl} f_{ctk} / \gamma_C, \tag{3.10}$$

in which $\alpha_{ct,pl} = 0.8$, f_{ctk} is the characteristic tensile strength of the material and $\gamma_C = 1.5$. The concrete compressive stress must be smaller than f_{cd} which can be calculated using eq. (3.10) with $\alpha_{cc,pl} = 0.8$.

(B) The joints have ***no tensile strength***: when the load is increased, the joints between the elements will start to open, yielding a kinematic mechanism of two rotating blocks. Therefore, the bending moment resistance should be calculated for this deformed situation in which a mechanism has developed and the bending resistance is fully delivered by the prestressing tendons. It must be verified if the concrete compressive stress and increased prestressing steel stress are not exceeding the strength limits $f_{pk}/\gamma_s = 1691$ MPa and f_{cd}, respectively. Note that this failure mechanism is ductile only if the prestressing tendons are governing and start yielding upon increasing the load. If the concrete in compression is governing, the structure will fail in a brittle manner.

ULS: torsion
NEN-EN 1992-1-1 12.6.4 states that unreinforced concrete elements are not able to take any torsional moments. Torsional moments can be induced by eccentric point-loads or by misalignment of the bridge on the bearing. The presence of eccentric local loads is not likely, since the highest considered load is of a service vehicle. Given its dimensions relative to the bridge width, the vehicle will pass the bridge almost centrically. However, given the brittle behaviour of the structure, the effect of this local eccentric load must be addressed.

3.3. Performance indicators

3.3.1. Introduction

To compare different bridge designs and determine which design is 'best' (discussed in chapter 6), a set of performance indicators is defined. Together with the set of design validation criteria defined in section 3.2.3, the resulting bridge designs can be assessed on both performance and feasibility.

The main purposes of using 3DCP as a building material are the ability to design free-form structures, a decreased environmental impact due to material savings, less construction waste and a decrease of the total construction cost [48]. Therefore, the 3DCP bridge designs studied in this research are assessed based on these promises. Two performance indicators (PI's) are defined: one for assessing the cost effectiveness and one for assessing the environmental impact of the structure.

3.3.2. Cost indicator

The first indicator $f_1(\mathbf{x})$ (3.11) expresses the total cost of the design, dictated by the total mass of the structure, the required amount of prestress, the total printing time and the number of elements.

$$f_1(\mathbf{x}) = \text{\euro}_M \cdot M + \text{\euro}_P \cdot M_P + \text{\euro}_T \cdot T + \text{\euro}_J \cdot J \tag{3.11}$$

in which

- M is the total concrete material weight in [kg];

- M_P is the required amount of prestressing steel [kg];

- T is the required time to print the entire structure [h];

- J is the number of joints present in the structure [-]

- $\text{\euro}_M$ is the price per ton of concrete material equal to €320/ton;

- $\text{\euro}_P$ is the price per kg of prestressing steel equal to €5/kg;

- $\text{\euro}_T$ is the price for using the printer for one hour (including labor) equal to €350/h;

- $\text{\euro}_J$ is the price per joint equal to €2000/joint;

The cost-values are determined together with 3DCP consultants of Witteveen+Bos. Note that the price for prestressing is including anchoring and installation. In practice, the total construction cost will be higher since in eq. (3.11) the material costs are considered only. It is assumed that this simplification is sufficiently adequate for comparing different 3DCP designs with each other.

3.3.3. Environmental impact indicator

The second criterion $f_2(\mathbf{x})$ is related to the environmental impact of the structure. A widely adopted method for quantifying the environmental impact of structures is conducting a Life Cycle Assessment (LCA). Using this method, the shadow price of a structure can be calculated, considering the entire life-span and all required materials and production processes. In this research, a LCA will be used to compare different 3DCP designs from an environmental point of view. The LCA performed in the context of this research is based on the assumptions listed below.

- Eleven life cycle impact categories are considered, these are: abiotic depletion, fuel and non-fuel (1), global warming potential (GWP) (2), ozone layer depletion (3), photochemical oxidation potential (4), acidification potential (5), eutrophication potential (6), human toxicity potential (7), freshwater- (8) and marine (9) aquatic ecotoxicity and terrestial ecotoxicity potential (10).

- Because it is expected that the raw material supply contributes most in the total shadow price and because in this analysis focus is on the design and material usage, only life cycle stage A1 is considered. This implies that the construction stage, use stage and end-of-life stage are assumed equivalent for each 3DCP bridge design alternative. The epoxy binder material is not considered in the raw material supply as it is assumed that the contribution is negligible given the relatively small volume.

1. production stage (half) products:

   – A1: raw material supply

   – A2: transportation

   – A3: manufacturing

2. construction stage of final product:

   – A4: transportation

   – A5: construction installation process

- In a number of researches on 3DCP material behaviour, the exact printable concrete mix composition has been mentioned. As reported in section 2.1.3, printable concrete mortars typically have a high cement content (i.e. low w/c-ratio) and consist of fine aggregates. Chen et al. [49] established an overview of published and non-published design mixtures from literature. These different concrete mixtures will be used to compare the environmental impact of a mix with a high OPC content, OPC in combination with pozzolans and fillers, a fibre reinforced mortar and a 100% geopolymer mortar. These results are combined with existing knowledge of the material properties as a function of the mix ingredients, based on which conclusions can be drawn with respect to the effectiveness of a high cement content. An overview of the different mixes is presented in table 3.1.

- The presence of admixtures is not considered, given their small amounts and because the shadow prices are hard to find because of the diverse compositions.

- The functional unit of this LCA is one m^3 of a prestressed bridge.

Table 3.1: 3D printable concrete mix compositions used for LCA, mix portions in [kg/m^3].

mix type	cement	slag	fly ash	silica fume	sand	water	other
OPC [50]	600	0	0	0	1379	259	-
OPC+pozzolans [17]	290	0	278	145	1211	285	-
geopolymer [17]	0	39	645	78	1168	47	alkaline activators [1]
fibre reinforced [17]	289	0	277	145	1209	284	glass fiber: 13.5

The Ecoinvent database [51] is used as the source for the required input in the LCA, being the monetary value of one kg of each specific mix ingredient for each impact category. The result is the shadow price [€] for each mixture per impact category. The complete calculation can be found in appendix B and the total shadow cost per [m3] per mixture together with the prestressing steel is provided in table 3.2. Remarkably, the geopolymer mixture has a higher environmental impact than the OPC-based mixtures. This is due to the high toxicity of the alkali-based activators. The GWP potential of the geopolymer mixture is lower than for the cement-based mixtures. The mixture with 50% replacement of OPC by alternative binders has a 50% lower shadow price, emphasizing the high environmental impact of OPC. For all mixtures, the GWP is the most important impact category.

Table 3.2: Total shadow price per material.

material	shadow price
mix 1	€32,39/m^3
mix 2	€16,08/m^3
mix 3	€44,07/m^3
mix 4	€17,55/m^3
prestressing steel	€0,66/kg

---

[1] actigel:8; bentonite:8; K2SIO3:250; KOH:23

Using these values, the total shadow price of a bridge design can be calculated with eq. (3.12).

$$f_2(\mathbf{x}) = \text{\texteuro}_C \cdot V_C + \text{\texteuro}_P \cdot M_P \tag{3.12}$$

in which

- V_C is the total concrete volume [m^3];

- $\text{\texteuro}_c$ is the shadow price per m^3 concrete;

- M_P is the required amount of prestress [kg] and

- $\text{\texteuro}_P$ is the shadow price per kg prestress.

3.4. Summary

The main construction principle of the 3DCP bridge designs analysed in this research is a sequence of 3DCP elements, connected using an epoxy joint material. The loads acting on the bridge are a combination of self-weight and variable traffic loading from cyclists and pedestrians. To be able to carry the tensile stresses induced by these loads, the structure is prestressed using post-tensioning of the tendons. The structure is finished with a concrete compression and a wear layer (see fig. 3.3, fig. 3.4 and fig. 3.6).

The safety of the bridge must be validated by performing a number of design checks. In SLS, it must be verified if the tendon eccentricity does not induce high tensile stresses at support-level and if the imposed deformations do not induce cracking. Furthermore, the deflection and eigenfrequency must be validated. In ULS, the structure's shear strength and bending resistance must be validated. Regarding the bending strength and required amount of prestress, two different scenarios are distinguished.

(A) If the joint strength is higher than the concrete tensile strength, the amount of prestress P can be designed based on (1) requiring a compression-only structure in SLS or (2) limiting the tensile strength in ULS to f_{ctd}. Hereafter called 'SLS_0' and 'ULS_{fctd}', respectively. These requirements holds at both support-level and at mid-span.

(B) If the joint strength is assumed to be zero, the concrete is not able to deliver any tensile resistance since a kinematic mechanisms has been established. Therefore, the amount of prestress must be based on requiring a compression-only structure in SLS, SLS_0. This requirement holds at both support-level and at mid-span.

In order to compare the performance of different bridge designs, two indicators have been defined; one for assessing the cost effectiveness of a design and one for assessing the environmental impact.

In the next chapter, the lay-out parametric model will be elaborated on. To construct the model, knowledge from this chapter as well as the previous chapter will be used.

4

Research model

4.1. Introduction

4.1.1. Model requirements

The main function of the model is to generate a 3DCP bridge design for a set of design parameters, whose values can be specified by the user. The model is used in chapter 5 and chapter 6 as a tool to generate design alternatives. This database of designs can be used to gain insight in the underlying relationships between input parameters and design and to optimise the design. The most important characteristic of the model is that it couples the design features corresponding to the fresh state with the structural design of the final, assembled structure.

In chapter 2, a thorough literature study has been conducted to understand the fresh material behaviour of 3D printable concretes and challenges regarding the printing process have been discussed. In chapter 3, the newly proposed box-girder design has been introduced, followed by a summary of the design requirements for this structure, derived from guidelines defined in Eurocode. The chapter was concluded with the definition of two performance indicators that allow for comparing design alternatives. The findings of these chapters are visualised as a comprehensive overview of all parameters incorporated in designing a 3DCP bridge structure, given in appendix A. The research model should be capable of capturing all the aspects discussed in the previous chapters to generate a 3DCP box-girder bridge design reflecting both printing process- and design aspects. Therefore, the following set of model requirements is defined.

- In section 2.2.2 and section 2.3.1, the mechanical properties of a few materials have been listed. It should be possible for a user to input a specific material type, as well as the input of separate material properties in order to analyse the effect of a single material property.

- In chapter 2, a number of geometrical (future) possibilities and limitations imposed by the printer have been discussed. These should be incorporated in the model to adequately reflect the printing process in the design.

- Next to the box-girder design, is should be possible to generate a design with the bottle-shaped cross-section as well in order to compare the two cross-section design alternatives. To give the user of the model as much freedom as possible, it should be possible to describe the cross-section in a fully parametric fashion.

- The user should be able to assess a design based on the design checks and performance indicators defined in chapter 3, which means these quantities must be outputted.

- Finally, it is desired to obtain a visualization of the design to more conveniently interpret the results.

4.1.2. Model framework

Based on this set of requirements, the basic model framework can be defined. The model is fed with a set of material, geometry and printing process parameters based on which it outputs a 3DCP bridge design. This design is visualised and described with the set of validation checks and performance indicators.

For a given design, the performance indicators can be calculated directly using the equations defined in section 3.3. However, to calculate the required amount of prestress, printability of the elements and the design validation checks, a structural analysis must be performed. These calculations must be both accurate and computationally efficient. Accurate because the design should be safe, but not over-conservative. Computationally efficient because the model is used to generate a large set of design alternatives. If for example 5 parameters are selected as variable and each variable can have 10 different values, then $10^5 = 100000$ different combinations exist and for each possible parameter combination an output set must be generated. The next sections further elaborate on the implementation of the structural analysis in the model, distinguishing between the fresh concrete elements and the final, hardened structure. A schematic representation of the model framework is given in fig. 4.1.
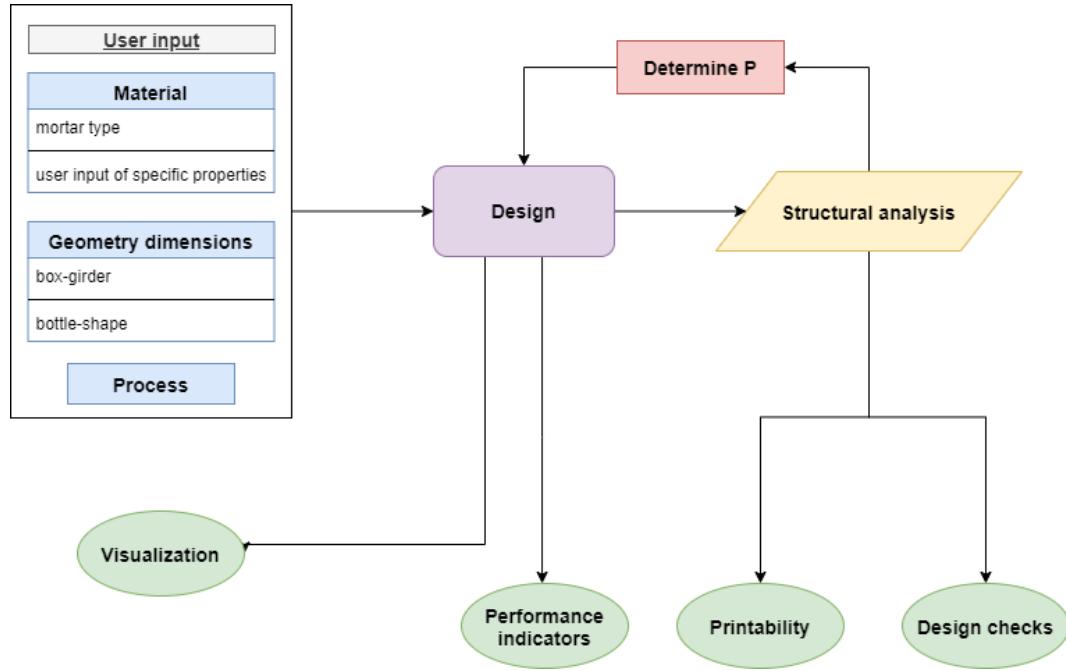
Figure 4.1: Schematic representation of the model framework. The blue blocks are input parameter sets, the green blocks represent output quantities.

4.2. Structural analysis of fresh concrete elements

4.2.1. Model assumptions

As described in section 2.2.3, a fresh concrete structure can fail by elastic buckling or by plastic collapse when reaching a critical element height. For both failure modes, an analytical model exists for predicting the maximum possible height. However, for more complex structures it is advised to use a numerical model for predicting the structural behaviour. Although the box-girder is more advanced than the validated structures in [2], in the parametric research model the structural performance will be approximated using the analytical prediction models in order to save computation time.

To do so, first an important assumption is made: for determining the maximum printable height, it is assumed that the layer has the same shape as the nozzle i.e. dxb. This implies that the material is very stiff and that no shearing prior to deposition occurs. In any other case, the actual layer width should be interpreted as independent of the nozzle size. Modelling the deformation of the layer after extrusion is a complex mechanism dependent on the material rheology, pump pressure and nozzle geometry, which can (today) be modelled only using numerical flow dynamics simulations and is therefore omitted in this research.

4.2.2. Implementation of analytical model approach

The calculation of the maximum height before plastic collapse occurs is relatively straight-forward. Assuming a pressure-dependent shear failure, the maximum height can be calculated using eq. (2.9). The terms representing the shear strength can be derived from eq. (2.4). The normal pressure $\sigma_n(t)$ is equal to the self-weight

at time t. Combining these two equations yields:

$$l_p = C_0 / \left[\frac{\rho_f g}{\sqrt{3}} - \frac{\alpha_C + \rho_f g \dot{l} \tan(\phi)}{\dot{l}} \right] \tag{4.1}$$

where C_0 and α_c refer to the initial cohesion and increase of cohesion in time: $C(t) = C_0 + \alpha_C t$.

The calculation of the critical height before elastic buckling is more complicated. Solving the differential equation in [2] to compute the critical height for a simply-supported and fully clamped wall can only be done in a purely numerical fashion or by reading the design graphs fig. 2.9. The closed-form approximation for the free wall in eq. (2.6) will yield a more conservative lower-bound solution. This analytical equation will be used in combination with the design graphs to approximate the critical height as described hereafter.

- The box-girder is split-up into smaller segments such that multiple equivalent rectangular boxes are considered. The critical wall with length s will be the longest side of a single box, being either the width of height, indicated by the grey shades in fig. 4.2:

$$s = \max[(H - b); (W - b)/n] \tag{4.2}$$

- Because the printing paths are long (>2 min layer print time), it is assumed that the material cures according to the quadratically increasing function due to heating up of the system [27].

- Equations eq. (2.7f) and eq. (2.7d) yield the dimensional wall length $\bar{s}$ and the dimensionless curing rate $\bar{\zeta}_E^l$, respectively.

- It is assumed that this wall with length s is not supported by the adjacent walls. In reality, these walls will provide some rotational stiffness and therefore this is a probably a rather conservative assumption [25]. However, this assumption is convenient for modelling, since the analytical approximation from eq. (2.6) can be implemented directly which is not possible when using the design graphs. A preliminary analysis has shown that the difference in critical buckling height between the case when a free wall is assumed and when a simply-supported wall is assumed is only 10%. This difference is small because the dimensionless wall length $\bar{s}$ is relatively large for this structure, approaching the solution for the free wall (see fig. 2.9a).

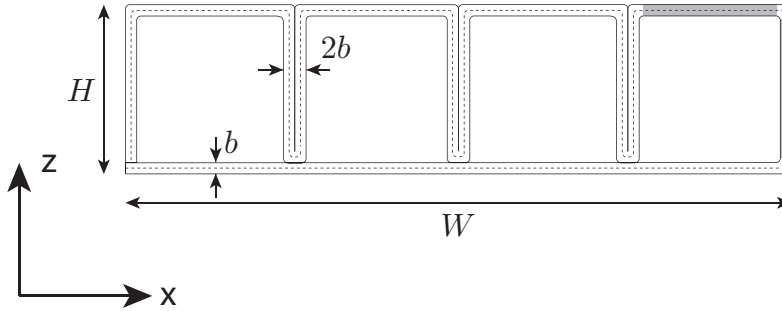- Finally, the actual buckling length can be calculated using eq. (2.7c).

Figure 4.2: Critical walls for buckling failure of the box-girder indicated in grey. Which wall is governing, depends on the adopted parameter values and its length can be determined using eq. (4.2)

Then, the maximum possible object height can be determined with:

$$l_{max} = \min(l_{cr}, l_p) \tag{4.3}$$

Comparing this maximum printable height to the actual object height yeidls the following printability requirement:

$$\frac{L}{N} \leq l_{max} \rightarrow UC_l = \frac{l_{max}}{L/N} \tag{4.4}$$

4.3. Structural analysis of hardened concrete structure

4.3.1. Model assumptions

Multiple strategies can be adopted to compute the design criteria for the final bridge structure defined in section 3.2.3. To limit computation time, it is desired to avoid the use of FE software if possible. This can be done by using analytical formulations based on Euler-Bernoulli beam theory to compute resulting stresses and strains, instead of more advanced numerical 2D or 3D models. This simplified approach is adopted in the research model. However, certain limitations concerning the applicability of the beam-theory should be taken into consideration:

- the beam-theory is applicable to slender structures only, i.e. having a minimum span/depth-ratio of 10-15. As the slenderness ratio decreases to 5, shear strains become increasingly important and therefore structures should be calculated using the Timoshenko beam formulation or, for slenderness ratios below 3, using a vertical plate;

- local stresses close to a point where point loads are applied are not captured;

- stresses other than normal stresses in the direction of the longitudinal beam axis cannot be captured;

- detailed stress patterns induced by torsional moments from eccentric loading cannot be modelled;

Unfortunately, due to these assumptions, a number of checks defined in section 3.2.3 cannot be performed when using the simplified beam-model. Therefore, to ensure that these checks are not governing and thus can be safely disregarded, a numerical validation procedure is conducted for limit cases using a more detailed FE model. Second, the applicability of the model for calculating normal- and shear stresses is verified in the same way. Because the detailed relations between the environmental parameters, geometry and material properties and the shrinkage and creep of 3D printable concrete structures are non-existent at this moment, the validation for cracking of the concrete structure due to the time-dependent deformations is omitted in this research. The loss in prestress will be accounted for by assuming a reduction of 20% which is conservative. The implementation of the beam model is discussed in section 4.3.2 and the validation procedure in section 4.3.3.

4.3.2. Implementation of beam-model

In this section, the approach for obtaining the required quantities for calculating the design checks using the beam model is explained briefly. Appendix C.1 provides a detailed description of the equations that are used to calculate the required output quantities.

1. The beam is split-up in a predefined number of elements with size dx. Then, for each of these elements the cross-sectional properties A, W_{top} and W_{bot}, I_y and the total print-path length S are calculated. This approach allows for considering a non-prismatic beam if desired. Note: it is assumed that the cross-sectional resistance is delivered by the 3DCP beam only - the contribution of the top-layer is neglected. The cross-sectional properties for the box-girder can be calculated by hand in a straight-forward manner, which saves computation time. The bottle-shaped cross-section is more complex and is therefore calculated using Grasshopper (more on this in section 4.4).

2. The loads and the following load combinations are defined:

   - SLS: self-weight only + P (load-combination during construction)

   - SLS: characteristic load combination (3.4)

   - SLS: frequent load combination (3.5)

   - ULS: full load (3.3)

3. The tensile stresses induced by these loads at mid-span and support-level can now be calculated. The minimal required amount of working prestress $P_{m\infty}$ is computed. Then, it is verified if the tensile stress requirement at support-level during construction is fulfilled. If not, the tendon eccentricity e_p is reduced (and P is thereby increased) in an iterative loop, until this requirement is satisfied.

4. Using this value for $P_{m\infty}$, for each beam-element the resulting normal stresses at top and bottom are stored, together with the bending moment capacity and the prestressing stress increase for scenario (B).

5. The deflection w at mid-span is calculated.

6. The compressive, tensile and shear resistances are calculated, considering a reduced tensile strength due to a loss of bond-strength. This reduction is calculated for three scenarios: no, a moderate or high reduction. Considering these different scenarios allows for studying the effect that the layer interval time ti has on the structural performance. The moderate and high reduction scenarios are derived from fig. 2.11a and fig. 2.11b. The points in both graphs are read and plotted in Excel, after which a trendline could be derived (see fig. 4.3). The resulting relations are:

   6.1. No loss in bond-strength;

   6.2. Moderate loss in bond-strength according to [28] depicted in fig. 2.11a, equal to:

$$f_{ctd}(ti) = -0.151 \cdot \ln(ti) + 0.9811 \tag{4.5}$$

   6.3. High loss in bond-strength according to [30] depicted in fig. 2.11b, equal to:

$$f_{ctd}(ti) = 0.8642 \cdot ti^{-0.45} \tag{4.6}$$

7. Finally, the following validation checks can be calculated:

Table 4.1: Design validation checks calculated using the beam model. A check is OK if the UC-value is smaller than 1.0.

description	limit state	check
prestress limit to prevent concrete crushing	SLS	$UC_{0.6f_{ck}}$
dynamic verification	SLS	UC_{ω}
deformation limit	SLS	UC_w
shear force limit	ULS	UC_V
scenario (A): concrete tensile stress limit	ULS	$UC_{f_{ctd}}$
scenario (A): concrete compression stress limit	ULS	$UC_{f_{cd}}$
scenario (B): bending moment capacity	ULS	UC_M
scenario (B): prestress limit	ULS	UC_P
scenario (B): concrete compression stress limit	ULS	$UC_{f_{cd}}$
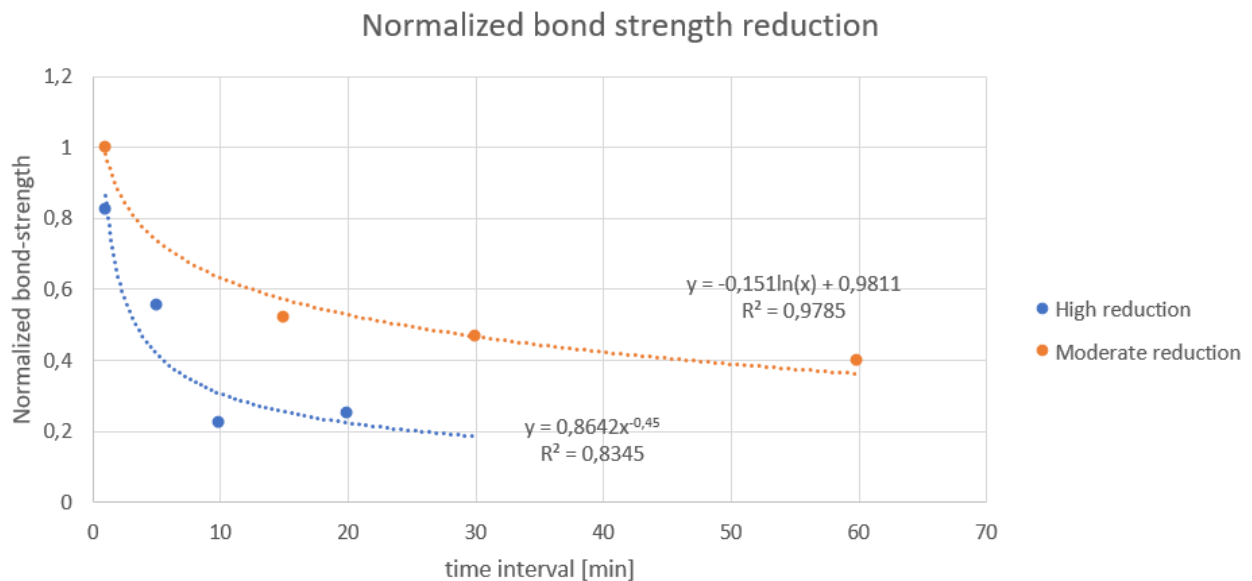
Figure 4.3: Moderate and high bond strength reduction functions for increasing time interval between layers.

To conclude, this approach allows for calculating most of the design validation criteria. When choosing an adequate element size dx, the calculation time is small because no FE software is required. In the next section, the accuracy and applicability of the simplified model is determined by validating it using a FE model.

4.3.3. Validation of simplified model approach

To verify if the assumptions made by using the simplified beam model are safe, a FE validation model of the bridge is established. It is decided to use a 3D-model since only a small number of parameter sets need to be validated and in this way a detailed outline of the stress-patterns can be obtained. The software DianaFEA is chosen because a model can be built using a Python script which is convenient for defining the model parametrically. For details about how the FE model and the analyses that have been performed, reference is made to appendix D.

The design cases specified in table 4.2 will be assessed for validating the applicability of the 1D-model.

Table 4.2: Case studies for validating the applicability of the simplified beam model.

validation case	W [m]	L [m]	H [m]	b [m]	n	traffic load case	assumption to verify
case 1	5	15	1.5	0.05	8	q_{fk}	maximum slenderness
case 2	5	20	1.5	0.05	3	q_{fk}	large span
case 3	5	15	1.0	0.05	3	q_{fk}	transverse stresses
case 4	5	10	1.0	0.05	3	Q_{serv}	local+global loads from service vehicle

The validation results are summarized in table 4.3. It can be concluded that the beam-model simplification safely approximates the bridge behaviour and does not neglect important design checks.

Table 4.3: Summary of validation results per case.

case	results	conclusion
1	stresses < f_{ctd} and linear stress distribution	EB hypothesis valid
2	stresses < f_{ctd} and similar to 1D-model	1D model applicable for large spans
3	no peak stresses in transverse direction	safe to not consider
4	stresses < f_{ctd}	service vehicle not governing

4.4. Model lay-out

From the results of the previous sections, it can be concluded that the simplified structural analysis approach is a safe and sufficiently accurate representation of reality. The structural performance of the fresh state can be predicted using analytical functions yielding a conservative lower-bound solution. For calculating the equations embedded in the model, the input parameters listed in table 4.4 are required. Note that, instead of providing separate material properties, the model also contains a library with the material properties of the Weber 3D 115-1, Weber 3D 145-1, Weber 3D 145-2 and Weber 3D 160 mixture (see table 2.1 and table 2.2 for the corresponding values). The geometry parameters can be defined assuming a box-girder or a bottle-shaped topology, chosen by the user.

Because of the parametric nature of the model, it is decided to use Grasshopper+Rhino as the main programming environment, extended with custom-made Python scripts. Grasshopper is a visual scripting language with which Rhino geometry can be built and controlled. This is done using blocks that can be placed on a canvas and connected with each other, creating a data flow. In the research model, a python-script is written containing the analytical formulations for calculating the required output quantities. This script is called in Grasshopper and fed with the required input parameters defined on the canvas. Using this structure, the geometry can be visualized and analysed simultaneously. Another benefit is that the python script can be used outside of Grasshopper as well for performing the parameter studies and optimisation performed in the next chapters. In addition, a User Interface shown in fig. 4.5 is developed such that the model can be used without the need for understanding Grasshopper.

Table 4.4: Overview of model input parameters.

category	parameter	symbol	reference
print process	horizontal print speed	v [m/s]	fig. 2.2
print process	layer height	d [m]	fig. 2.2
print process	layer width	b [m]	fig. 2.2
material, fresh	cohesion at t=0	C_0 [Pa]	table 2.1
material, fresh	linear cohesion increase in time	α_C [Pa/s]	table 2.1
material, fresh	angle of internal friction	ϕ [°]	table 2.1
material, fresh	Young's Modulus at t=0	E_0 [Pa]	table 2.1
material, fresh	linear Young's Modulus increase in time	α_E [Pa/s]	table 2.1
material, fresh	compressive strength at t=0	σ_0 [Pa]	table 2.1
material, fresh	linear compressive strength increase in time	α_σ [Pa/s]	table 2.1
material, fresh	density of fresh concrete	ρ_f [kg/m^3]	table 2.1
material, hardened	density of hardened concrete	ρ [kg/m^3]	table 2.2
material, hardened	compressive strength	f_{ck} [MPa]	table 2.2
material, hardened	tensile strength	f_{ctk} [MPa]	table 2.2
material, hardened	Young's modulus	E [MPa]	table 2.2
material	Poisson's ratio	v [-]	table 2.1
geometry	width	W [m]	fig 3.4
geometry	span	L [m]	fig 3.4
geometry	height	H [m]	fig 3.4
geometry	number of cells in cross-section	n [-]	fig 3.4
geometry	height reduction at mid-span	a [m]	fig. 3.4
geometry	total number of elements	N [-]	fig 3.4
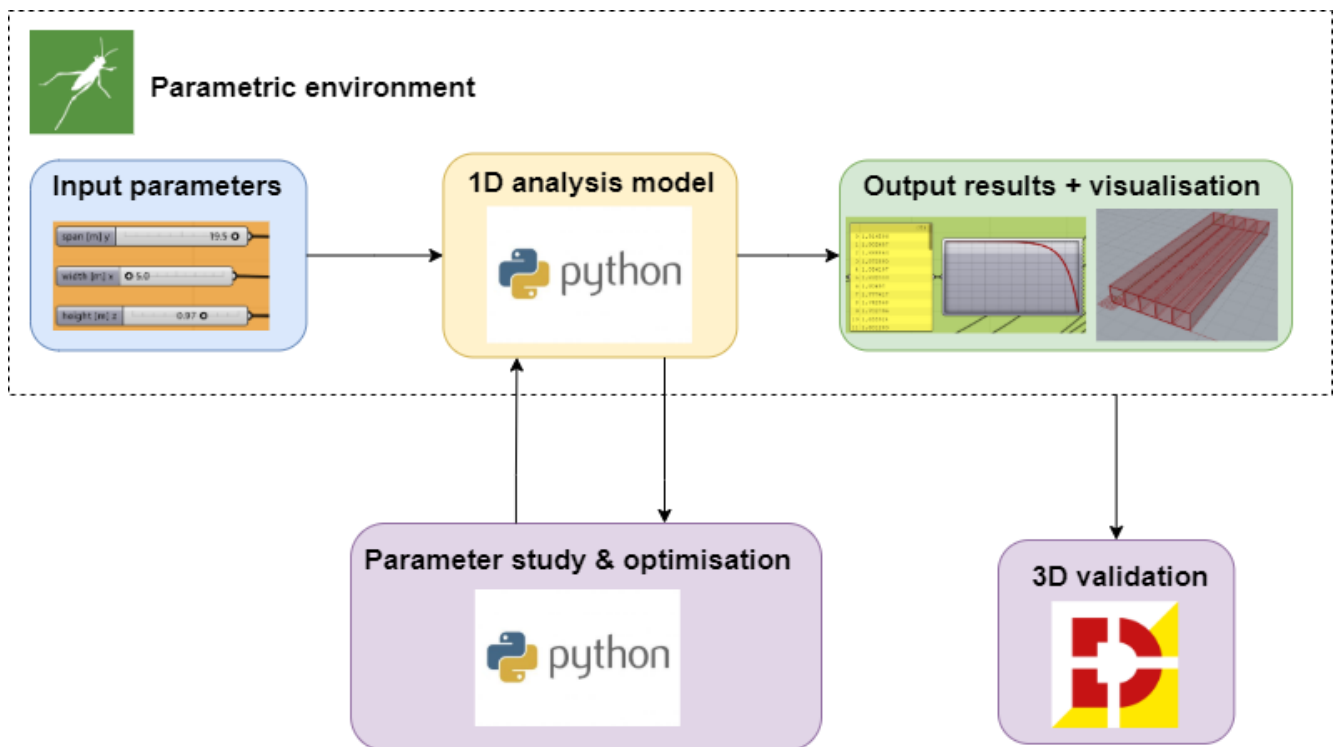
Figure 4.4: Schematic representation of the model lay-out, combining Grasshopper, Python and DianaFEA.
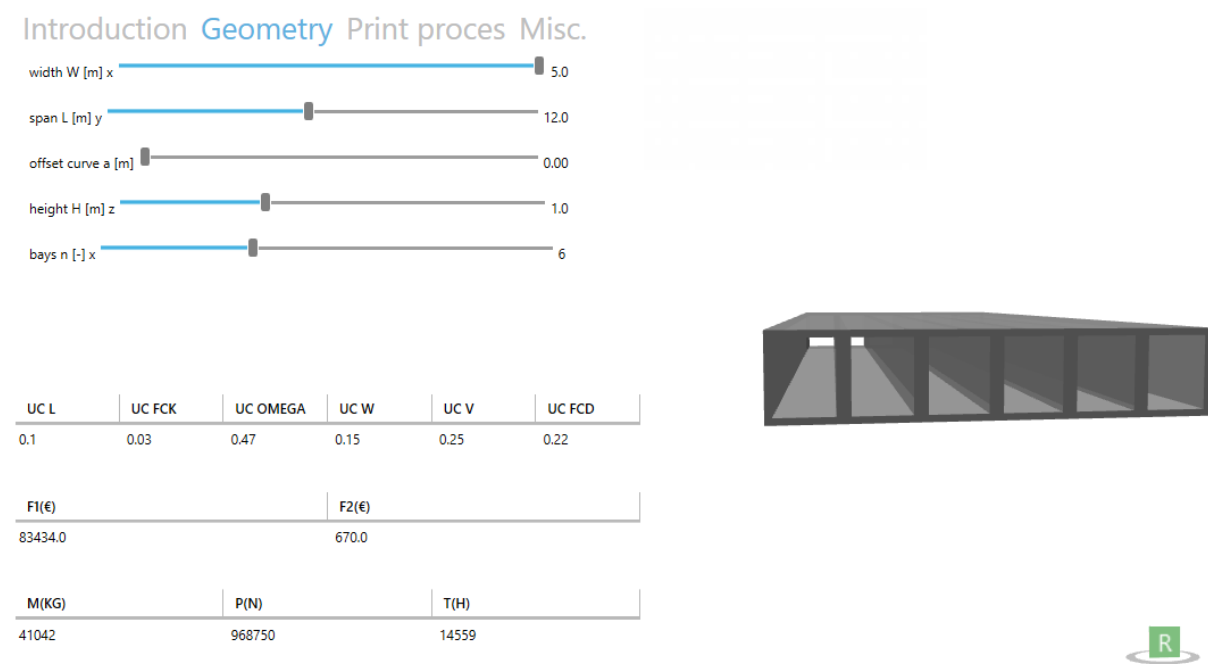
Figure 4.5: User Interface in which bridge designs can be generated.

4.5. Conclusion

A parametric research- and design model has been developed which generates 3DCP bridge designs as a function of material, geometry and printing process parameters. The design model is built using analytical relations only which is computationally efficient since the use of FE software is not required. This analytical approach is sufficiently accurate and a safe approximation of reality. Using Grasshopper+Rhino in combination with Python as the programming environment, the design can be visualised. The feasibility and performance of a design can be assessed by the user by interpreting the outputted values for the design validation checks and performance indicators. In the next chapters, the parametric research model will be used for conducting a parameter study and to optimise the design of a 3DCP bridge.

5

Parameter study

5.1. Objective & method

In this chapter a number of analyses is performed to gain insight in the underlying relations between design variables and the performance and feasibility of the bridge design. After a short introduction of each analysis, the adopted methods are discussed. In the following sections, the context and results of each analysis are discussed in detail.

1. A **preliminary** qualitative **study** is performed to to observe the characteristics of the model responses and to check the model for errors, by detecting possible unexpected relations and discontinuities in output functions.

2. Analyse the *relative* **importance** of each **parameter** on the performance and feasibility of the bridge design. The results provide insight in which parameters are most important when designing a 3DCP structure. This information can be used to simplify the design process by fixing non-sensitive design variables.

3. Investigate the effect of a reduced interlayer **bond-strength** on the design, a frequently reported issue of 3DCP sample measurements. This is done by comparing the resulting designs for varying strength degradation functions.

4. The current **low robustness** of the printing process is a common known issue, yielding uncertainties in the properties and quality of a 3DCP element. In this analysis, the source of the spread is allocated, based on material properties measurement data of 3DCP samples. Secondly, the effect of an uncertainty in the measured mechanical properties on the structural design is assessed.

The parameter studies are performed by conducting sensitivity and uncertainty analyses using the parametric model. A sensitivity analysis (SA) studies how uncertainty in the output of a model can be allocated to different sources of uncertainty in the input of a model [52]. SA is different from uncertainty analysis, which is used to describe the range of possible outcomes for a set of input parameters with given uncertainty. It does not address the contribution of a single parameter to the total uncertainty of model outcomes.

Two types of SA can be distinguished: local and global. Local SA studies the effect of varying a single parameter at a time on the variation in the output. Global SA methods study the output variability when manipulating two or more variables at a time, thereby revealing parameter interactions. Global methods are able to deal with non-linear models, but require a higher computational cost. When studying local sensitivities only, there is a risk of underestimating a parameter effect. In the SA conducted in this research, both local and global sensitivity methods are used. The methods that are used to conduct these analyses are described hereafter.

Local sensitivity analysis

The local sensitivity can be assessed qualitatively by plotting the output quantity of interest against one input parameter. From this graph it can be derived if the relation is linear, (monotonically) increasing or decreasing. If the relation is linear, a qualitative measure of sensitivity can be derived equal to the gradient of the trend. In case of a non-linear or even non-monotonic trendline, a local gradient can be derived only.

Global sensitivity analysis

The Sobol' method is a variance-based SA method [53] which can handle non-linear and non-monotonic response functions. A variance based method quantifies the amount of variance that each parameter contributes to the unconditional variance of the output. These amounts can be related to a single parameter or to the interaction between two parameters. The contributions are expressed as sensitivity indices (SI's), representing the fractions of the model output variance which are a direct measure of sensitivity. Both first- and second order indices are computed: first order SI's indicate the local sensitivity of an individual parameter and second order SI's indicate the interaction between two parameters, which highlights processes that are closely related.

Consider a parameter X_i and its partial variance V_i. The first order sensitivity index $S_i = V_i/V$ or 'main effect' represents the contribution of this parameter's variance to the total variance. In other words: on average, the model output variance would decrease with V_i if X_i would be fixed. The impact of the interaction between two parameters X_i and X_j is given by $S_{ij} = V_{ij}/V$ and the total contribution of a parameter including main effect and interactions is S_{Ti}. If the model is additive, $S_{Ti} = S_i$ and the sum of all S_i's is equal to 1. For non-additive models interactions exist and the sum of all S_i's is smaller than 1, while the sum of all S_{Ti}'s is larger than 1. The Sobol indices are computed using the SALib package for Python [54], which requires the following input arguments:

- The total number of variables and the range in which each parameter may vary.

- The number of input samples N e.g. parameter combinations that is drawn. A higher number of samples increases the significance of the computed indices, but also increases computation time. To calculate the minimum required number of samples, a convergence study must be performed. The significance of the Sobol indices can be determined by interpreting the confidence interval of each index, which is returned by the algorithm. The SI's are significant if the confidence interval is within 10% of the SI-value.

- The desired confidence level of the Sobol indices, by default set to 95% which is adopted in all analyses.

Finally, it should be noted that this method assumes that the input parameters are independent of each other.

Uncertainty analysis

The uncertainty analyses are performed using the Monte Carlo method. The uncertainty of an input parameter must be known by fitting a certain distribution to it. Then, a random sample within that distribution is drawn N times and for each sample the model output is interest is calculated, yielding N output results. Plotting the distribution of these outputs yields insight in the degree to which the input uncertainty affects the model output.

5.2. Preliminary study

5.2.1. Introduction

First, the model is analysed qualitatively in order to detect unexpected relations and discontinuities and to characterize the behaviour of the model response. This is done by means of a local sensitivity analysis, in which the response of each output quantity is plotted against each input parameter. Because it is not expected that the value of the individual material properties will introduce model errors, these will be fixed corresponding to the Weber 3D-160 mixture and assuming a moderate bond-strength reduction (i.e. according to fig. 2.11a). The other parameters are varied one by one within a predefined range and when varying each parameter, the others are fixed. The lower- and upper bounds and fixed values of the variable input parameters are listed in table 5.1.

Table 5.1: Lower- and upper bound and fixed parameter values adopted during the preliminary study.

parameter	lower bound	upper bound	fixed
W [m]	3	5	4.5
L [m]	10	20	12
a [m]	0	0.4	0
H [m]	0.5	1.5	0.8
n [-]	3	8	5
b [m]	0.03	0.1	0.05
d [m]	0.009	0.02	0.01
v [m/s]	0.080	0.180	0.120
N [-]	10	30	20

The output quantities of interest are the design validation checks in both fresh and hardened state and the two performance indicators. Distinction is made between the two joint-strength scenarios (A) in which the joints are stronger than the concrete in tension or (B) in which the joints have no tensile strength. For scenario (A) the output quantities are plotted for designing the prestress (1) requiring compression-only in SLS (marked as SLS_0) and (2) requiring a limited tensile strength in ULS (marked as $ULS_{f_{ctd}}$). For scenario (B) only SLS_0 is considered, since the concrete tensile strength cannot contribute to the bending resistance.

5.2.2. Results
In appendix E.1, the analysis results are presented as a set of graphs for each parameter, distinguishing between scenario (A) and (B). The characteristics of each response are summarised in table E.1 and E.2. Upon globally analysing the resulting graphs and model characteristics, the following is observed.

- For both scenarios, the model response can generally be characterised as non-linear, since a large number of output quantities depend on the design variables in a non-linear fashion. Moreover, the UC for deformations UC_w is non-monotonic for an increasing height reduction at mid-span a and f_2 is non-monotonic for increasing H, as these quantities first increase and later on decrease. The apparent complexity of the underlying model emphasizes the need for this parametric design approach, as it is hard to determine optimal solutions using an iterative design process.

- When requiring the prestress to be designed such that a compression-only structure is obtained in SLS (SLS_0), the response is non-continuous for many output quantities, showing a step-wise behaviour. This can be explained as follows: starting point for determining the amount of prestress is assuming the practically maximum possible tendon eccentricity. However, this might induce tension at support level from tendon eccentricity. This is not allowed and therefore, the model will decrease the tendon-eccentricity step-wise, thereby increasing the amount of prestress.

- The layer height d and number of elements N are not influential for most output quantities and only influence the fresh concrete structural performance UC_l and the cost performance indicator f_1. This can be expected, as these parameters do not influence the cross-sectional resistance or loading and thus do not affect the design validation checks. Moreover, experiments have not yet shown a clear dependence between the mechanical strength and the layer-height. For scenario (B) however, a kinematic mechanism is created assuming two rigid blocks rotating about a point at mid-span, which is in reality only true for an even number of elements - for an odd number of elements two joints will open just left and right from the middle-element yielding a different mechanism. However, this is not considered in the model and therefore the parameter N is not affecting in the corresponding design checks.

- The structural performance of the fresh concrete structure does not change when introducing a non-prismatic beam via the parameter a. This means that cantilevering layers must be printed, which cannot be described using the model of [2]. It is, however, a non-conservative relation, since overlapping layers generally decrease the stability of the structure. This must be kept in mind when analysing the potential benefit of introducing a non-prismatic beam.

Secondly, the difference between the results from the two prestress design requirements SLS_0 and $ULS_{f_{ctd}}$ in scenario (A) is analysed, yielding the following observations.

- The relations for both requirements generally have the same monotonic behaviour (i.e. are both increasing or decreasing). However, some relations show an opposed trend:

  - The required amount of prestress assuming SLS_0 decreases for increasing a but decreases when assuming $ULS_{f_{ctd}}$. Increasing a means an increasing tendon eccentricity but decreasing cross-sectional resistance. Apparently, for $ULS_{f_{ctd}}$, this increasing tendon-eccentricity cannot keep up with the decreasing cross-sectional resistance (although the increase is small). Consequently, $UC_{f_{ck}}$ which is linearly related to the required amount of prestress shows similar behaviour and UC_V and UC_M which are linear inversely related to P show opposite behaviour.

  - For increasing b, the required amount of prestress assuming SLS_0 increases while it decreases assuming $ULS_{f_{ctd}}$. When the layer-width increases, both the cross-sectional area and self-weight increase. When assuming $ULS_{f_{ctd}}$, the increase in cross-sectional area dominates the increasing load. This effect is only pronounced in UC_M for scenario (B), which decreases for increasing P.

- It is obvious that the value of $UC_{f_{ctd}}$ in scenario (A) is insensitive for varying parameter values, as the required amount of prestress is based on assuming this UC to be equal to 1.0.

- Initially, it was expected that the SLS_0 requirement would have been more conservative in general. However, for larger spans and when introducing the non-prismatic beam, the $ULS_{f_{ctd}}$ becomes more conservative. This can be explained as follows: when designing the prestress in SLS, the stresses cannot be controlled upon increasing the load towards ULS, whereas the ULS-requirement ensures the UC's are fulfilled at a higher load-level. Apparently, for larger spans, the loads in ULS are higher than the remaining load capacity when designing for compression-only in SLS.

The third set of observations is obtained upon comparing the responses for scenario (A) and (B).

- As expected, the results assuming scenario (A) and (B) are equal apart from the bending checks defined in ULS ((A) UC_{fctd} and $UC_{f_{cd}}$ and (B) UC_M, UC_P and $UC_{f_{cd}}$).

- For scenario (B), note that UC_P is only sensitive to a change in length and height. This makes sense, because the increase in prestress upon development of the mechanism is basically dependent on the ratio between span and height only.

Finally, a rough quantitative analysis is conducted, upon which the following is obtained.

- The values of the UC's are all between 0 and 2.0, meaning that the adopted parameter bounds are realistic. For this adopted parameter set, it can be generally concluded that the UC's in ULS are governing over the UC's in SLS.

- The UC for the verification of the dynamics becomes critical for long spans only. This can be expected, as the slenderness increases accordingly, becoming more sensitive to vibrations. The UC for the maximum amount of prestress $UC_{f_{ck}}$ is, for all parameters, far from critical.

- Generally, the UC-values for scenario (B) are higher than for scenario (A), implying that scenario (B) is more conservative, which is in line with expectations as the concrete is not contributing anymore to the tensile resistance. The bending moment capacity is critical and can only be increased by increasing the applied amount of prestress (which is generally possible, given the fact that UC_P and $UC_{f_{cd}}$ are less critical) or by increasing the internal lever arm i.e. the deck height.

5.2.3. Conclusion
Based on these observations, it can be concluded that the model does not show any inconsistencies, meaning that the relations derived from literature and design practice are likely to be implemented correctly. The response assuming SLS_0 shows step-wise behaviour due to the incremental decrease in tendon-eccentricity to decrease the tensile stress at support-level. Furthermore, the UC's in ULS are generally governing the design feasibility where mechanism (B) is more conservative than (A). In SLS, $UC_{f_{ck}}$ is not expected to be governing in any case given the low values and the dynamic verification check UC_ω is only required for large spans. The SLS_0 prestressing assumption requiring compression-only in SLS is more conservative for lower spans, but for larger spans the $ULS_{f_{ctk}}$ prestress requirement which limits the tensile strength in ULS is more conservative.

5.3. Relative parameter importance

5.3.1. Introduction

A global sensitivity analysis using the Sobol method is performed to determine the relative parameter importance for the feasibility and performance criteria of a 3DCP bridge design. The Sobol method calculates the relative contribution of each parameter's variance to the total variance of each output. This allows for ranking the parameters from most influential to least influential.

In this analysis, all parameters are varied within predefined ranges. A preliminary trial analysis has shown that the results are dependent on the ranges that were used as input. This effect is caused by the interaction between parameters. Therefore, three different parameter range scenarios will be analysed. The first scenario reflects the design space for a smaller span bridge (LB), the second scenario for a larger span bridge (UB) and the third scenario considers the total design space (tot). The trial analysis showed a predominant interaction between L and H and therefore the corresponding H-ranges are estimated using $H = L/15$. The number of elements N for each range is determined assuming each element is 1m long. The effect of a prismatic cross-section will be analysed in chapter 6 and therefore $a = 0$ in this analysis. An overview of the scenarios with corresponding ranges for the geometry- and process parameters is given in table 5.2a (the other parameter ranges are constant throughout the three scenarios).

The material parameters are varied individually, rather than varying the discrete mixture type. It should be noted that this might yield unrealistic results, since the Sobol method assumes independent parameters. It is possible to implement parameter dependence by sampling the parameters for a given correlation matrix. However, this is not done here, as this is a time-consuming procedure and a large dataset is required for determining the correlations. Not considering this dependency underestimates the importance of the material parameters, but since the correlations are unknown it is impossible to say to which extent. The adopted material parameter ranges are derived from the material properties reported in table 2.1 and table 2.2 and can be found in table 5.2b. Note that the parameter deg denotes the degree of bond-strength reduction between two layers for increasing velocity, which can take values 0, 1 or 2 corresponding to no, a moderate or high reduction, respectively. For calculating the second objective function, the shadow price of 'mix 1' containing a high cement portion is used, equal to €32,39/m³. In total 21 variables are incorporated. The minimal required number of parameter samples for giving significant results is set to $N = 30000$, determined in the preliminary trial analysis.

Table 5.2: Parameter input ranges for the relative importance SA.

(b) Material parameter input ranges.

(a) Geometry and process parameter input ranges, assuming three different design scenarios ($a = 0$). See fig. 3.4 for the parameter definitions.

parameter	LB range	UB range	total range
W [m]	3.5-5	3.5-5	3.5-5
L [m]	8-14	14-20	8-20
H [m]	0.53-0.93	0.93-1.33	0.53-1.33
n [-]	3-8	3-8	3-8
b [m]	0.03-0.1	0.03-0.1	0.03-0.1
d [m]	0.009-0.02	0.009-0.02	0.009-0.02
v [m/s]	0.080-0.180	0.080-0.180	0.080-0.180
N [-]	8-14	14-20	8-20

parameter	range
ρ_f [kg/m³]	2070-2175
E_0 [Pa]	17369-77912
α_E [Pa/s]	20.45-57.05
σ_0 [Pa]	1109-5984
α_σ [Pa/s]	2.45-5.23
C_0 [Pa]	2600-3050
α_C [Pa/s]	0.97-1.04
ϕ [°]	0-20
f_{ck} [MPa]	21-30
f_{ctk} [MPa]	1.3-4.86
ρ [kg/m³]	2000-2120
E [MPa]	19000-30000
deg [-]	0, 1 or 2

The amount of prestress in scenario (A) is designed for requiring a limited tensile stress equal to the concrete tensile strength in ULS, because the previous study has shown that this is a more conservative approach for increasing span. The analysis is conducted for scenario (A) only, as the purpose of this analysis is to investigate the influence of the concrete material properties relative to the geometry and process parameters. The relative parameter importance is calculated for all design validation criteria except for UC_{fctd} as this check is designed to be equal to 1.0 and thereby not of interest, and for the two performance indicators. Additionally, the required amount of prestress is analysed in order to interpret the results more conveniently.

5.3.2. Results

After running the analyses, a visual overview of the *total* sensitivity index values (so, the SI's including interaction effects) is obtained for all output quantities per variable range set. The relative importance results and possible parameter interactions are discussed hereafter, distinguishing between the UC's and the PI's.

Design feasibility: UC's

In fig. 5.2a, fig. 5.2b and fig. 5.2c, the relative parameter importance for the UC's assuming scenario (A) are plotted. The SI's for UC_V for the total scenario are not plotted as these did not reach convergence. The 1st order and total sensitivity indices for all other output quantities for the three adopted variables ranges were significant, given that the errors turn out to be within 10% of the actual index value. Each first bar in fig. 5.2 is the check for the performance of the fresh concrete structure UC_l, bars 2-4 are the SLS checks $UC_{f_{ck}}$, UC_ω and UC_w and bars 4 and 5 are the ULS checks UC_V and $UC_{f_{cd}}$. Upon comparison of the three graphs in fig. 5.2, the following is observed.

- The fresh concrete structural performance check UC_l is governed by the layer width b for all variable ranges. Since local buckling is likely to be the governing failure mechanism this can be expected, as the wall-thickness enhances the stiffness with a factor b^3. Note that the fresh material properties only have a minor influence on the fresh performance, compared to the geometry. It is expected that interaction effects other than between L&H are present, since the results between the three range scenarios differ. This is confirmed by the interaction diagram shown in fig. 5.1a. The parameters b, N and L interact, explaining the difference between the range scenarios. Therefore, the relative parameter importance is determined for the maximum printable height l, rather than the $UC_l = l/(L/N)$. The result is visualised in the pie-diagram shown in fig. 5.1b. From this graph it can be deduced that the layer width b is most influential for the maximum printable element height, while the fresh material properties are of minor importance. Note that this result is obtained under the assumption that the layer does not deform after extrusion. For more fluid materials, the fresh material properties are important, since the viscosity and static yield stress and the nozzle geometry determine the obtained layer width.
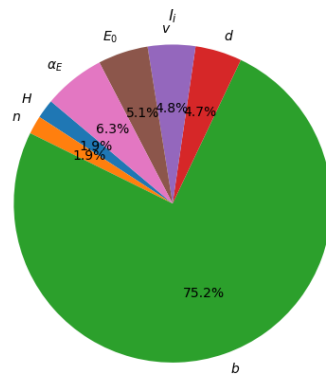
(a) Relative parameter importance for the maximum printable element height l, showing a large dependence on parameter b (in green).
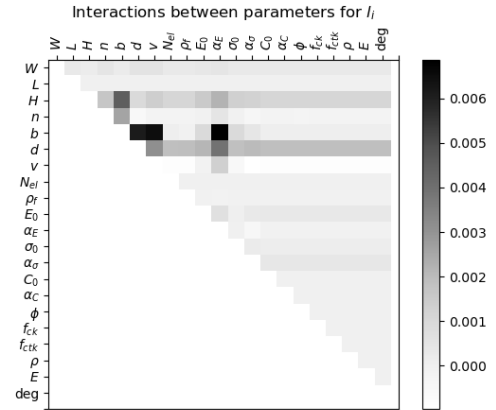
(b) Parameter interaction diagram for UC_l.

Figure 5.1: Global sensitivity analysis results for the maximum printable height l for the total variable range.

- The relative parameter importance results for the hardened UC's are similar for the three adopted variable ranges, meaning that no other parameter interactions affect the result.

- The SLS checks are all dominated by the span L, cross-sectional height H and layer width b, respectively. Small differences are present across the variable ranges, but the *order* of importance is unaffected. The strength and stiffness of the material turns out to be of minor importance compared to the geometry.

- The shear strength validation check is governed by the characteristic tensile strength f_{ctk}, followed by the total web width determined by n and b. These results can be expected given the assumed relation for the shear resistance from eq. (3.9).

- The UC for validating the compressive strength is clearly dominated by the span, followed by the height H and number of webs n. Minor differences exist between the adopted variable ranges, but the span is always dominating. Note that the concrete compressive strength only appears to be of minor influence.
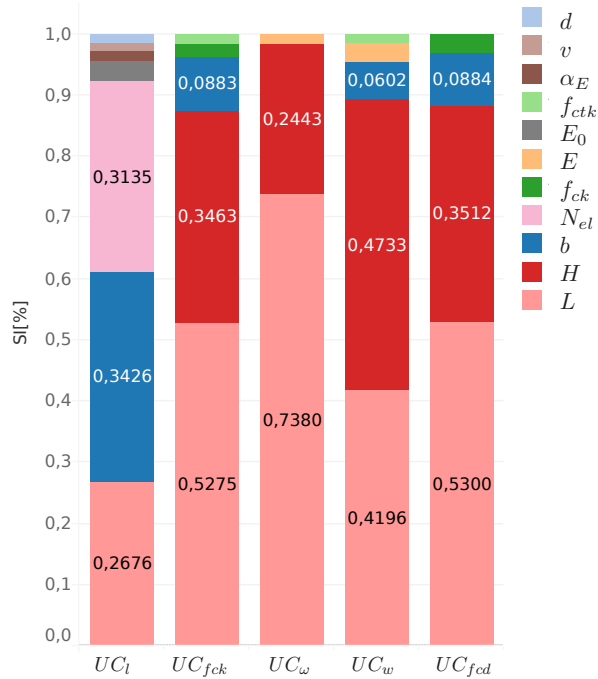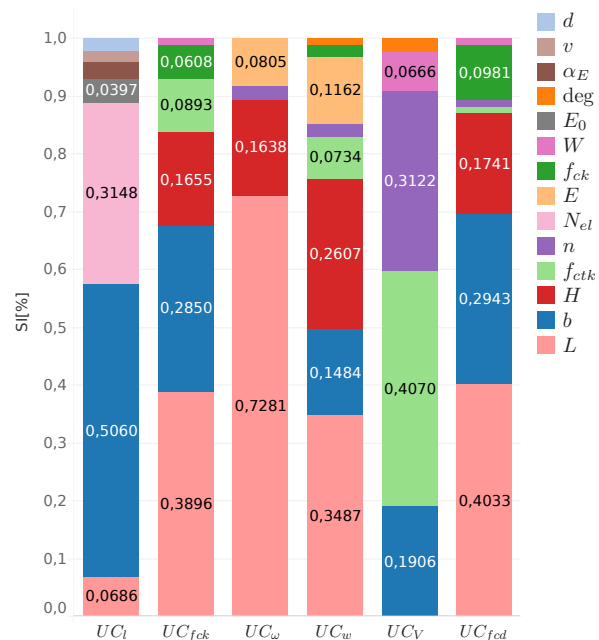

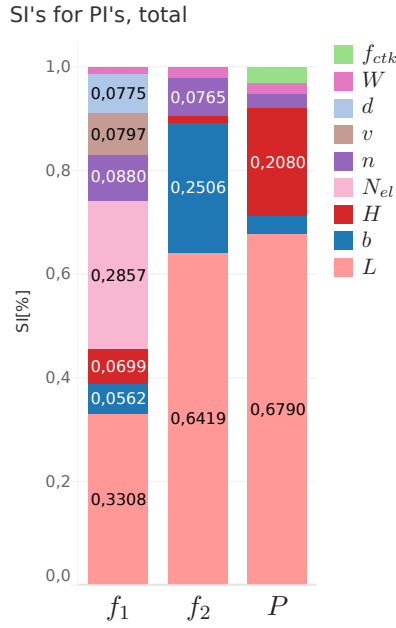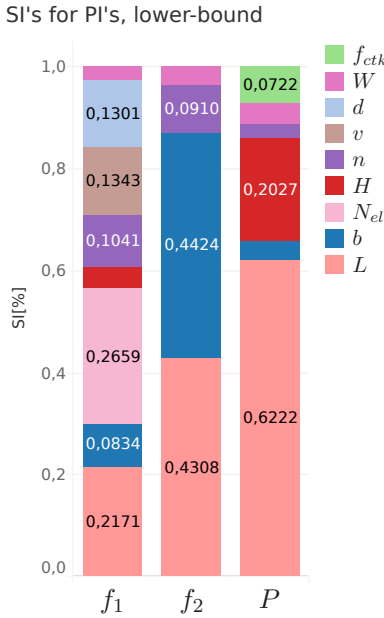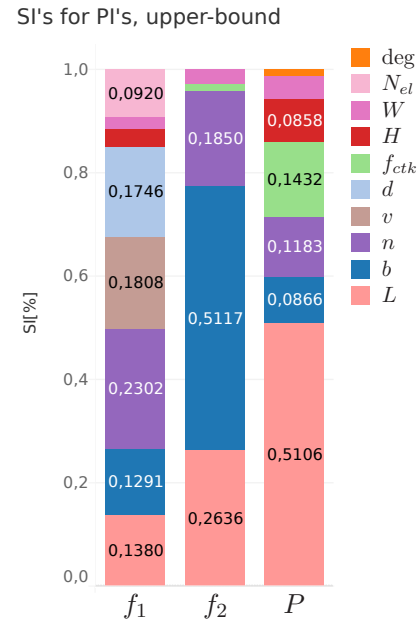(a) Relative parameter importance [%] for the 'total' variable range ($8 \leq L \leq 20$).
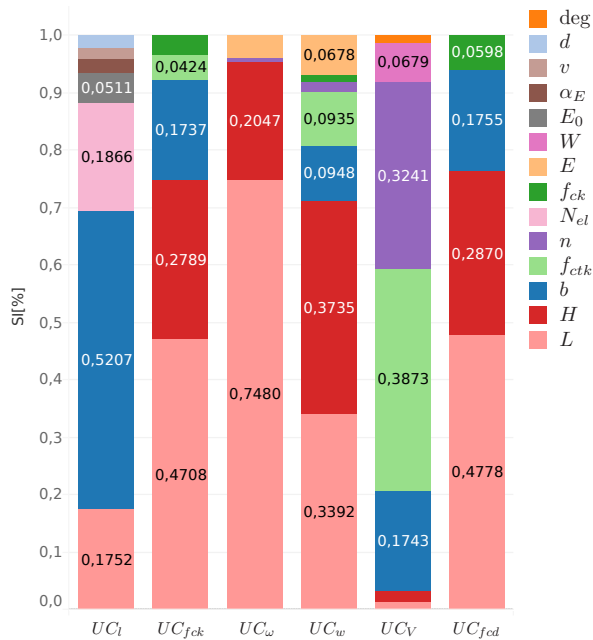
(b) Relative parameter importance [%] for the 'lower-bound' variable range ($8 \leq L < 14$).

(c) Relative parameter importance [%] for the 'upper-bound' variable range ($14 \leq L \leq 20$).

Figure 5.2: Relative parameter importance for the Unity Checks assuming scenario (A), for the total-, lower- and upper-bound variable ranges. The indicated values are a measure of importance in determining the corresponding UC-value.

Performance indicators

In fig. 5.3, the relative parameter importance for the performance indicators and required amount of prestress P is given. Based on the visualisation in fig. 5.3, the following is observed.

- For PI f_1, the number of elements N and the span L are the most important parameters for the lower-bound range. For the upper-bound, the number of cells in the cross-section n becomes dominant while for the total variable range L and N are dominant again. It seems that for larger spans, the mass becomes more important given the higher SI for n.

- The results for f_2 are dominated by the layer width b and span L, for all variable ranges.

- For the required amount of prestress P, the span is the most important parameter. This can be expected, as the acting bending moments increase with a factor L^2. For the lower-bound and total variable range the height H is the second most important parameter, which makes sense as this parameter determines the tendon eccentricity. It turns out that for higher spans however, other cross-section parameters and the material strength become more important. Apparently, for high spans an increasing cross-sectional resistance determined by n and b becomes more important.

Considering the total variable range i.e. complete 3DCP bridge design space, the span L and number of elements N are dominating the total cost of a design and the span and layer width b are dominating the shadow-price of the design. But when narrowing down the design space to a larger-span or smaller-span bridge, these observations change. Therefore, it is hard to draw a general conclusion about which parameters dominate the response of the PI's. Apparently, other interaction effects are playing a role. Therefore, the interaction diagrams of f_1 and f_2 are given in fig. 5.4. Indeed, there are other parameter interactions that influence the SI-results, indicated by the black filled boxes. These interactions explain the differences between the graphs shown in fig. 5.3 and imply that the results only hold for the adopted parameter ranges.
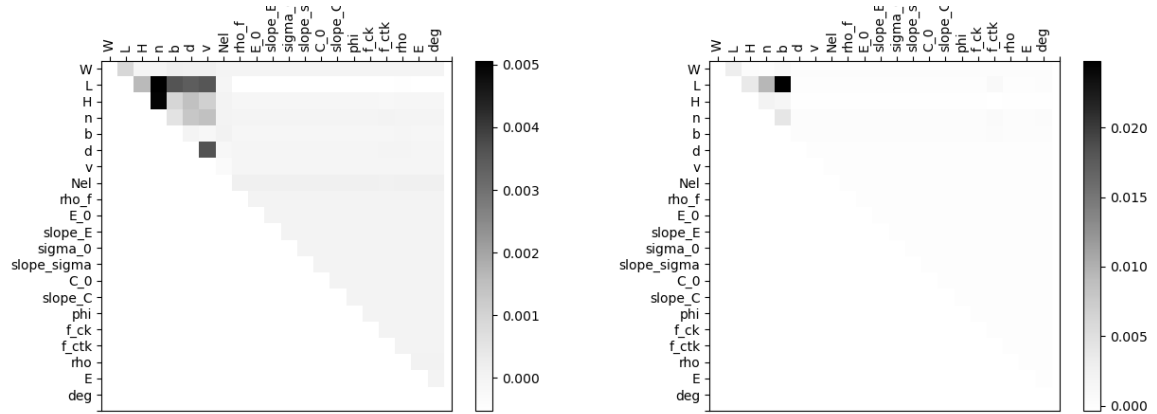
(a) Parameter interactions for PI f_1.

(b) Parameter interactions for PI f_2.

Figure 5.4: Parameter interactions diagrams for the two PIs, showing the presence of other interactions than parameter pair L & H.

(a) Relative parameter importance [%] for the 'total' variable range ($8 \leq L \leq 20$).

(b) Relative parameter importance [%] for the 'lower-bound' variable range ($8 \leq L < 14$).

(c) Relative parameter importance [%] for the 'upper-bound' variable range ($14 \leq L \leq 20$).

Figure 5.3: Relative parameter importance for the performance indicators, for the three different variable ranges. The indicated values are measure of importance in determining the corresponding UC-value.

5.3.3. Conclusions

- The UC for checking the performance of a fresh concrete element is dominated by the layer width, number of elements and the span. Performing the same analysis for the maximum printable height only shows a predominant dependence on the layer width b. This implies that improving the material properties will not yield large benefits. However, since the fresh material properties (viscosity, static yield stress) determine the final layer width, these are of great importance. Implementing the relation between fresh material rheology and layer deformation after extrusion will provide a large improvement of the model.

- The Unity Checks for the final, hardened structure are dominated by the bridge span and cross-sectional geometry. This implies that changing the hardened material strength and stiffness will hardly change the value of these checks. The shear strength however is governed by the tensile strength and total web width, for which improving the material properties will pay-off. However, this only holds if the adopted shear resistance relation eq. (3.9) is valid which should be verified by experimental research.

- Both performance indicators and the required amount of prestress are not influenced by the material properties. The cost-function is dominated by the span, number of elements and print-path geometry. The shadow-price is mostly influenced by the span and layer-width only.

- The presented design graphs can be used as a guideline for designing a short-span bridge ($8 \leq L < 14$), a large span bridge ($14 \leq L \leq 20$) or the entire design space ($8 \leq L \leq 20$) when assuming the same variable ranges as adopted in this study.

5.4. Bond strength reduction

Three different scenarios for the bond strength reduction due to an increasing time interval between two layers are incorporated in the model (see section 4.3.2). By comparing the designs resulting from each of these scenarios, the influence of a bond-strength reduction can be quantified. From fig. 5.2 and fig. 5.3, it can be deduced that the shear strength validation check UC_V, the deformation validation check UC_w and the amount of prestressing P depend on the degree of bond-strength degradation (being none, moderate or high) - albeit of limited *relative* importance. However, this does not yield any information about the *absolute* effect of a strength reduction. Therefore, the effect of this phenomenon is analysed more in-depth.

The previously mentioned output quantities are calculated by varying the horizontal print velocity, for each bond-strength reduction factor. The other design parameters are kept constant, using the following design parameter values: W = 4.5 m; L = 12 m; a = 0 (prismatic beam); H = 0.7 m; n = 5; b = 0.05m ; d = 0.01 m; N = 12; mixture type = Weber 3D 160. Furthermore, it is assumed that the joints are stronger than the concrete i.e. scenario (A) and the amount of prestress is based on limiting the tensile stress in ULS. The results of the analysis are plotted and shown in fig. 5.5. The increase or decrease of the moderate and high bond-strength reduction relative to the result for no bond-strength reduction at $v = 80$ mm/s is given in table 5.3.

Table 5.3: Relative increase or decrease at $v = 80$ mm/s, relative to no bond-strength reduction.

output quantity	moderate decrease	high decrease
UC_V	14.3 %	49.2 %
UC_w	-11.8 %	-29.5 %
P	11.1 %	27.8 %

The importance for selecting an appropriate bond-strength reduction factor is most pronounced for the UC on shear strength UC_V, showing a relative increase of 49.2% for the high reduction. However, this increase is smaller for higher printing speeds. The relative decrease for UC_w and P is smaller however, a too conservative assumption for the bond-strength reduction in time can yield a 28% over-estimation of the required amount of prestress P. Furthermore, UC_w is obviously not governing for this design-case and therefore, accurately estimating the bond-strength decrease is of lesser importance. Moreover, note that the UC_w decreases for increasing reduction, because this increases the required amount of P, but does not decreases the stiffness.

Accurately estimating the degree of bond-strength reduction is especially important for low print speeds. For a low print-speed of 80 mm/s, a high bond-strength reduction yields an increase in P of almost 28% and an increase in UC_V of almost 50 %. The value for UC_w decreases for an increasing bond-strength reduction. These results show that the degree of bond-strength reduction in time is more influential than the horizontal print velocity v. Therefore, it is important to accurately characterise the reduction in bond-strength for increasing layer print times. Using this curve, an optimal print speed can be derived.

(a) UC_V for varying print-speed and degree of bond-strength reduction

(b) UC_w for varying print-speed and degree of bond-strength reduction

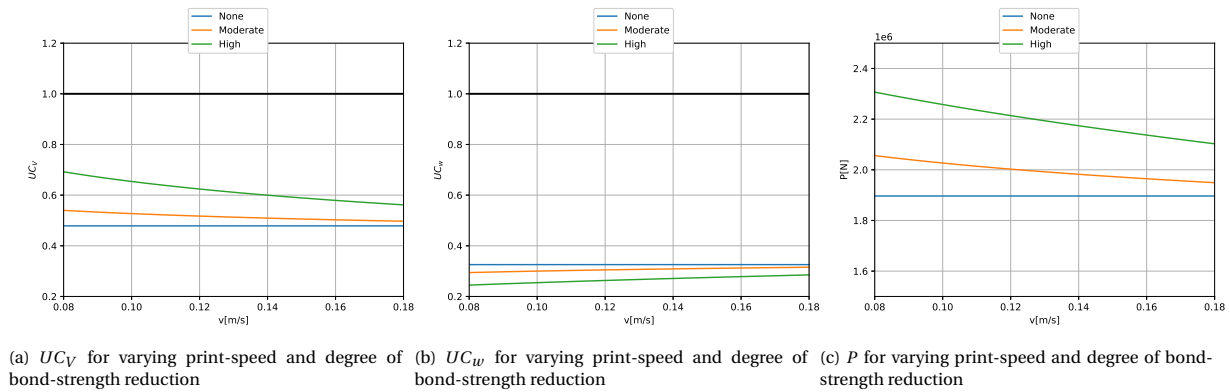(c) P for varying print-speed and degree of bond-strength reduction

Figure 5.5: Absolute influence of varying degrees of bond-strength reduction on affected output quantities.

5.5. Uncertainty analysis

5.5.1. Introduction

Using the currently available literature on 3D printing of concrete, a model for designing a 3DCP bridge considering printing process effects has been established. Given the 3DCP geometry, material properties and process characteristics, the maximum printable height can be predicted and the anisotropic material behaviour due to a decreased inter-layer bond-strength is incorporated. However, in chapter 2 it has already been mentioned that the material properties depend on many other process characteristics, which cannot be predicted yet. For example, the rheology of the concrete filament directly after extrusion changes when the material is sheared in the nozzle prior to extrusion (e.g. when using a nozzle with back-flow, due to a change in cross-section in the system or due to friction in the hose). Furthermore, the temperature and RH of the printing location influence the material rheology, as well as the possible temperature increase due to heating up of the system. The final layer shape depends on the material rheology after extrusion, i.e. a less viscous, sheared material will deform which increases the layer width and decreases the layer height. This means that the final obtained strength and shape of a 3DCP element are prone to random variations.

In this section, the magnitude of these uncertainties is estimated based on available process data. Subsequently, the effect this has on the final design is determined by analysing the propagation of the uncertainty through the model. A schematic overview of this uncertainty propagation is given in fig. 5.6.
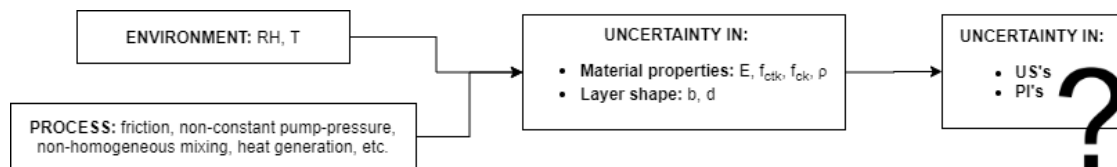
Figure 5.6: Schematic overview of sources of uncertainty and their propagation through the model.

5.5.2. Data analysis: quantification of uncertainty

To quantify the scale of the material uncertainties, a data analysis is conducted. During the production of the 3DCP elements by Weber Beamix and BAM for the bridge in Nijmegen (fig. 3.2), test samples have been printed at the beginning and end of each day of printing, for 30 days. The samples were then tested on flexural strength and compression in three directions, on 7 and 28 days. On each day, the same material, nozzle and printer settings were used. Based on this data, it can be analysed if a significant spread is present between the samples tested in different directions, between the different days of printing or between the samples printed on one day.

In appendix F it has already been proven that both the 28 day flexural strength and compressive strength are independent of the test-direction. This means that per day the data of two times 9 tested samples can be used (9 in the morning and 9 in the afternoon). For the compressive strength, this value doubles to 18 since two compression tests were performed per sample. In fig. 5.7 all data points per day are plotted. In

fig. 5.8a and fig. 5.8b the average means of the entire sample set plus and minus one standard deviation is plotted, together with the daily mean and morning- and afternoon mean. Based on these graphs, it can be observed that on most days, the morning and afternoon averages are close to each other and close to the daily mean. This effect is even more pronounced for the compressive tests, likely because more data-points are included when calculating the mean. The daily means however show a large fluctuation relative to the total mean, sometimes exceeding the standard deviation bound. Again, this observation is more pronounced in the flexural test results. For the flexural strengths, the daily-mean value with the highest deviation from the total mean is measured on day 26, equal to 12.31 MPa which is a variation of 22%. The afternoon mean on day 19 is equal to 12.74 MPa, being the largest variation equal to 26%. For the compressive strength, only one daily mean exceeds the total mean bounds: on day 13 a daily mean of 64.43 MPa was found, corresponding to a variation of 15%. Fortunately, these extreme values are deviating from the mean in positive direction.
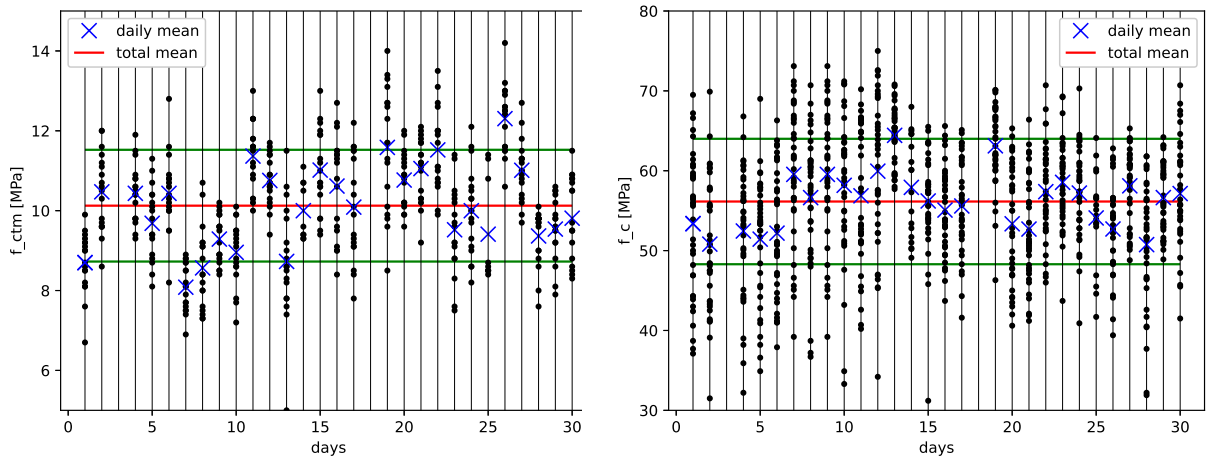
(a) Flexural tensile strength: data points measured on a single day and overall mean value.

(b) Compressive strength: data points measured on a single day and overall mean value.

Figure 5.7: Summaries of all daily measurement results.
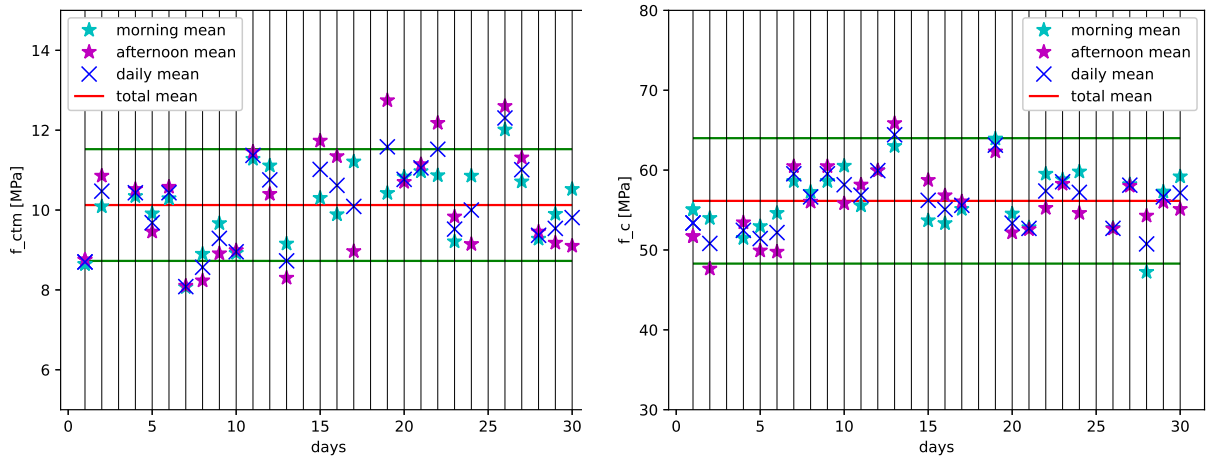
(a) Flexural tensile strength: total mean +/- one standard deviation together with the daily, morning and afternoon means. Based on 18 values per day: 9 in the morning and afternoon.

(b) Compressive strength: total mean +/- one standard deviation together with the daily, morning and afternoon means. Based on 36 values per day: 18 in the morning and afternoon.

Figure 5.8: Summaries of total and daily average measurement results.

Based on these qualitative observations on the measurement data, the following can be concluded.

- The spread observed in the complete sample is more likely due to a variation in the process characteristics between days. This can be due to the changing environmental conditions, due to a small difference in concrete batch or even due to a different operator managing the printer system.

- Given the small difference between the morning- and afternoon averages, it seems that this process does not introduce large variations in the measured material data.

- The daily values sometimes even exceed the uncertainty based on the total sample. This emphasizes the importance of understanding the cause of these variations. However, the maximum variation is only 26%. This implies that the total uncertainty induced by these unknown process characteristics affecting the material properties, is maximal 26 %. In chapter 5, the effect of these uncertainties on the model output is analysed.

5.5.3. Uncertainty propagation

In this section it is analysed to what extent these process uncertainties influence the model output i.e. a bridge design - independent of the source of the uncertainty. From the previous sensitivity analyses, it has turned out that the characteristic tensile- and compressive strengths influence the design checks $UC_{f_{ck}}$, UC_w, UC_V and $UC_{f_{cd}}$ and the required amount of prestress P. The considered uncertainty range is a normal distribution with mean and standard deviation of the total dataset of material measurements, summarized in table 5.4.

Table 5.4: Normally distributed uncertainties induced by the printing process, for the compressive and tensile strength of the Weber 3D 160 mortar.

parameter	RS	μ [MPa]	σ [MPa]
f_{ck}	14%	30.0	4.20
f_{ctk}	14 %	4.86	0.67

Subsequently, in a Monte-Carlo analysis the parameters f_{ck} and f_{ctk} are picked randomly within the corresponding normal distribution. All other parameters are constant: $W = 4.5$m, $L = 12$m, $H = 0.9$m, $n = 5$, $b = 0.05$m, $d = 0.01$, $v = 0.12$m/s and a moderate bond-strength reduction is assumed. In total 10,000 parameter samples are randomly drawn and the recorded outputs are plotted in a histogram to derive the distribution of the outputs, given in appendix E.2. Subsequently, the output data is fitted using a normal distribution. The resulting relative spreads are summarised in table 5.5. The relative spread of the output quantities is lower for P, UC_w and UC_V and higher for $UC_{f_{ck}}$ and $UC_{f_{cd}}$, but close to the relative spread of the input parameters. This means that the input uncertainty is not enlarged by the model. Furthermore, in structural design, parameter uncertainty is accounted for by the use of safety factors. For unreinforced concrete, the strength must be divided by $\gamma_M = 1.5$ and multiplied with $\alpha = 0.8$, yielding a reduction of 47%. Because this reduction is larger than the obtained parameter uncertainty and given that the error is not amplified in the model, it can be concluded that this parameter uncertainty does not affect the safety of the bridge design.

Table 5.5: Uncertainty analysis: relative spread of output quantities for a given parameter input distribution.

output quantity	P	UC_{fck}	UC_w	UC_V	UC_{fcd}
RS	9.78 %	17.89%	12.87%	9.31%	14.84 %

5.6. Conclusion
From the analyses performed in this section, the following conclusions can be drawn.

- The model generates a 3DCP bridge design as expected and fulfills the model requirements defined in chapter 4.

- The layer width b clearly dominates the maximum printable height of the fresh concrete structure, while the fresh material properties are of minor influence. Therefore, it is important to control the final layer width as a function of the material properties, nozzle geometry and pump pressure. This implies that indirectly, the fresh material properties are of importance.

- The bridge geometry described by the height H, span L, number of webs n and layer width b of the structure dominates the value of all model output quantities. This implies that for designing a 3DCP bridge structure, optimising the size and shape of the bridge is more effective than choosing the right material type. Only for the shear strength design validation check, the material properties are of influence, together with the total web width. The UC for bending is satisfied by applying sufficient prestress. This required amount is dominated by the material properties as well.

- The degree of the decrease in bond strength might be crucial for the value of the unity check on shear and largely influences the required amount of P. The degree of decrease is more influential than the print velocity v and therefore accurately characterising the bond-strength reduction as a function of layer print time is important.

- The uncertainty analysis has shown that material property variations are most likely caused by environmental influences like temperature and RH, rather than by process effects in the printer system. The model does not capture these variations, as they cannot be described today. The effect of these uncertainties on the model output is analysed and it is concluded that the material parameter uncertainties are covered by the design safety factors.

6

Case studies

6.1. Introduction

In this chapter, the potential for using the established model as a design and optimisation tool is demonstrated. In the first case, the 3DCP bridge design will be optimised in terms of cost and sustainability using the parametric model and the attained knowledge in chapter 5. The starting point is an actual design case for a bridge in Noord-Holland which Witteveen+Bos is currently working on. Additionally, several future design variations are discussed. In the second case, the bridge design of Gemert (fig. 1.1) is used to compare the performance of the bottle-shaped- and box-girder cross-section topologies, reflecting on the printability constraints.

6.2. Case-study: 3DCP bridge Voordijksloot

6.2.1. Case-study introduction

Witteveen+Bos is currently designing four 3DCP bridges in the Dutch province Noord-Holland, each having different design requirements. In this chapter, the design of the bridge spanning the 'Voordijksloot'-river is analysed in detail and strategies for optimising the design are discussed. In fig. 6.1 an artist impression of the 3DCP bridge spanning the Voordijksloot is shown. The curved edges improve the aesthetics of the bridge and can be easily manufactured using 3D concrete printing. The main, load-bearing part of the deck is a straight plate having a box-girder cross-section. The design requirements for this bridge are listed hereafter:

- span L = 9.4 m; width W = 5.0 m; layer width b = 50 mm;

- the required amount of prestress must be designed to limit the tensile stress at mid-span in ULS to the design tensile strength;

- during construction e.g. in SLS, the tensile stress at the top-fiber at support-level may not exceed the tensile strength;

- it may be assumed that the joints have a higher design tensile strength than the concrete (i.e. scenario (A));

- the bridge is printed using the Weber 3D 160 mixture.

An initial design has already been made, which is based on satisfying the design validation checks in hardened state. Given this design, the maximum printable height and resulting number of elements is calculated. This yields the following design specifications:

- height H = 700 mm; number of openings n = 6 i.e. 7 webs;

- required prestress P = 914 kN with an eccentricity from the c.a. of 250 mm;

- SLS: $UC_{f_{ck}}$ = 0.06, UC_ω = 0.39 and UC_w = 0.19;

- ULS: UC_V = 0.32 and $UC_{f_{cd}}$ = 0.27;

Figure 6.1: Artist impression of the bridge spanning the Voordijksloot, made by and received from Witteveen+Bos.

- assuming a layer-height of 1 cm and a print-speed of 120 mm/s yields a maximum printable height $l = 0.72$ m, which means that at least $N = 14$ elements are required;

- PI's: $f_1 = €45206$ and $f_2 = €294$

In the subsequent sections, this initial design is optimised for minimising cost and environmental impact using the parametric model and the results from chapter 5. Secondly, a feasibility study is performed for an increased span, showing the potential of the parametric design model. Finally, the potential of several future optimisation solutions is discussed.

6.2.2. Design optimisation: minimise f_1 vs. f_2
Optimisation formulation & method
The definition of optimisation is stated as: "The determination of values for **design variables** which minimize (or maximize) the **objective**, while satisfying all **constraints**" [55].

In this case, the minimisation **objective function** is defined as one of the two performance indicators being $f_1(\mathbf{x})$ of $f_2(\mathbf{x})$. The **constraints** are the design validation criteria or UC's. In order to limit computation time, only $UC_l(\mathbf{x})$ and $UC_V(\mathbf{x})$ are selected as these are expected to be governing. The validity of the remaining criteria is verified afterwards. In the previous chapter, it has been concluded from the relative parameter importance study that the parameters N, L, v, d, n, b, H and W are most influential for the UC's and PI's. This means that these parameters will be included as **variable design** parameters during optimisation. Since the span L and width W are fixed by the boundary conditions, the design variable set reduces to $\mathbf{x} = [H, n, b, d, v, N]$. The bounds for $\mathbf{x}$ are defined as follows: [lb, ub] = [0.5, 3, 0.03, 0.009, 0.08, 2], [1.5, 8, 0.1, 0.02, 0.18, 20]. The remaining parameters, being the parameter describing the material properties, will be fixed during optimisation according to the Weber 3D 160 mixture.

The design optimisation runs carried out in this section are performed using the Trust-Region constrained optimisation algorithm available in the Scipy package for Python. This is a 2nd order multi-variate constrained optimisation algorithm. It essentially is a variation to the Newton's method which seeks the optimum using 2nd order derivative information. The local approximation is made within a trust region Δx, which is adjusted based on the approximation quality, thereby creating a sub-problem that is solved every iteration. This makes the method rather expensive, but robust. The algorithm requires second-order derivative information, which is acquired using central finite differences. Details about the implementation of the algorithm and the calculation of the input quantities are given in appendix G.

Optimisation results
The design for the bridge spanning the Voordijksloot is optimised for minimising the cost-performance indicator $f_1(\mathbf{x})$ and sustainability indicator $f_2(\mathbf{x})$ separately, assuming $L = 9.4$m, $W = 5$m and using the Weber 3D 160 printable mortar. This is done for all three bond-strength reduction scenarios: no, a moderate or high reduction. The results are summarized in table 6.3. The resulting bridge design for minimising the cost-function is indeed cheaper than the resulting design for minimising the environmental footprint, which is

more sustainable. Note that the bridge for minimising cost consists of only 4 elements, while the sustainable design consists of 22 elements. This is because more elements do not increase the environmental footprint, while this does increase the costs. Therefore, the algorithm focuses on decreasing the weight and required amount of prestress, not caring about the number of elements. Moreover, the cost-minimised bridge is heavier and contains more prestress than the reference design and the sustainable design, again emphasizing that the need for minimising the number of elements is priority in this case. The sustainable design clearly requires the least amount of material. Furthermore, notice that for minimising the total cost, in which the buildability of the fresh structure is governing, the layer-width is increased to its maximum value of 100mm, which is in accordance with the results found in chapter 5. Apparently, it is more beneficial to minimise the printing speed to 0.8 m/s to have a long layer printing time allowing the material to gain strength and stiffness before deposition of the next layer, than printing at the maximum speed of 0.18 m/s. However, when including a bond-strength reduction factor, the print speed clearly increases in order to minimise the strength reduction. The reduced strength clearly results in a higher required amount of prestress, while the geometry of the cross-section remains constant. For the sustainability minimisation, the printing velocity maximises in order to limit the strength decrease. This results in a lower element height which increases cost. The increase in required amount of prestress is pronounced, however the increase in f_2 is limited.

Table 6.1: Optimisation results: overview of designs with $\mathbf{x}$ = [H[m] n[-] b[mm] d[mm] v[mm/s] N[-]], assuming the **degree** of bond-strength reduction is no, moderate or high bond-strength reduction (SP = shadow price).

design case	degree	x	$\mathbf{M}$[kg]	$\mathbf{P}$[kN]	UC_V	l [m]	f_1	f_2
initial design	none	[0.7; 6; 50; 10; 120; 14]	17138	914	0.32	0.72	€45206	€294
min. cost	none	[0.5; 3; 100; 10.1; 81.3; 4]	23515	1962	0.50	2.59	€27622	€428
min. cost	moderate	[0.5; 3; 100; 9.0; 91.3; 4]	23515	2223	0.55	2.58	€27688	€437
min. cost	high	[0.5; 3; 100; 9.0; 91.4; 4]	23515	2703	0.68	2.57	€27792	€457
min. SP	none	[0.9; 3; 30; 9.0; 80.0; 18]	8991	592	0.65	0.51	€56276	€158
min. SP	moderate	[0.89; 3; 30; 9.0; 180; 49]	8955	657	0.69	0.19	€107558	€160
min. SP	high	[0.87; 3; 30; 9.0; 180; 49]	8884	818	0.80	0.19	€107510	€164
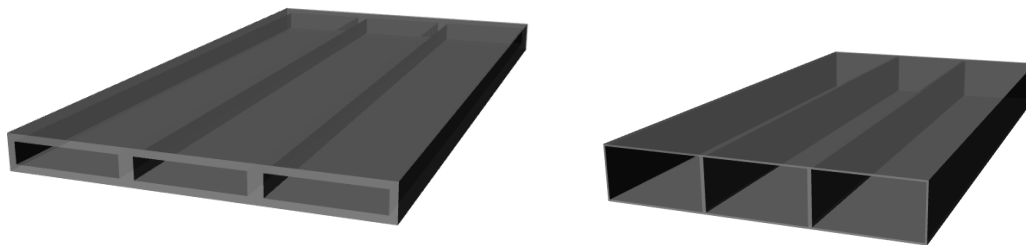
Figure 6.2: Visualisations of the cost-optimised design (left) and of the sustainable design (right).

Multi-objective optimisation

The optimisation results clearly show a Pareto front: optimising one objective function is only possible by making the other objective worse. There does exist an optimal solution considering both objective functions. This Pareto optimum is found by minimising the weighted sum of the two objectives:

$$f = w_1 \cdot f_1 + w_2 \cdot f_2 \tag{6.1}$$

in which the weights w_1 and w_2 are set to 1.0, because the two objective are considered to be equally important. The boundary conditions are similar to the previous optimisations and it is assumed that there is no bond-strength reduction.

A summary of the resulting design is given in table 6.2 together with a visualisation in fig. 6.3. In fig. 6.4, a visualisation of the design is given, together with an overview of all design optimisations performed in this sections. This graph clearly depicts the presence of the Pareto front and the multi-objective optimal design.

Table 6.2: Resulting design for Pareto optimal design, $\mathbf{x}$ = [H[m] n[-] b[mm] d[mm] v[mm/s] N[-]].

design case	degree	x	M[kg]	P[kN]	UC_V	l [m]	f_1	f_2
multi-objective	no	[0.8; 3; 57; 9.3; 90; 8]	16034	487969	0.50	1.16	€34922	€262
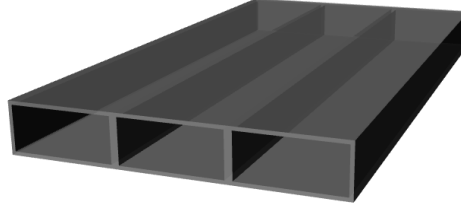
Figure 6.3: Visualisation of the multi-objective optimised design.

6.2.3. Scenario (B): zero joint strength
The previous analyses all have been conducted assuming that the joints are stronger than the concrete when entering the tensile regime. However, this is far from trivial and therefore the consequences are analysed when assuming the joints have zero tensile strength. In this case, the concrete cannot deliver any tensile strength and therefore the prestressing steel is responsible for providing sufficient bending moment resistance. Unfortunately, the previous bridge designs cannot be redesigned using the optimisation algorithm due to the non-continuous relations between design variables and model outputs for this scenario. The functions must be at least twice differentiable to be able to be passed to the algorithm. Therefore, the bridge is redesigned iteratively by starting from the designs obtained in the previous section, again using the parametric model. Note that for scenario (B) the required amount of prestress and bending checks do not depend on the bond-strength reduction in time - this will only influence the shear strength. Therefore, starting points are the zero bond-strength reduction designs and in each iteration it is manually verified if the design checks are satisfied.

Both designs initially do not have sufficient bending moment capacity. The first step is therefore to redesign the amount of prestress based on requiring a compression-only structure in SLS. The cost-minimised design now satisfies the bending check at mid-span, for an increased amount of prestress with 1000 kN. This leads to a minor increase in total construction cost and shadow-price. The more slender, sustainable design does not fulfill the bending check right-away. Therefore, the design must be altered by (1) increasing the height which increases the tendon eccentricity or by (2) increasing the required amount of prestress which can be done in this case by increasing the number of webs. The first option yields the most sustainable design, requiring a small increase of prestress, but a significant increase in shadow-price and construction cost due to the increased mass.

Table 6.3: Iteration results assuming scenario (B): overview of designs with $\mathbf{x}$ = [H[m] n[-] b[mm] d[mm] v[mm/s] N[-]].

design case	x	M[kg]	P[kN]	UC_V	UC_M	l [m]	f_1	f_2
min. cost (A)	[0.5; 3; 100; 10.1; 81.3; 4]	23515	1962	0.50	-	2.59	€27622	€428
min. cost (B1)	[0.5; 3; 100; 10.1; 81.3; 4]	23515	1962	0.60	1.69	2.59	€27622	€428
min. cost (B2)	[0.5; 3; 100; 10.1; 81.3; 4]	23515	2942	0.46	0.99	2.59	€27881	€462
min. SP (A)	[0.9; 3; 30; 9.0; 80.0; 22]	8991	592	0.65	-	0.51	€57969	€158
min. SP (B1)	[0.9; 3; 30; 9.0; 80.0; 22]	8991	592	0.65	2.2	0.51	€57969	€158
min. SP (B2)	[0.9; 3; 30; 9.0; 80.0; 22]	8991	970	0.60	1.16	0.51	€64376	€171
min. SP (B3)	[1.5; 4; 30; 9.0; 80.0; 22]	12866	748	0.34	1.0	0.97	€73858	€222

6.2.4. Feasibility study: increased span
Using the current span of 9.4m the bridge foundation will intersect with the existing pile-foundation of an adjacent culvert. Therefore, the client asks to increase the span with 5 meters on both sides to L = 19.4 meters.
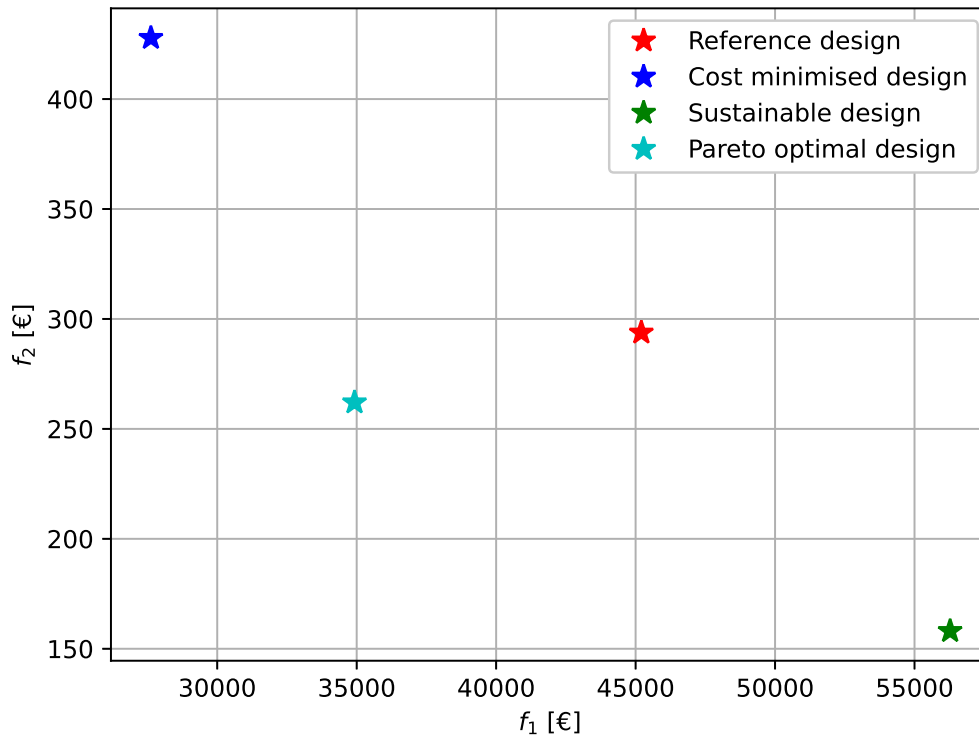
Figure 6.4: An overview of the different design optimisations on the Pareto front.

In this section, the feasibility of increasing the span is analysed using the parametric design tool. The width is equal to $W = 5$m, again using the Weber 3D 160 mortar. The bridge is designed using the cost minimisation optimisation algorithm, using the same design variable set. It is assumed that there is moderate loss in bond-strength in time and that the joints are stronger than the concrete. The required amount of prestress is designed for limited tension in ULS. The resulting bridge design is visualised using the Grasshopper design tool as shown in fig. 6.5. The results are summarized in table 6.4. The increased span is mainly compensated for by increasing the amount of prestress. It turns out that using 8 elements is sufficient. However due to the increased slenderness of the structure, an additional dynamic verification needs to be performed according to NEN-EN 1990 A2.4.3.2 because the eigenfrequency $\omega_n < 5$ Hz. All other checks are satisfied and the total cost is equal to $f_1 = €63161$ and the shadow price is equal to $f_2 = €1398$. It is therefore concluded that it is feasible to increase the span of the bridge, under the condition that an additional dynamic verification must be performed. The same conclusion holds when assuming the joints have no tensile strength i.e. scenario (B). It turns out that the applied amount of prestress is sufficient for delivering the required bending moment capacity, since $UC_M = 0.85$ and $UC_P = 0.67$.
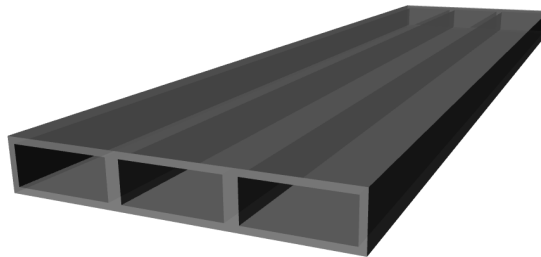
Figure 6.5: Visualisation of the optimised design for an increased span of $L = 19.4$ m.

Table 6.4: Resulting design for increased span, $\mathbf{x} = [H[\text{m}]\ n[\text{-}]\ b[\text{mm}]\ d[\text{mm}]\ v[\text{mm/s}]\ N[\text{-}]]$.

design case	degree	x	$\mathbf{M}$[kg]	$\mathbf{P}$[kN]	UC_V	l [m]	f_1	f_2
$L = 19.4$m	moderate	[0.8; 3; 100; 9.0; 108; 8]	55934	7540	0.52	2.44	€63181	€1398

6.2.5. Future optimisation solutions
Kinked tendon profile
For calculation of the shear resistance using (3.9), it is important that no cracks are present at support level. To ensure this, in scenario (A), the stresses must be smaller than f_{ctd}, but in scenario (B) the tensile stresses must be smaller than 0. In the design, the prestressing tendons are straight and applied eccentrically, which may cause tensile stresses at support level. Therefore, a variation to the linear tendon configuration is assessed having a kinked tendon profile as depicted in fig. 6.6. In this way, no tendon eccentricity is present at support level, but the desired eccentricity at mid-span can be achieved. In existing external prestressing applications, the kinks are introduced at saddles, which are capable of carrying the high local forces that are generated. The solution for introducing the kinks in a 3DCP structure is considered out of the scope of this research. In this section, the theoretical benefit of such a solution is presented.
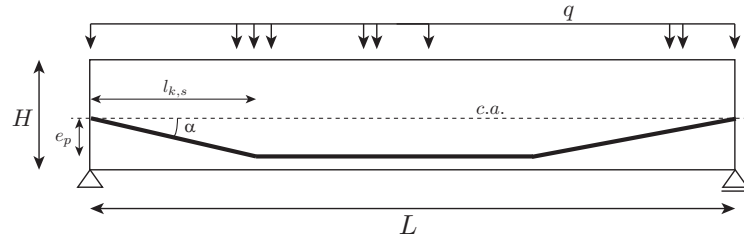
Figure 6.6: Longitudinal cross-section with a kinked tendon profile lay-out

An additional variable in the kinked tendon lay-out is the length of the sloped part, called l_p. Together with the tendon eccentricity at mid-span e_p, this determines the slope and thereby the magnitude of the upward bending moment at mid-span, equal to $M_P = P\sin(\alpha)l_p$. Note that for small angles, this relation simplifies to $M_P \approx P\alpha l_p \approx Pe_P$, similar to the linear tendon lay-out. The required amount of prestress is plotted against the sloped length, for various bridge spans L, see fig. 6.7 (all other parameters are kept constant at average values). It is clear that the benefit of a large kink is more pronounced for large spans. This can be explained, as for large spans, the tendon eccentricity in a linear tendon must be highly reduced to prevent cracking at support level, at the cost of an increasing amount of P. Note that a kinked tendon profile is beneficial only in case the slope is larger than about 2 metres.

Non-prismatic beam
As already introduced in section 3.1.2, the possibility of printing a non-prismatic beam is included in the research model. The straight bottom chord can be translated into a curved line with an offset a at mid-span, creating an arch which yields a higher tendon eccentricity at mid-span, reducing the required amount of prestress. Printing such a geometry requires the printing of cantilevering layers, which is only possible for very stiff materials or when using an infill support material. In this research, the potential benefit of arching the bottom line from a structural point of view will be assessed assuming it is possible to print cantilevering layers.

By introducing a curve at the bottom side of the beam while keeping the top-side straight, a non-prismatic cross-section arises. This is beneficial, since the tendon eccentricity at mid-span increases, which decreases the required amount of prestress. In fig. 6.8, the absolute decrease of P for increasing a is depicted. The entire spectrum of possible designs is plotted (blue dots). In red average interval values are plotted in which a more distinct trend is visible. The average decrease in P is 40% but this number may vary depending on the values of the other design parameters.
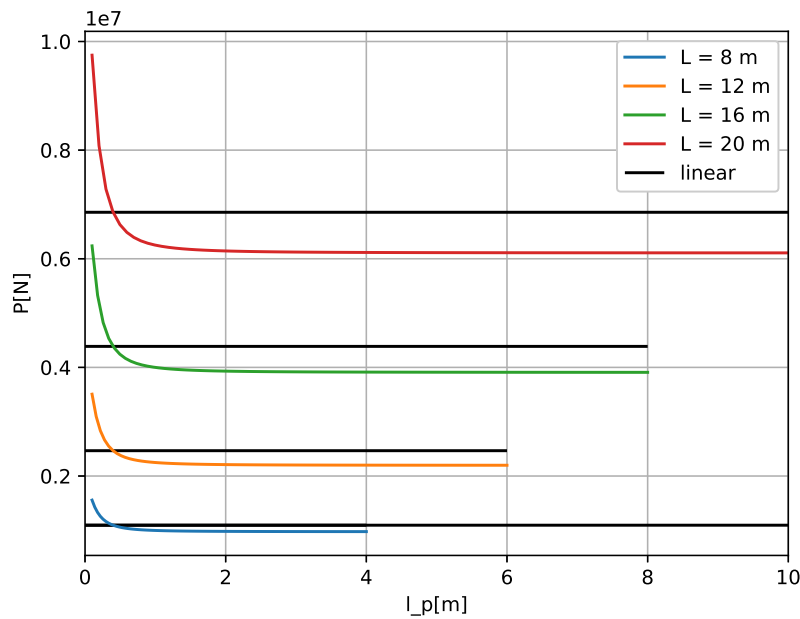
Figure 6.7: Required amount of P for various spans.

6.3. Case study: bottle-shape vs. box-girder

As discussed in the introducing chapter of this thesis, the preceding generation of 3DCP designs has a bottle-shape cross-section (Gemert, Nijmegen). The major reason for using a box-girder cross-section is the expected material savings. However, there are also drawbacks of the box-girder design. The pros and cons of using this new cross-section are discussed hereafter.

The main challenge encountered in the box-girder design is the lower resistance to buckling due to the larger unsupported 'wall'-parts. The bottle-shape design contains more internal supports in the print-track, allowing for a higher possible element height. Based on the bridge design for Gemert which was printed with the Weber 3D 115-1 mix, the two alternatives are compared hereafter.

The bridge consists of six elements of 1.08m height, having a layer-width of dxb = 12x60 mm, resulting in 89-90 layers per element. The print-track length per layer equals 25.1m and the total required concrete mass was $A \cdot L \cdot \rho = 1.40 \cdot 6.5 \cdot 2000 = 18.2$ tons. Consider now the same boundary conditions and layer geometry, but using a box-girder topology. The bridge is designed such that the layer height is maximised, which can be done by decreasing the height H and print speed v and increasing the number of cells n. Despite these efforts, it turns out that the maximal printable height only reaches $l = 0.43$ meters, which is less than half that of the bottle-shaped topology. This can have the following three causes.

- The bottle-shaped topology has a longer printpath: 25.1 meters compared to only 15.8 meters for the box-girder. This limits the stiffness increase before deposition of the next layer, decreasing the buckling resistance.

- The bottle-shaped topology provides more internal support, because the length of an unsupported wall-part is smaller. Moreover, the vertical wall parts at the bottom are more supported because the bottom flange has a doubled thickness.

- The model that is used to describe this maximum element height provides a convervative lower-bound of the actual printing height - assuming the internal 'walls' are simply-supported. Moreover, the accuracy of the model strongly depends on the calibration of the material parameters and it is known that these are prone to large variations.

So, despite the fact that designing a bridge using the box-girder topology saves material weight (12.5 tons vs. 18.2 tons), the maximum attainable element height is lower. This requires more 3DCP elements which
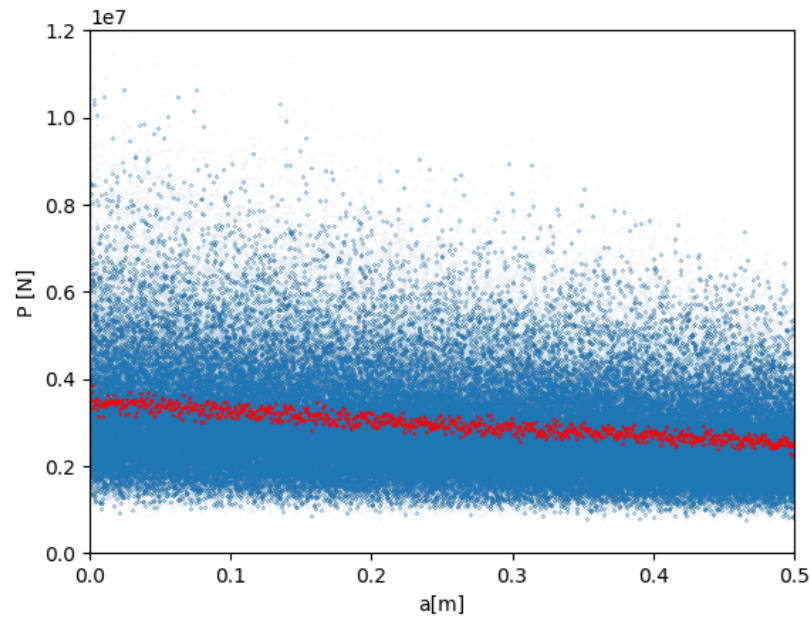
Figure 6.8: Decreasing P [N] for increasing a[m]
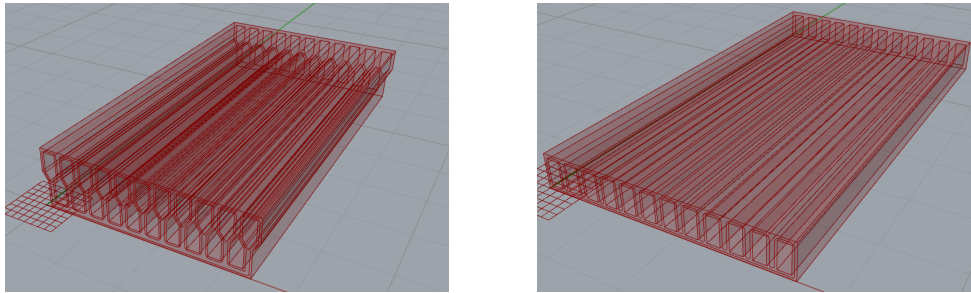
Figure 6.9: Visualisation of the Gemert bridge design for L: a bottle-shaped cross-section and R: a box-girder cross-section topology.

increases cost. It is expected that the main cause for this decrease is the shorter print-path length. This should be taken in consideration when designing 3DCP bridges having a smaller width.

6.4. Conclusion

- For the cost-minimised design, the maximal printable height is governing the result since joints are expensive. The more sustainable design is more slender in order to minimise weight and amount of prestress, making the shear strength critical.

- It is possible to increase the span of the bridge with 10 meters if the bridge satisfies the additional dynamic verification check.

- When assuming the joints have no strength, the optimised designs do not have sufficient bending moment capacity. To satisfy the bending checks, the required amount of prestress must be increased.

- Introducing a kinked tendon profile reduces the required amount of prestress when assuming the joints have no strength, especially for large spans ($L > 16$m).

- A thinner cross-section at mid-span reduces the required amount of prestress up to 40%, but requires the printing of cantilevering layers.

- In terms of printability, the bottle-shaped cross-section is more feasible than the box-girder topology. This is likely because the print-path is shorter, limiting the material to gain sufficient strength.

7

Conclusion and recommendations

7.1. Conclusion

In this research, a link between the manufacturing process and structural design of a 3DCP structure is established, focusing on a 3DCP cyclist bridge, with the aim to answer the following research question:

"What is the influence of printing process parameters and 3D printable concrete material properties on the structural design of a 3DCP cyclist bridge and how can this design be optimised to unlock the potential of cost-effective and sustainable bridge structures?"

After performing an extensive literature study, it turns out that the following printing process aspects influence the global structural performance of the final, hardened structure:

- Depending on the material properties, printing process characteristics and print-path lay-out, a fresh concrete structure might fail during printing by either plastic collapse or elastic buckling. The maximum possible height of the fresh concrete structure before failure determines the total number of elements in the bridge.

- Due to the layer-wise build-up of the structure, the material properties may become anisotropic due to a decreased bond-strength between two subsequent layers. This lower bond-strength results in a decreased flexural tensile strength of the 3DCP bridge structure.

- The installation of traditional reinforcement solution into a 3DCP structure is not trivial. Other solutions for improving the ductility of the structure exist, such as the inclusion of steel fibers into the concrete mix, the on-line printing of a thin reinforcement cable embedded in the concrete filament or reducing the tensile stresses by applying prestress.

These effects are included in the parametric research model that has been established. The model generates 3DCP bridge design alternatives as a function of 22 user-defined parameters describing the printing process, material properties and bridge geometry. The structural performance of the fresh concrete structure is evaluated using analytical equations, based on the prediction model described in [2]. Modelling the structural performance of the structure in hardened state using analytical equations proves to be a safe and accurate simplification, validated by a detailed FE analysis. The effect of a decreased bond-strength on the design feasibility can be assessed by defining a bond-strength reduction for increasing layer print time. Hence, the parametric research model can be used as a practical tool for designing and analysing 3DCP bridge structures.

After performing a global sensitivity analysis using the parametric model, it is found that the performance of the fresh concrete element is mainly governed by the layer width b. However, the final layer geometry is determined by the viscosity of the material which is dependent on the interplay between material properties, nozzle geometry and printer settings. If the material is stiff, the layer-size is equal to the nozzle but more fluid materials deform after deposition. Therefore, it is important to be able to control the final layer geometry as a function of these parameters. The Unity Checks for the hardened state are dominated by the bridge

span and cross-sectional geometry. The material properties are only important for the shear-resistance validation check, together with the total web width. However, it is noted that it is uncertain if the adopted shear resistance calculation is applicable for this material, since the aggregate size is lower than for conventional concretes. The performance in terms of cost and sustainability of the final, hardened bridge structure is dominated by the printing process- and geometry parameters, not by the material parameters. These results imply that when optimising a 3DCP bridge design, optimising the topology of the cross-section and boundary conditions is more effective than changing the material properties.

The effect of a decreasing bond-strength as a function of the layer printing time on the global structural performance is assessed. It turns out that an accurate characterisation of this strength decrease function of time is more important than finding an optimal print-velocity.

Material strength data of 3DCP samples showed a significant uncertainty in the measured strength properties. This implies that there is a large number of unknown printing process parameters influencing the mechanical properties and thus structural performance, which have not been included in the model. Allocating the source of this uncertainty showed that the printing process itself is well under control, but environmental aspects like RH and temperature might be of large influence, since large differences between subsequent testing days were found. An uncertainty analysis showed that these parameter uncertainties do not lead to larger uncertainties in the model output than covered by the material safety factors.

To show the potential of the model for analysing and optimising 3DCP bridge designs, the design for a 9.4 meter span bridge is optimised for minimising cost and environmental footprint. For the cost-efficient design, the maximum element height is the governing design criterion, since additional joints are expensive. For the sustainable design, focus is on minimising the amount of prestress in which the shear strength design check is governing, yielding a different cross-section and a higher number of elements. These differences illustrate that cost-efficient designs are not the most sustainable alternative and vice-versa. An additional feasibility study shows that increasing the span with 10 meters is possible only after performing an additional validation check for the dynamic behaviour of the structure, because the slenderness has increased. Comparing the design of the bottle-shaped cross-section with the box-girder topology shows that the maximum printable height of the box-girder is lower than that of the bottle-shaped design, most likely because the layer print time is much shorter. This result confirms the importance of integrating the design- and printing process.

The previous conclusions are based on assuming that the joints between the 3DCP elements are stronger than the concrete. Therefore, a scenario in which the joints have zero tensile strength is assessed as well. Analyses show that in this case, the previously optimised designs do not have sufficient bending moment capacity. Only after increasing the amount of prestress and increasing the internal lever-arm, the design checks are satisfied. These results emphasise the need for adequately estimating the joint tensile strength.

Looking forward to the future of 3DCP bridges, the feasibility of two future design optimisations is discussed. It is shown that introducing a kinked tendon-profile is beneficial for large span bridges ($L > 16m$) when assuming the joints have no strength. However, an adequate solution is required to distribute the high local forces introduced at the kinks. Introducing a non-prismatic bridge cross-section by curving the bottom-line can yield a reduction of the required amount of prestress up to 40%. Note that this solution requires the printing of cantilevering layers, for which the structural performance in fresh state should be assessed using numerical modelling.

The conducted research shows that the printing process and the design process of a 3DCP structure are closely interrelated. Considering the printing process during structural design results in more cost-efficient and sustainable structures. The geometry of the cross-section and the structure's boundary conditions are most influential in determining the feasibility and performance of a 3DCP bridge design - the material properties are of smaller influence. The novel analytical parametric modelling approach proves to be a useful tool to analyse and design 3DCP structures in a fast and accurate way. Hence, this first attempt of integrating the printing process into the structural design of a 3DCP structure using an efficient model has succeeded and can serve as a basis for further research and design optimisation.

7.2. Recommendations

This research is a small contribution to the rapidly growing amount of knowledge about 3D concrete printing. Today, a lot of research is being conducted to better understand and model the 3DCP process. The results of this research have shown that considering the printing process during the structural design of a 3DCP structure is important. However, there are many missing links in coupling the printing process with the structural design. To improve the parametric research model that has been established and to enrich and reinforce the conclusions made in this research, the following set of recommendations for future research are proposed:

- The layer width after extrusion turns out to be an important parameter for the design feasibility and performance. Therefore, it is important to be able to predict the deformation of a layer as a function of the material properties, nozzle geometry, pump pressure and external environment. A simplification of this complex mechanism can today be described using detailed numerical dynamic flow simulations. It is desired to have simple, analytical models to describe the material behaviour in the nozzle to predict the actual layer width.

- Investigate the applicability of the existing empirical models to calculate the shear resistance of a cross-section for printable concrete structures or derive an accurate alternative shear resistance prediction model.

- Analysis on material data has shown that differences exist between samples printed on different days. Therefore it is likely that the material properties are sensitive to the RH and temperature of the printing environment. Because these relations are unknown yet, material tests should be performed to remove uncertainties in the material properties.

- Different models exist to predict the creep and shrinkage of a concrete structure. It is however unknown if these models are applicable for 3DCP structures which should be verified by conducting experiments as a function of the different parameters. Alternatively, new models can be derived to predict the creep- and shrinkage deformation of 3DCP structures. It is recommended to verify this for the young, hardening element and final, hardened structure.

- This research has shown that the strength of the joint epoxy material influences the global structural performance. Therefore, an accurate characterisation of this strength and the identification of factors influencing it is important.

- The model that has been used in this research for predicting the maximum object height of the fresh concrete structure is valid for straight wall structures only. However, it turned out that integrating a curved bottom section is beneficial as the required amount of prestress decreases. However, a structure printed with cantilevering layers will fail earlier and therefore, predicting the maximum object height for a structure built with cantilevering layers would be a great improvement of the model.

- The modelling technique adopted in this research using simplified analytical equations has proven to be a fast and accurate approach. It is recommended to increase the use of this approach to efficiently analyse and optimise concrete structures, both 3D printed and constructed using traditional concrete casting.

The parametric model established in this research can be used as a design tool for structural engineers. The conclusions of this research reflect enrich the knowledge base on which engineers design structures. Although researchers and industry are working closely together on improving and optimising the 3DCP process, the following set of recommendations is proposed more specifically for structural engineers designing 3DCP bridge structures:

- The parameter study has shown that the cross-section geometry is most influential for the feasibility and performance of the 3DCP bridge design. Therefore, it might pay-off to further optimise this. Moreover, for cost-efficient structures, the height of an element should be maximised.

- When designing a 3DCP structure, a decrease in bond-strength for increasing layer print time is important as it directly decreases the flexural tensile strength. Therefore it is important to accurately determine the decrease in inter-layer bond-strength. Based on this function, the print-velocity can be optimised.

- Optimisation of the design has shown that a kinked tendon profile is beneficial in case of large spans. However, high local loads are introduced at the kinks. Therefore a solution is required for distributing these stresses, for example by integrating an additional rib. Additionally, the benefit of a curved tendon profile could be assessed as well as the practical implementation of this solution.

- As the weight of 3DCP structures is typically lower than conventional concrete structures, the structure becomes more sensitive to dynamic discomfort. Therefore, a more detailed dynamic verification analysis should be conducted to assess if these more slender structures meet the design criteria stated in Eurocode.

- Improving and extending the parametric research model by continuously updating it with the rapidly increasing amount of knowledge about 3D concrete printing.

Bibliography

[1] Robbie M Andrew. Global CO 2 emissions from cement production. *Earth Syst. Sci. Data*, 10:195–217, 2018.

[2] A. S.J. Suiker. Mechanical performance of wall structures in 3D printing processes: Theory, design tools and experiments. *International Journal of Mechanical Sciences*, 137:145–170, 3 2018.

[3] R. A. Buswell, W. R. Leal de Silva, S. Z. Jones, and J. Dirrenberger. 3D printing using concrete extrusion: A roadmap for research, 10 2018.

[4] NOS. Wereldprimeur voor Gemert: fietsen over een 3D-geprinte brug | NOS.

[5] Theo A. M. Salet, Zeeshan Y. Ahmed, Freek P. Bos, and Hans L. M. Laagland. Design of a 3D printed concrete bridge by testing. *Virtual and Physical Prototyping*, 13(3):222–236, 7 2018.

[6] BAM Infra. Primeur: Weber Beamix en BAM Infra openen 3D-betonprintfaciliteit, 2019.

[7] Borg Costanzi C. Bos F. Zeeshan A. Wolfs R. Schipper, R. Double curved concrete printing: printing on non-planar surfaces. *Spool*, 4(2):17–21, 2017.

[8] Twente Additive Manufacturing. 3D Printing Concrete Live - World's Records (Time Lapse), 2020.

[9] Freek Bos, Rob Wolfs, Zeeshan Ahmed, and Theo Salet. Additive manufacturing of concrete in construction: potentials and challenges of 3D concrete printing. *Virtual and Physical Prototyping*, 11(3):209–225, 7 2016.

[10] Nicolas Roussel. Rheological requirements for printable concretes, 10 2018.

[11] Cobouw. 3D Betonprinten blijft veel te veel steken in #metoo projecten, klinkt het op de 'eindejaarsroast' van Booosting - Cobouw.nl.

[12] Cobouw. Pioniers van het 3D betonprinten specialiseren zich en zoeken hun eigen niches - Cobouw.nl.

[13] Yu Chen. Sustainable Cemenitious Material for 3D Concrete Printing View project. Technical report.

[14] T. T. Le, S. A. Austin, S. Lim, R. A. Buswell, A. G.F. Gibb, and T. Thorpe. Mix design and fresh properties for high-performance printing concrete. *Materials and Structures/Materiaux et Constructions*, 45(8):1221–1232, 8 2012.

[15] Venkatesh Naidu Nerella, Simone Hempel, and Viktor Mechtcherine. Effects of layer-interface properties on mechanical performance of concrete elements produced by extrusion-based 3D-printing. *Construction and Building Materials*, 205:586–601, 4 2019.

[16] Biranchi Panda, Suvash Chandra Paul, and Ming Jen Tan. Anisotropic mechanical performance of 3D printed fiber reinforced sustainable construction material. *Materials Letters*, 209:146–149, 12 2017.

[17] Suvash Chandra Paul, Yi Wei Daniel Tay, Biranchi Panda, and Ming Jen Tan. Fresh and hardened properties of 3D printable cementitious materials for building and construction. *Archives of Civil and Mechanical Engineering*, 18(1):311–319, 1 2018.

[18] N. Roussel and F. Cussigh. Distinct-layer casting of SCC: The mechanical consequences of thixotropy. *Cement and Concrete Research*, 38(5):624–632, 5 2008.

[19] Jacques Kruger, Stephan Zeranka, and Gideon van Zijl. An ab initio approach for thixotropy characterisation of (nanoparticle-infused) 3D printable concrete. *Construction and Building Materials*, 224:372–386, 11 2019.

[20] A. Perrot, D. Rangeard, and A. Pierre. Structural built-up of cement-based materials used for 3D-printing extrusion techniques. *Materials and Structures/Materiaux et Constructions*, 49(4):1213–1220, 4 2016.

[21] Jacques Kruger, Seung Cho, Stephan Zeranka, Celeste Viljoen, and Gideon van Zijl. 3D concrete printer parameter optimisation for high rate digital construction avoiding plastic collapse. *Composites Part B: Engineering*, 183:107660, 2 2020.

[22] R. J.M. Wolfs, F. P. Bos, and T. A.M. Salet. Early age mechanical behaviour of 3D printed concrete: Numerical modelling and experimental testing. *Cement and Concrete Research*, 106:103–116, 4 2018.

[23] Jacques Kruger, Stephan Zeranka, and Gideon van Zijl. 3D concrete printing: A lower bound analytical model for buildability performance quantification. *Automation in Construction*, 106, 10 2019.

[24] R. J.M. Wolfs, F. P. Bos, and T. A.M. Salet. Triaxial compression testing on early age concrete for numerical analysis of 3D concrete printing. *Cement and Concrete Composites*, 104, 11 2019.

[25] A.S.J. Suiker, R.J.M. Wolfs, S.M. Lucas, and T.A.M. Salet. Elastic buckling and plastic collapse during 3D concrete printing. *Cement and Concrete Research*, 135:106016, 9 2020.

[26] R. J.M. Wolfs, F. P. Bos, and T. A.M. Salet. Correlation between destructive compression tests and non-destructive ultrasonic measurements on early age 3D printed concrete. *Construction and Building Materials*, 181:447–454, 8 2018.

[27] R. J.M. Wolfs and A. S.J. Suiker. Structural failure during extrusion-based 3D printing processes. *International Journal of Advanced Manufacturing Technology*, 104(1-4):565–584, 9 2019.

[28] T. T. Le, S. A. Austin, S. Lim, R. A. Buswell, R. Law, A. G.F. Gibb, and T. Thorpe. Hardened properties of high-performance printing concrete. *Cement and Concrete Research*, 42(3):558–566, 3 2012.

[29] Biranchi Panda, Nisar Ahamed Noor Mohamed, Suvash Chandra Paul, G. V.P.Bhagath Singh, Ming Jen Tan, and Branko Šavija. The effect of material fresh properties and process parameters on buildability and interlayer adhesion of 3D printed concrete. *Materials*, 12(13), 7 2019.

[30] Yi Wei Daniel Tay, Guan Heng Andrew Ting, Ye Qian, Biranchi Panda, Lewei He, and Ming Jen Tan. Time gap effect on bond strength of 3D-printed concrete. *Virtual and Physical Prototyping*, 14(1):104–113, 1 2019.

[31] Jay G. Sanjayan, Behzad Nematollahi, Ming Xia, and Taylor Marchment. Effect of surface moisture on inter-layer strength of 3D printed concrete. *Construction and Building Materials*, 172:468–475, 5 2018.

[32] R. J.M. Wolfs, F. P. Bos, and T. A.M. Salet. Hardened properties of 3D printed concrete: The influence of process parameters on interlayer adhesion. *Cement and Concrete Research*, 119:132–140, 5 2019.

[33] Emmanuel Keita, Hela Bessaies-Bey, Wenqiang Zuo, Patrick Belin, and Nicolas Roussel. Weak bond strength between successive layers in extrusion-based additive manufacturing: measurement and physical origin. *Cement and Concrete Research*, 123:105787, 9 2019.

[34] Timothy Wangler, Nicolas Roussel, Freek P. Bos, Theo A.M. Salet, and Robert J. Flatt. Digital Concrete: A Review, 9 2019.

[35] R. J. M. Wolfs. *Experimental characterization and numerical modelling of 3D printed concrete*. PhD thesis, 2019.

[36] Domenico Asprone, Costantino Menna, Freek P. Bos, Theo A.M. Salet, Jaime Mata-Falcón, and Walter Kaufmann. Rethinking reinforcement for digital fabrication with concrete, 10 2018.

[37] Freek Bos, Zeeshan Ahmed, Evgeniy Jutinov, and Theo Salet. Experimental Exploration of Metal Cable as Reinforcement in 3D Printed Concrete. *Materials*, 10(11):1314, 11 2017.

[38] F. P. Bos, E. Bosco, and T. A. M. Salet. Ductility of 3D printed concrete reinforced with short straight steel fibers. *Virtual and Physical Prototyping*, 14(2):160–174, 4 2019.

[39] P Kumar Mehta and Paulo J M Monteiro. CONCRETE Microstructure, Properties and Materials. Technical report, 2001.

[40] Braam; van Breugel; van der; Walraven Veen;. *Concrete Structures under Imposed Thermal and Shrinkage Deformations - Theory and Practice.* 2011.

[41] Indra Noer Hamdhan and Barry G Clarke. Determination of Thermal Conductivity of Coarse and Fine Sand Soils. Technical report, 2010.

[42] Innovation Origins. TU/e maakt brug van 3D geprint gewapend beton.

[43] Bridge Project. Bridge Project – Een vormvrije betonnen 3D geprinte brug.

[44] European Committee for Standardization. *NEN-EN 1990+A1+A1/C2. Eurocode: Basis of structural design.* 2002.

[45] European Committee for Standardization. *NEN-EN 1991-2+C1. Eurocode 1: Actions on structures - Part 2: Traffic loads on bridges.* 2015.

[46] European Committee for Standardization. *NEN-EN 1992-1-1+C2. Eurocode 2: Design of concrete structures - Part 1-1: General rules and rules for buildings.* 2011.

[47] European Committee for Standardization. NEN-EN 1992-2+C1. Eurocode 2: Design of concrete structures - Concrete bridges - Design and detailing rules. 2011.

[48] Timothy Wangler, Ena Lloret, Lex Reiter, Norman Hack, Fabio Gramazio, Matthias Kohler, Mathias Bernhard, Benjamin Dillenburger, Jonas Buchli, Nicolas Roussel, and Robert Flatt. Digital Concrete: Opportunities and Challenges. *RILEM Technical Letters*, 1:67, 10 2016.

[49] Mingxu Chen, Bo Liu, Laibo Li, Lidong Cao, Yongbo Huang, Shoude Wang, Piqi Zhao, Lingchao Lu, and Xin Cheng. Rheological parameters, thixotropy and creep of 3D-printed calcium sulfoaluminate cement composites modified by bentonite. *Composites Part B: Engineering*, 186, 4 2020.

[50] Ali Kazemian, Xiao Yuan, Evan Cochran, and Behrokh Khoshnevis. Cementitious materials for construction-scale 3D printing: Laboratory testing of fresh printing mixture. *Construction and Building Materials*, 145:639–647, 8 2017.

[51] Gregor Wernet, Christian Bauer, Bernhard Steubing, Jürgen Reinhard, Emilia Moreno-Ruiz, and Bo Weidema. The ecoinvent database version 3 (part I): overview and methodology. *International Journal of Life Cycle Assessment*, 21(9):1218–1230, 9 2016.

[52] Andrea Saltelli. Sensitivity Analysis for Importance Assessment. *Risk Analysis*, 22(3):579–590, 6 2002.

[53] Ilya M Sobol. Sensitivity estimates for nonlinear mathematical models. 1993.

[54] Jon Herman and Will Usher. SALib: An open-source Python library for Sensitivity Analysis.

[55] Douglass J. Wilde Panos Y. Papalambros. *Principles of Optimal Design: Modeling and Computation.* 2000.

List of Figures

List of Tables

Appendices

A

Parameter overview

Parameter overview

Printer (process) properties
- Velocity printer head
- Printer area dimensions
- Pump pressure
- Imperfections
- Nozzle dimensions | *layer width* / *layer height*
- Relative humidity printing location
- Temperature printing location
- Wind speed at printing location
- Curing method
- Inclusion of steel wire?
- Nozzle stand-off distance

Time dependent deformations
- Shrinkage
- Creep

Concrete mix
- Water/binder-ratio
- Binder composition
- Cement/sand-ratio
- Admixtures
- Fiber reinforcement?

Fresh material properties
- Density
- Poisson's ratio
- Compressive strength (t)
- Shear strength (t)
- Young's Modulus (t)

Fresh concrete checks
- No clogging in hose
- Plastic collapse structure
- Elastic buckling structure
- Shape stability of one layer
- Surface cracking
- Interlayer bond
- Filament quality in corner
- Cracking of young concrete

Structural design
- Consequence Class (CC)
- Dimensions structure
- Structural system
- Structural model
- Nr. of elements
- Building sequence

Practical limitations
- Transport: maximum element size
- Geometry: sufficient height for prestressing

Geometry cro-sec
- Length
- Width
- Height
- Web width (~ layer width)
- Nr. of webs

Loads
- Self-weight
- Permanent load
- Distributed variable load
- Local wheel load
- Wind load
- Prestress
- Temperature

Hardened concrete structure ULS
- Tensile stress < f_ctd (no cracks allowed)
- Shear force: V_Ed < V_Rd
- Compressive stress < f_cd

Hardened material properties
- Density
- Poisson's ratio
- Compressive strength (t)
- Tensile strength (t)
- Young's Modulus (t)

Hardened concrete structure SLS
- No tension in SLS
- Limited deflections
- Dynamics check
- Control of crack development

B

LCA calculation

[kg/m3]	Paul et al., 2018		Kazemian et al., 2017	
	geopolymer	OPC+geo	fibre-reinf	OPC
cement	0	290	289	600
slag	39	0	0	0
fly ash	645	278	277	0
silica fume	78	145	145	0
sand	1168	1211	1209	1379
water	47	285	284	259
actigel	8	0	0	0
bentonite	8	0	0	0
K2SIO3	250	0	0	0
KOH	23	0	0	0
sodium lignosulfonate	0	7	9	0
glass fiber	0	0	13.5	0
tot kg/m3	2266	2216	2226.5	2238
	€ 44.07	€ 16.08	€ 17.55	€ 32.39

total concrete volume: 1 m3

LCA database	monetary value [€]	0.16	0.05	30	0.09	0.03	0.0001	0.06	2	4	9
	impact category	Abiotic depletion (no	Global warming	Ozone layer depletion (ODP	Human toxicity	Fresh water aquatic ecot	Marine aquatic	Terrestrial ec	Photochemical o	Acidification	Eutrophication
ingredients	[kg]	kg Sb eq	kg CO2 eq	kg CFC-11 eq	kg 1,4-DB eq	kg 1,4-DB eq	kg 1,4-DB eq	kg 1,4-DB eq	kg C2H4	kg SO2 eq	kg PO4--- eq
cement CEM1	1	0.001575041	0.821865169	2.28998E-08	0.045432377	0.005218558	10.54551544	0.00121037	4.3604E-05	0.001144272	0.000171022
slag GGBFS	1	0.003152425	0.450524188	4.34278E-08	0.216320641	0.009989834	37.56844254	0.00065609	7.05798E-05	0.002591386	0.000539511
fly ash	1	2.30009E-05	0.0033	2.6E-10	0.00067	0.00021	0.21	0.0000074	0.0000012	0.000015	0.0000035
silica fume	1	4.8E-09	0.0052	3.9E-10	0.0015	0.00003	0.32	0.000048	0.0000016	0.000014	0.0000033
river sand	1	2.00013E-05	0.0029	3.1E-10	0.0019	0.000031	0.2	0.000011	0.0000023	0.000018	0.0000042
water	1	2.6E-10	0.00034	1.6E-11	0.000083	0.0000013	0.022	0.0000015	0.00000011	0.0000008	0.00000014
sodium silicate	1	0.0064817	1.15	6.25E-08	0.595	0.00805	37.7	0.00193	0.000411	0.00629	0.00083
glass	1	6.72E-03	6.66E-01	9.03E-08	2.34E-01	4.71E-02	1.12E+02	2.21E-03	3.32E-04	9.38E-03	7.40E-04

OPC	impact category	Abiotic depletion (non fuel)	Global warming (GWP100)	Ozone layer depletion (ODP)	Human toxicity	Fresh water aquatic ecotox.	Marine aquatic ecotoxicity	Terrestrial ecotoxicity	Photochemical oxidation	Acidification	Eutrophication		
ingredients	[kg]	kg Sb eq	kg CO2 eq	kg CFC-11 eq	kg 1,4-DB eq	kg 1,4-DB eq	kg 1,4-DB eq	kg 1,4-DB eq	kg C2H4	kg SO2 eq	kg PO4--- eq	€	€/m3
cement CEM1	600	€ 0.15	€ 24.66	€ 0.00	€ 2.45	€ 0.09	€ 0.63	€ 0.04	€ 0.05	€ 2.75	€ 0.92	€ 31.75	€ 31.75
slag GGBFS	0	€ 0.00	€ 0.00	€ 0.00	€ 0.00	€ 0.00	€ 0.00	€ 0.00	€ 0.00	€ 0.00	€ 0.00	€ 0.00	€ 0.00
fly ash	0	€ 0.00	€ 0.00	€ 0.00	€ 0.00	€ 0.00	€ 0.00	€ 0.00	€ 0.00	€ 0.00	€ 0.00	€ 0.00	€ 0.00
silica fume	0	€ 0.00	€ 0.00	€ 0.00	€ 0.00	€ 0.00	€ 0.00	€ 0.00	€ 0.00	€ 0.00	€ 0.00	€ 0.00	€ 0.00
river sand	1379	€ 0.00	€ 0.20	€ 0.00	€ 0.24	€ 0.00	€ 0.03	€ 0.00	€ 0.01	€ 0.10	€ 0.05	€ 0.63	€ 0.63
water	259	€ 0.00	€ 0.00	€ 0.00	€ 0.00	€ 0.00	€ 0.00	€ 0.00	€ 0.00	€ 0.00	€ 0.00	€ 0.01	€ 0.01
actigel	0												
bentonite	0												
K2SIO3	0	€ 0.00	€ 0.00	€ 0.00	€ 0.00	€ 0.00	€ 0.00	€ 0.00	€ 0.00	€ 0.00	€ 0.00	€ 0.00	€ 0.00
KOH	0	€ 0.00	€ 0.00	€ 0.00	€ 0.00	€ 0.00	€ 0.00	€ 0.00	€ 0.00	€ 0.00	€ 0.00	€ 0.00	€ 0.00
sodium lignosulfonate	0												
glass fiber	0												
		€ 0.16	€ 24.86	€ 0.00	€ 2.69	€ 0.10	€ 0.66	€ 0.04	€ 0.06	€ 2.85	€ 0.98	€ 32.39	€ 32.39

OPC+pozz mixture	impact category	Abiotic depletion (non fuel)	Global warming (GWP100)	Ozone layer depletion (ODP)	Human toxicity	Fresh water aquatic ecotox.	Marine aquatic ecotoxicity	Terrestrial ecotoxicity	Photochemical oxidation	Acidification	Eutrophication		
ingredients	[kg]	kg Sb eq	kg CO2 eq	kg CFC-11 eq	kg 1,4-DB eq	kg 1,4-DB eq	kg 1,4-DB eq	kg 1,4-DB eq	kg C2H4	kg SO2 eq	kg PO4--- eq	€	€/m3
cement CEM1	290	€ 0.07	€ 11.92	€ 0.00	€ 1.19	€ 0.05	€ 0.31	€ 0.02	€ 0.03	€ 1.33	€ 0.45	€ 15.35	€ 15.35
slag GGBFS	0	€ 0.00	€ 0.00	€ 0.00	€ 0.00	€ 0.00	€ 0.00	€ 0.00	€ 0.00	€ 0.00	€ 0.00	€ 0.00	€ 0.00
fly ash	278	€ 0.00	€ 0.05	€ 0.00	€ 0.02	€ 0.00	€ 0.01	€ 0.00	€ 0.00	€ 0.02	€ 0.01	€ 0.10	€ 0.10
silica fume	145	€ 0.00	€ 0.04	€ 0.00	€ 0.02	€ 0.00	€ 0.00	€ 0.00	€ 0.00	€ 0.01	€ 0.00	€ 0.08	€ 0.08
river sand	1211	€ 0.00	€ 0.18	€ 0.00	€ 0.21	€ 0.00	€ 0.02	€ 0.00	€ 0.01	€ 0.09	€ 0.05	€ 0.55	€ 0.55
water	285	€ 0.00	€ 0.00	€ 0.00	€ 0.00	€ 0.00	€ 0.00	€ 0.00	€ 0.00	€ 0.00	€ 0.00	€ 0.01	€ 0.01
actigel	0												
bentonite	0												
K2SIO3	0	€ 0.00	€ 0.00	€ 0.00	€ 0.00	€ 0.00	€ 0.00	€ 0.00	€ 0.00	€ 0.00	€ 0.00	€ 0.00	€ 0.00
KOH	0	€ 0.00	€ 0.00	€ 0.00	€ 0.00	€ 0.00	€ 0.00	€ 0.00	€ 0.00	€ 0.00	€ 0.00	€ 0.00	€ 0.00
sodium lignosulfonate	7												
glass fiber	0												
		€ 0.08	€ 12.18	€ 0.00	€ 1.43	€ 0.05	€ 0.34	€ 0.02	€ 0.03	€ 1.44	€ 0.51	€ 16.08	€ 16.08

geopolymer

| ingredients	[kg]	Abiotic depletion (non fuel) kg Sb eq	Global warming (GWP100) kg CO2 eq	Ozone layer depletion (ODP) kg CFC-11 eq	Human toxicity kg 1,4-DB eq	Fresh water aquatic ecotox. kg 1,4-DB eq	Marine aquatic ecotoxicity kg 1,4-DB eq	Terrestrial ecotoxicity kg 1,4-DB eq	Photochemical oxidation kg C2H4	Acidification kg SO2 eq	Eutrophication kg PO4--- eq	€	€/m3
cement CEM1	0	€ 0.00	€ 0.00	€ 0.00	€ 0.00	€ 0.00	€ 0.00	€ 0.00	€ 0.00	€ 0.00	€ 0.00	€ 0.00	€ 0.00
slag GGBFS	39	€ 0.02	€ 0.88	€ 0.00	€ 0.76	€ 0.01	€ 0.15	€ 0.00	€ 0.01	€ 0.40	€ 0.19	€ 2.42	€ 2.42
fly ash	645	€ 0.00	€ 0.11	€ 0.00	€ 0.04	€ 0.00	€ 0.01	€ 0.00	€ 0.00	€ 0.04	€ 0.02	€ 0.22	€ 0.22
silica fume	78	€ 0.00	€ 0.02	€ 0.00	€ 0.01	€ 0.00	€ 0.00	€ 0.00	€ 0.00	€ 0.00	€ 0.00	€ 0.04	€ 0.04
river sand	1168	€ 0.00	€ 0.17	€ 0.00	€ 0.20	€ 0.00	€ 0.02	€ 0.00	€ 0.01	€ 0.08	€ 0.04	€ 0.53	€ 0.53
water	47	€ 0.00	€ 0.00	€ 0.00	€ 0.00	€ 0.00	€ 0.00	€ 0.00	€ 0.00	€ 0.00	€ 0.00	€ 0.00	€ 0.00
actigel	8											€ 0.00	€ 0.00
bentonite	8											€ 0.00	€ 0.00
K2SIO3	250	€ 0.26	€ 14.38	€ 0.00	€ 13.39	€ 0.06	€ 0.94	€ 0.03	€ 0.21	€ 6.29	€ 1.87	€ 37.42	€ 37.42
KOH	23	€ 0.02	€ 1.32	€ 0.00	€ 1.23	€ 0.01	€ 0.09	€ 0.00	€ 0.02	€ 0.58	€ 0.17	€ 3.44	€ 3.44
sodium lignosulfonate	0											€ 0.00	€ 0.00
glass fiber	0											€ 0.00	€ 0.00
		€ 0.31	€ 16.87	€ 0.00	€ 15.63	€ 0.08	€ 1.22	€ 0.03	€ 0.24	€ 7.40	€ 2.30	€ 44.07	€ 44.07

fiber-reinforced

ingredients	[kg]	Abiotic depletion (non fuel) kg Sb eq	Global warming (GWP100) kg CO2 eq	Ozone layer depletion (ODP) kg CFC-11 eq	Human toxicity kg 1,4-DB eq	Fresh water aquatic ecotox. kg 1,4-DB eq	Marine aquatic ecotoxicity kg 1,4-DB eq	Terrestrial ecotoxicity kg 1,4-DB eq	Photochemical oxidation kg C2H4	Acidification kg SO2 eq	Eutrophication kg PO4--- eq	€	€/m3
cement CEM1	289	€ 0.07	€ 11.88	€ 0.00	€ 1.18	€ 0.05	€ 0.30	€ 0.02	€ 0.03	€ 1.32	€ 0.44	€ 15.29	€ 15.29
slag GGBFS	0	€ 0.00	€ 0.00	€ 0.00	€ 0.00	€ 0.00	€ 0.00	€ 0.00	€ 0.00	€ 0.00	€ 0.00	€ 0.00	€ 0.00
fly ash	277	€ 0.00	€ 0.05	€ 0.00	€ 0.02	€ 0.00	€ 0.01	€ 0.00	€ 0.00	€ 0.02	€ 0.01	€ 0.10	€ 0.10
silica fume	145	€ 0.00	€ 0.04	€ 0.00	€ 0.02	€ 0.00	€ 0.00	€ 0.00	€ 0.00	€ 0.01	€ 0.00	€ 0.08	€ 0.08
river sand	1209	€ 0.00	€ 0.18	€ 0.00	€ 0.21	€ 0.00	€ 0.02	€ 0.00	€ 0.01	€ 0.09	€ 0.05	€ 0.55	€ 0.55
water	284	€ 0.00	€ 0.00	€ 0.00	€ 0.00	€ 0.00	€ 0.00	€ 0.00	€ 0.00	€ 0.00	€ 0.00	€ 0.01	€ 0.01
actigel	0											€ 0.00	€ 0.00
bentonite	0											€ 0.00	€ 0.00
K2SIO3	0	€ 0.00	€ 0.00	€ 0.00	€ 0.00	€ 0.00	€ 0.00	€ 0.00	€ 0.00	€ 0.00	€ 0.00	€ 0.00	€ 0.00
KOH	0	€ 0.00	€ 0.00	€ 0.00	€ 0.00	€ 0.00	€ 0.00	€ 0.00	€ 0.00	€ 0.00	€ 0.00	€ 0.00	€ 0.00
sodium lignosulfonate	9											€ 0.00	€ 0.00
glass fiber	13.5	€ 0.01	€ 0.45	€ 0.00	€ 0.28	€ 0.02	€ 0.15	€ 0.00	€ 0.01	€ 0.51	€ 0.09	€ 1.53	€ 1.53
		€ 0.09	€ 12.59	€ 0.00	€ 1.71	€ 0.07	€ 0.49	€ 0.02	€ 0.04	€ 1.94	€ 0.59	€ 17.55	€ 17.55

prestress

		Abiotic depletion (non fuel) kg Sb eq	Global warming (GWP100) kg CO2 eq	Ozone layer depletion (ODP) kg CFC-11 eq	Human toxicity kg 1,4-DB eq	Fresh water aquatic ecotox. kg 1,4-DB eq	Marine aquatic ecotoxicity kg 1,4-DB eq	Terrestrial ecotoxicity kg 1,4-DB eq	Photochemical oxidation kg C2H4	Acidification kg SO2 eq	Eutrophication kg PO4--- eq	€
		0.16	0.05	30	0.09	0.03	0.0001	0.06	2	4	9	
ingredients	[kg]											
Prestressing steel (average)	kg	1.54E-02	1.79E+00	7.17E-08	3.81E+00	1.49E+00	1.32E+03	3.18E-02	9.27E-04	7.38E-03	1.34E-03	
		€ 0.00	€ 0.09	€ 0.00	€ 0.34	€ 0.04	€ 0.13	€ 0.00	€ 0.00	€ 0.03	€ 0.01	€ 0.66
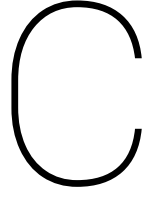
Elaboration on structural analyses

C.1. Hardened concrete structure

C.1.1. Calculation of imposed deformations

Creep strain

The creep deformation under a sustained compression stress σ_c can be calculated according to NEN-EN 1992-1-1 as follows:

$$\epsilon_{cc}(t, t_0) = \phi(t, t_0)\sigma_c / E_c \tag{C.1}$$

where $\phi(\infty, t_0)$ is the creep coefficient according to

$$\phi(t, t_0) = \phi_0 \beta_c(t, t_0). \tag{C.2}$$

t_0 is the concrete age at loading [days] and t the concrete age that is considered. The notional creep coefficient may be estimated from

$$\phi_0 = \phi_{RH}\beta(f_{cm})\beta(t_0) \tag{C.3}$$

with

$$\phi_{RH} = \left[1 + \frac{1 - RH/100}{0.1h^{1/3}}\alpha_1\right]\alpha_2 \tag{C.4}$$

$$\beta(f_{cm}) = \frac{16.8}{\sqrt{f_{cm}}} \tag{C.5}$$

$$\beta(t_0) = \frac{1}{0.1 + (t_0)^{0.2}} \tag{C.6}$$

where f_{cm} is the mean compressive strength at 28 days in [MPa], h is the notional size equal to $2A_c/u$ [mm], $\alpha_1 = (35/f_{cm})^{0.7}$ and $\alpha_2 = (35/f_{cm})^{0.2}$. The development of creep in time is described by:

$$\beta_c(t, t_0) = \left[\frac{(t - t_0)}{\beta_H + (t - t_0)}\right]^{0.3} \tag{C.7}$$

with

$$\beta_H = 1.5h\left[1 + (1.2RH/100)^{18}\right] + 250\alpha_3 \leq 1500\alpha_3 \tag{C.8}$$

where $\alpha_3 = (35/f_{cm})^{0.5}$. If the compressive stress σ_c exceeds $0.45f_{ck}(t_0)$, non-linear creep must be accounted for:

$$\phi_{nl}(\infty, t_0) = \phi(\infty, t_0)\exp(1.5(k_\sigma - 0.45)) \tag{C.9}$$

where $k_\sigma = \sigma_c / f_{ck}(t_0)$.

Shrinkage strain

The total shrinkage strain can be calculated according to the Model Code 2010 as follows:

$$\epsilon_{cs}(t, t_s) = \epsilon_{cas}(t) + \epsilon cds(t, t_s), \tag{C.10}$$

where the autogeneous shrinkage $\epsilon_{cas}(t)$ is equal to

$$\epsilon_{cas}(t) = \epsilon_{cas0}(f_{cm})\beta_{as}(t) \tag{C.11}$$

and the drying shrinkage $\epsilon_{cds}(t, t_s)$ is equal to

$$\epsilon_{cds}(t, t_s) = \epsilon_{cds0}(f_{cm}) \cdot \beta_{RH}(RH) \cdot \beta_{ds}(t - t_s) \tag{C.12}$$

where t is the concrete age in [days], t_s is the concrete age at the beginning of drying in [days] and $(t - t_s)$ is the duration of drying.

The notional autogeneous component can be calculated as follows:

$$\epsilon_{cas0}(f_{cm}) = -\alpha_{as}\left(\frac{f_{cm}/10}{6 + f_{cm}/10}\right)^{2.5} \cdot 10^{-6} \tag{C.13}$$

and

$$\beta_{as}(t) = 1 - exp(-0.2\sqrt{t}) \tag{C.14}$$

where f_{cm} is the mean compressive strength at t=28 days and $\alpha_{as} = 600$ for cement strength class 52.5R.

The drying shrinkage can be calculated as follows:

$$\epsilon_{cds}(t, t_s) = \epsilon_{cds0}(f_{cm}) \cdot \beta_{RH}(RH) \cdot \beta_{ds}(t - t_s) \tag{C.15}$$

where

- t is the concrete age in [days]

- t_s is the concrete age at the beginning of drying

The notional drying shrinkage coefficient $\epsilon_{cds}(f_{cm})$, the coefficient $\beta_{RH}(RH)$ taking into account the effect of the ambient RH and the coefficient $\beta_{ds}(t - t_s)$ describing the time-development are computed using:

$$\epsilon_{cds0}(f_{cm}) = \left[(220 + 110\alpha_{ds1})\exp(-\alpha_{ds2}f_{cm})\right] \cdot 10^{-6} \tag{C.16a}$$

$$\beta_{RH} = -1.55\left[1 - \left(\frac{RH}{100}\right)^3\right] \text{ for } 40 \le RH < 99\%\beta_{s1} \tag{C.16ba}$$

$$\beta_{RH} = 0.25 \text{ for } RH \ge 99\%\beta_{s1} \tag{C.16bb}$$

$$\beta_{ds}(t - t_s) = \left(\frac{(t - t_s)}{0.035h^2 + (t - t_s)}\right)^{0.5} \tag{C.16c}$$

$$\beta_{s1} = \left(\frac{35}{f_{cm}}\right)^{0.1} \tag{C.16d}$$

where

- $\alpha_{ds1} = 6$ and $\alpha_{ds2} = 0.012$ (cement type 52.5R);

- f_{cm} is the mean compressive strength;

- RH is the relative humidity of the environment [%];

- $h = 2A_c/u$ is the notional thickness of the element in contact with the atmosphere.

C.1.2. SLS checks

Prestress limit to prevent concrete crushing

First of all, the compressive stress in SLS induced by prestressing at t=0 must be limited to prevent concrete crushing:

$$UC_{0.6f_{ck}} = \frac{P_{m0}}{A_c}/0.6f_{ck} \leq 1.0 \tag{C.1}$$

Deformation limit

Assuming a simply-supported beam (which is conservative since the presence of the anchor-blocks provide some rotational stiffness), the deformation at mid-span of the bridge can be calculated as follows:

$$w = \frac{\frac{5}{384}(qL^4) - \frac{1}{8}(M_P L^2)}{E_{c,eff}I}; \tag{C.2}$$

where q is the load acting on the structure (calculated using eq. (3.4)), L is the span length, I is the moment of inertia and E is the effective modulus of elasticity given by:

$$E_{c,eff} = \frac{E_{cm}}{1 + \phi(\infty, t_0)} \tag{C.3}$$

where $\phi(\infty, t_0)$ is the creep coefficient at $t = \infty$. The deformation check can be calculated using:

$$UC_w = w/w_{max} \tag{C.4}$$

Determining required amount of prestress

As long as the structure is uncracked, the resulting stresses can be calculated as a superposition of the contributions depicted in fig. C.1.
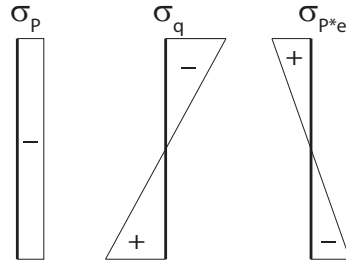

Figure C.1: Resulting normal stresses at mid-span, bottom fiber level

Using this relation, in case of a linear tendon profile, the minimal required amount of prestress to avoid tension in SLS is determined by solving the following inequality:

$$\frac{-P_{m\infty}}{A} - \frac{P_{m\infty}e_p}{W_{bot}} + \frac{M^{SLS}_{q,L/2}}{W_{bot}} \leq 0 \tag{C.5}$$

If this causes tension at the top of the cross-section at support level, the tendon eccentricity e_p is reduced (and the amount of prestress in increased accordingly) until the following inequality is satisfied:

$$-\frac{1.1 \cdot P_{m0}}{A} + \frac{1.1 \cdot P_{m0}e_p}{W_{top}} - \frac{0.9 \cdot M^{SLS}_{sw,sup}}{W_{top}} \leq 0 \tag{C.6}$$

For a kinked tendon profile, the upward bending moment from prestressing can be calculated as:

$$M_P = P_\infty \sin(\frac{e_P}{l_p})l_p \approx P_\infty e_p \tag{C.7}$$

Dynamic verification
Assuming that the bridge can be modelled as a SDoF system without damping, the eigenfrequency of the (simply supported) bridge (loaded by a point-load) can be calculated as follows:

$$\omega_n = \sqrt{\frac{k}{m}} \tag{C.8}$$

with

$$k = \frac{48EI}{L^3}. \tag{C.9}$$

A dynamic validation analysis must be performed is the following check is not fulfilled:

$$UC_\omega = 5/\omega_n \tag{C.10}$$

C.1.3. ULS checks
Shear force limit
The maximum shear force in ULS must be lower than the shear capacity defined by (3.9):

$$UC_V = V_{Ed,sup}^{ULS}/V_{Rd,sup} \le 1.0 \tag{C.11}$$

where $V_{Ed} = \frac{1}{2}qL^2$ and V_{Rd} is calculated using (3.9).

The bending checks at mid-span are dependent on the scenario for joint strength (A) or (B) that is considered.
Bending: scenario (A)
The maximum compressive stress and tensile stress must be lower than the concrete design strength:

$$UC_{f_{cd}} = \sigma_{top,L/2}^{ULS}/f_{cd} \le 1.0 \tag{C.12}$$

$$UC_{f_{ctd}} = \sigma_{bot,L/2}^{ULS}/f_{ctd} \le 1.0 \tag{C.13}$$

where

$$\sigma_{top,L/2}^{ULS} = -\frac{P_{m\infty}}{A} + \frac{P_{m\infty}e_p}{W_{top}} - \frac{M_{q,L/2}^{ULS}}{W_{top}} \tag{C.14a}$$

$$\sigma_{bot,L/2}^{ULS} = -\frac{P_{m\infty}}{A} - \frac{P_{m\infty}e_p}{W_{bot}} + \frac{M_{q,L/2}^{ULS}}{W_{bot}} \tag{C.14b}$$

Bending: scenario (B)
At mid-span after joint opening, sufficient bending moment capacity must be present in ULS. Additionally, it must be checked if the stress in the concrete compression zone and the stress in the prestressing steel are within limits:

$$UC_M = M_{Ed,L/2}/M_{Rd,L/2} \le 1.0 \tag{C.15}$$

$$UC_{\sigma_P} = (\sigma_P + \Delta\sigma_P)/f_{pd} \le 1.0 \tag{C.16}$$

$$UC_{f_{cd}} = \sigma_{top,L/2}^{ULS}/f_{cd} \le 1.0 \tag{C.17}$$

These quantities can be calculated based on the mechanism depicted in fig. C.2. It is assumed that the deflection δ is small and equal to 10 mm. Due to the joint opening, the prestressing force increases and the concrete compression force accordingly.

This force increase can be calculated using:

$$\Delta P = \frac{\Delta L}{L}E_P A_P \tag{C.18}$$

where E_p is the elasticity modulus of prestressing steel equal to 195,000 MPa, A_p the total amount of prestress, and ΔL the elongation of the prestressing steel: $\Delta L = 2\theta(H - \delta - e_{edge})$. Considering the acting cross-sectional forces, depicted in fig. C.3, and making force equilibrium, the horizontal force can be determined: $N_c =$
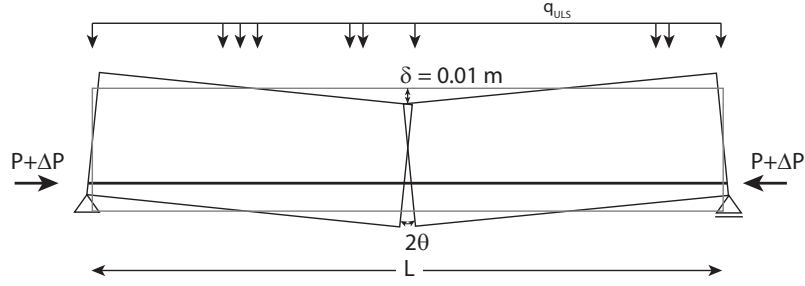
Figure C.2: Developed mechanism after joint opening: two rigid blocks rotated with an angle $\theta = \frac{\delta}{L/2}$

$P + \Delta P$. To determine the stress in the prestressing steel, it is assumed that the ultimate concrete strain is reached, equal to 3.5 ‰. The prestressing steel strain can be calculated using:

$$\epsilon_P = \frac{3.5}{x_u}(H - \delta - e_{edge} - x_u) \tag{C.19}$$

where x_u the height of the compression zone and still unknown. Assuming the stress-strain distribution given in fig. C.4 the actual prestressing steel stress $\sigma_P + \Delta\sigma_P$ and strain can be found. The height of the concrete compression zone can be now determined by solving (C.19). Using this value, the compressed area and corresponding concrete compressive stress $\sigma_{top,L/2}^{ULS}$ can be calculated. Finally, it must be determined where the concrete compression force is acting, given the open cross-section. It is assumed that the force acts at $0.5x_u$ from top-fiber level, which is conservative. The bending moment capacity is then equal to:

$$M_{Rd} = N_c \left(H - 0.5x_u - \delta - e_{edge}\right) \tag{C.20}$$
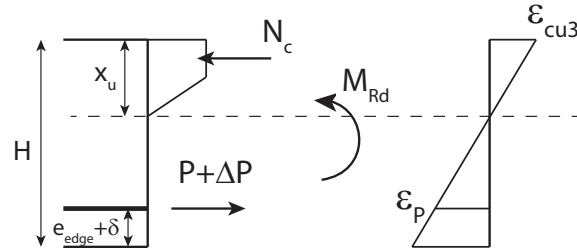
Figure C.3: Cross-sectional forces resulting after joint opening

Stress-strain diagram of prestressing steel
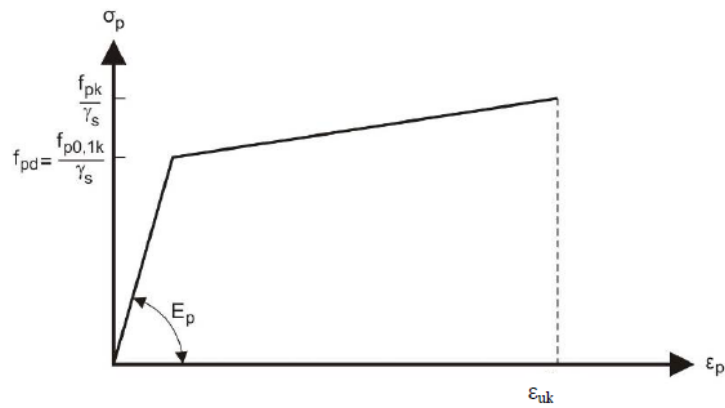
Y1860S7: $f_{pk} / \gamma_s = 1860 / 1{,}1 = 1691$ N/mm^2
            $f_{pd} = f_{p0,1k} / \gamma_s = 1674 / 1{,}1 = 1522$ N/mm^2
            $\varepsilon_{uk} = 35$ ‰
            max. initial stress $\sigma_{pi} = \sigma_{pm0} = 1395$ N/mm^2 ; $\sigma_{p.max} = 1488$ N/mm^2 (at jacking)
            $E_p = 195 \cdot 10^3$ N/mm^2

Figure C.4: Stress-strain diagram of Y1860S7 prestressing steel (from the TUDelft course CIE4160)

D
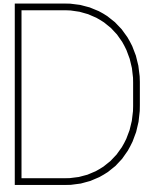
FE Analyses

D.1. FE model assumptions

The 3D-model is constructed as described hereafter. The FE model for the distributed loads is shown in fig. D.1 and the FE model for analysing the effects of the local loads is shown in fig. D.2.

- the anchor blocks are modelled at both sides of the bridges as solid unreinforced concrete (C30/37) elements of width 0.3m;

- the 3DCP material is defined as isotropic concrete with given Young's Modulus and Poisson's ratio;

- linear solid elements are applied for both the concrete anchor blocks and 3DCP structure;

- a mesh size equal to 0.1m is used (double the layer-thickness);

- the prestressing loads are applied as n point loads with a magnitude P/n applied at the anchor blocks.

- line-supports with restrained z-rotation are applied at the bridge-edges (no face-support is applied at the anchor-blocks, otherwise the blocks would act as a rotational constraint which is unconservative);

- loads are applied according to the load-cases specified in table 4.2;

- no symmetry is applied because of the configuration of the prestressing tendons in the anchor blocks on both sides;

- a linear-elastic analysis is sufficient since cracking is not allowed (design requirement);

- for the check on local loads and transverse stress concentrations, the concrete top-layer is modelled as well because it is essential for distributing the local forces. The deck is modelled as a block of 90mm thick made of conventional concrete.

- the service vehicle is applied as 4 wheel loads with a magnitude of $25/2/(0.25^2) = 200 \, \text{kN/m}^2$.
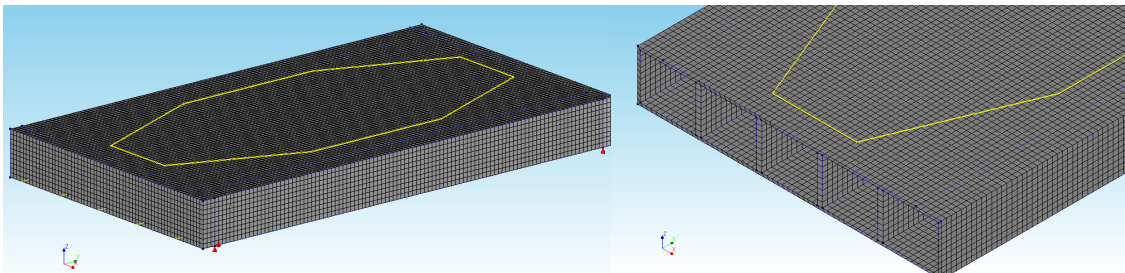

Figure D.1: 3D FE model for analysing validation case 1. The FE model for case 2 and 3 are similar, but have varying span and number of cells. The distributed load and prestressing loads (point loads) are shown in yellow.
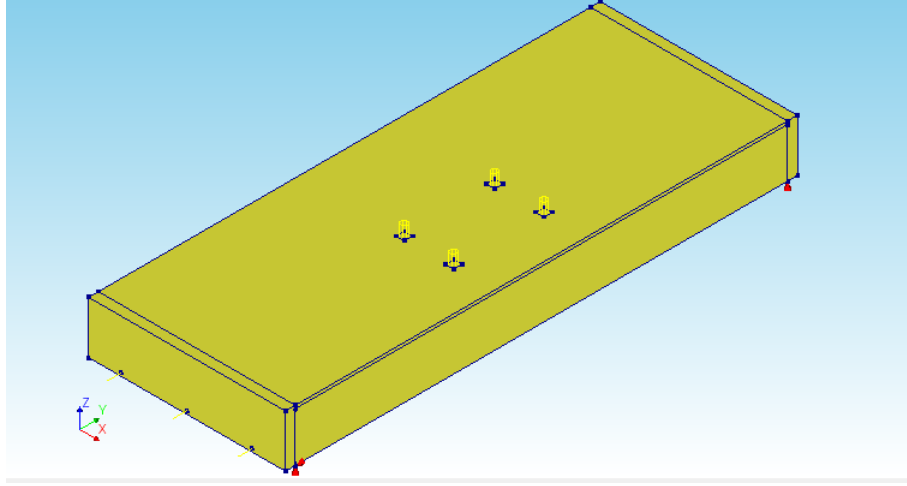
Figure D.2: 3D FEM model for analysing validation case 4, including the top-layer. The loads are shown in yellow.

D.2. Results

Case 1: maximum slenderness

As shown in fig. D.3, the tensile- and compressive stresses in longitudinal direction are, as expected, similar to the 1D results (the small scatter at support-level is due to the presence of the anchor blocks). The 1D beam-model even overestimates the stresses at both top and bottom. This might be due to the small rotational constraint provided by the anchor blocks, which is not captured in the simplified model.
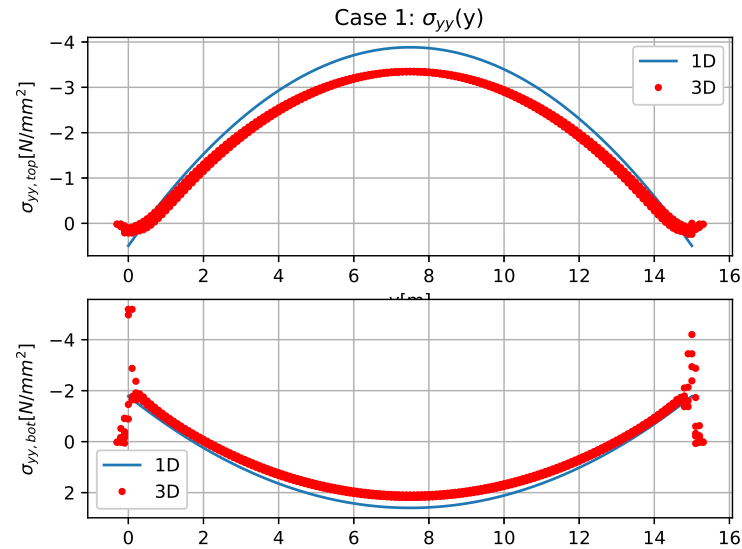
Figure D.3: Case 1: σ_{yy}(y) at the bottom- and top of the beam.

The stresses vary linearly over the height as can be seen in fig. D.4, which means the Bernouilli-hypothesis can be applied. This implies that the assumed minimum slenderness ratio of $L/10$ yields realistic results.
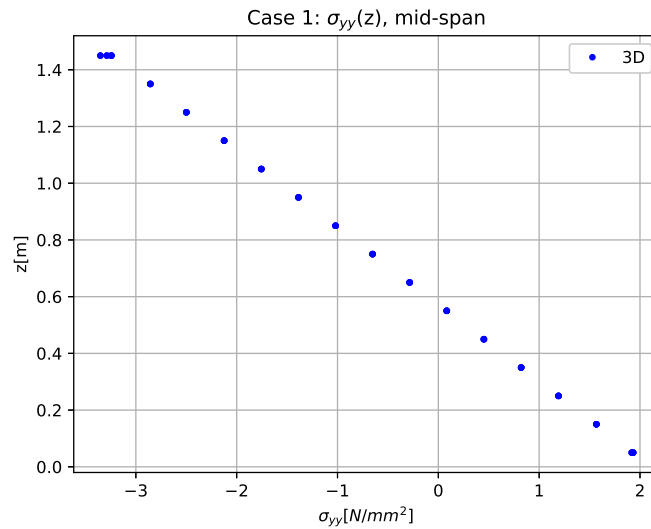
Figure D.4: Case 1: $\sigma_{yy}(z)$, measured at mid-span (z=0 corresponds to the bottom-side).

Case 2: long-span
To verify if the stresses induced for a long-span beam are not underestimated, a bridge design with a 20 meter span is validated. The results are plotted and shown in fig. D.5. It is observed that the simplified beam model becomes even more accurate for this increased span. Therefore, it can be concluded that for long spans, the beam model is a safe approximation.

Figure D.5: Case 2: $\sigma_{yy}(y)$ at the bottom- and top of the beam.

Case 3: transverse stresses
In fig. D.6 it is shown that stresses in lateral direction vary due to the webs present in the deck. For a cross-section with three cells only, the stresses cannot be sufficiently distributed, yielding high tensile peak stresses at the webs at the deck.
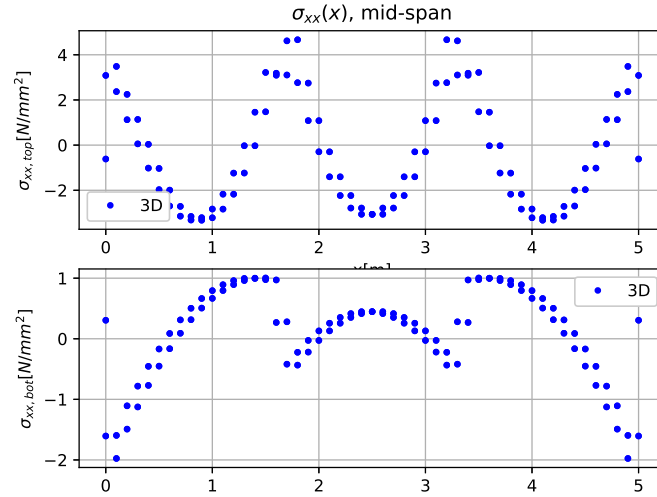
Figure D.6: Case 3: transverse stresses for n = 3, exceeding the tensile strength.

Performing the same analysis, but now including the concrete compression layer yields the result depicted in fig. D.7. Stresses are below the tensile strength which means the 1D simplification does not underestimate possible tensile stresses. Note: at the top, two stress-patterns are plotted. This is because stresses are element results, which are interpolated towards the nodes at the interface between top-layer and 3DCP cross-section.

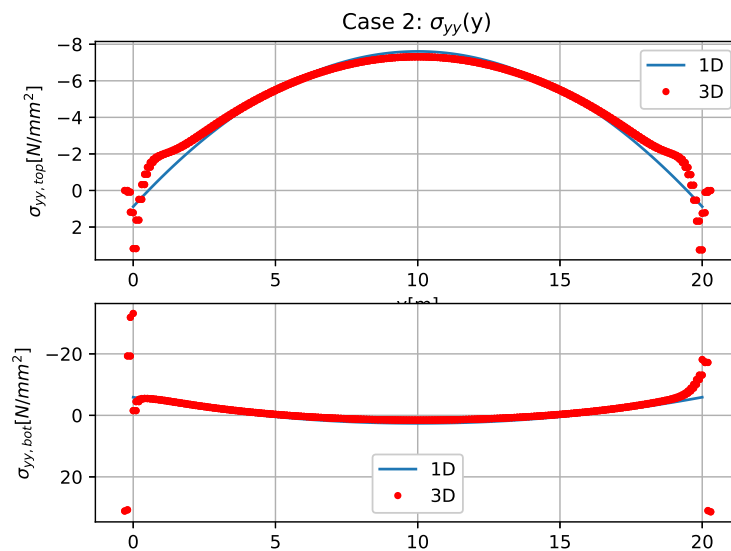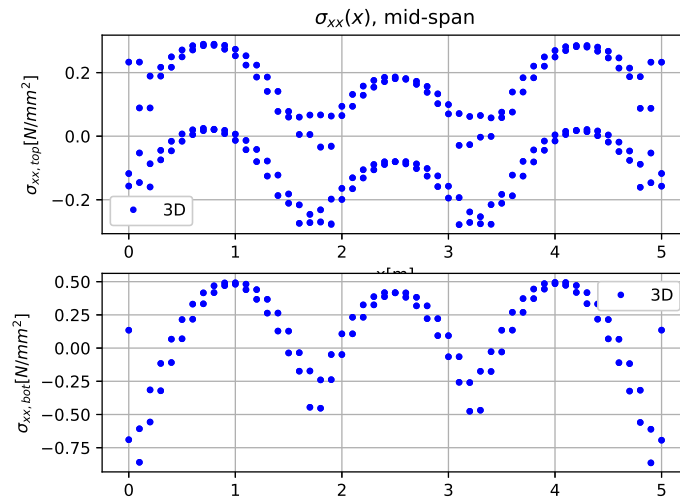Figure D.7: Case 3: transverse stresses for n = 3 including top-layer, not exceeding the tensile strength.

Case 4: service vehicle
The wheel loads are applied as depicted in fig. D.2. The truck is positioned slightly eccentric. For this analysis, the compression-layer is added to the model, to accurately model the stress distribution of the local loads. The global behaviour of the truck is not governing as can be seen in fig. D.8: all stresses remain smaller than f_{ctd}. Moreover, a preliminary analysis has pointed out that for larger spans, the service vehicle cannot exceed the compression from the pretressing, thereby hardly inducing any tension at the bottom. Furthermore, the local behaviour is not inducing any peak stresses as well, as depicted in fig. D.9.
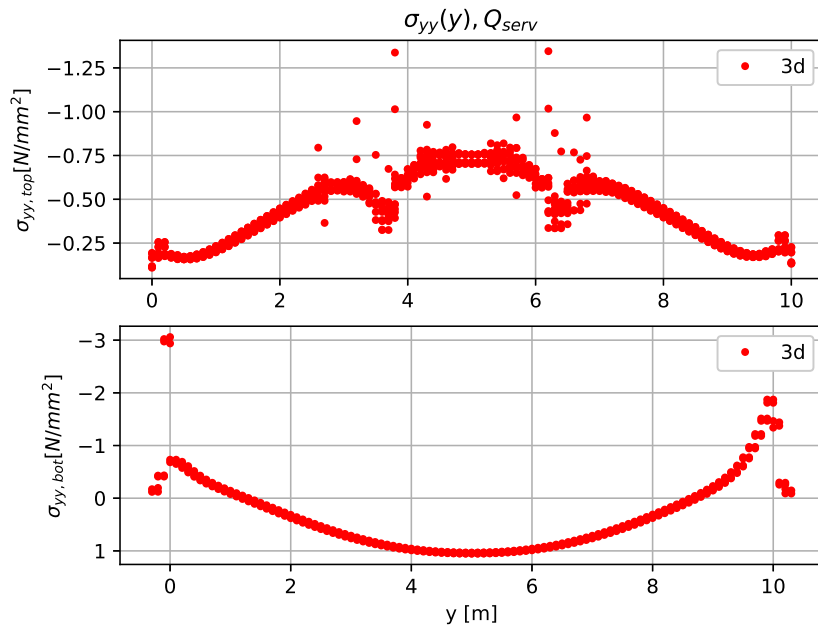
Figure D.8: Case 4: normal stresses σ_{yy} induced by the service vehicle (measured under the most eccentric wheel at x = 4 m).
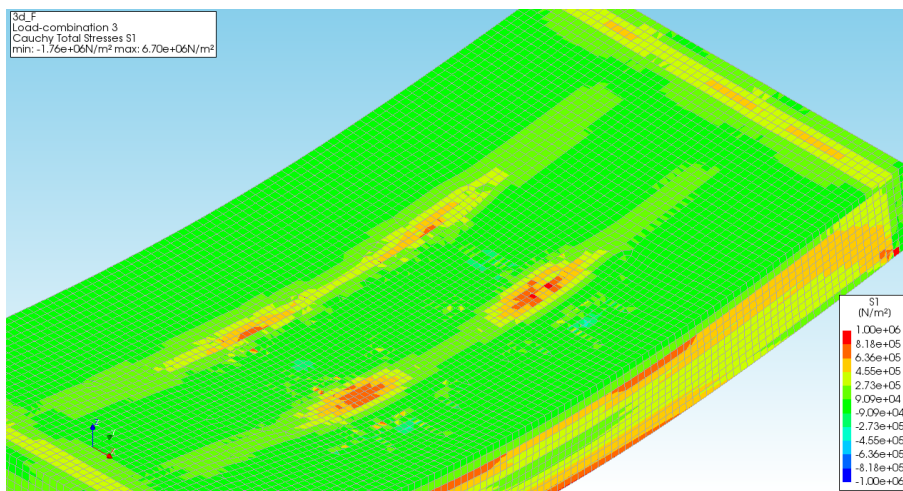
Figure D.9: Case 4: principal stresses under the wheel contact points from the service vehicle.

Results parameter study

E.1. Preliminary study results

E.1.1. Scenario (A): high joint-strength

In this section, the preliminary sensitivity analysis are presented, based on the assumption that the joint strength is higher than the design concrete strength. In table E.1 an overview of the response characteristics is presented. This is important information for the subsequent analyses.

Table E.1: Model characteristics for scenario (B): + = monotonically increasing; - = monotonically decreasing; / = non-monotonic; L = linear; NL = non-linear; 0 = no influence; nc: non-continuous.

|	UC_l	$UC_{f_{ck}}$	UC_ω	UC_w	UC_V	$UC_{f_{ctd}}$	$UC_{f_{cd}}$	P	f_1	f_2
W	NL -	nc +; NL +	NL -	nc +; NL +	L +	0; NL +	nc +; NL +	nc +; NL +	nc +; L +	L +
L	L +	NL +	NL +	NL +	NL +	0; NL +	NL +	NL +	L +	NL +
a	0	NL -; NL +	NL -	NL +; /	NL +; NL -	NL +; 0	NL +	NL -; NL +	NL -	NL -
H	NL -	nc -; NL -	NL -	nc -; NL -	nc -; NL -	NL -; 0	nc -; NL -	nc -; NL -	L +	nc /; /
n	NL -	nc -; NL -	NL +	nc -; NL -	NL -	L -; 0	nc -; NL -	nc +; L +	L +	nc +; L +
b	NL -	nc -; NL -	L +	nc -; NL -	nc -; NL -	NL -; 0	nc -; NL -	nc +; NL -	L +	L +
d	NL +	0	0	0	0	0	0	0	NL -	0
v	L +	0; NL -	0	0; NL +	NL -	NL -; 0	0; NL +	0; NL -	NL -	0; NL -
N	NL -	0	0	0	0	0	0	0	L+	0
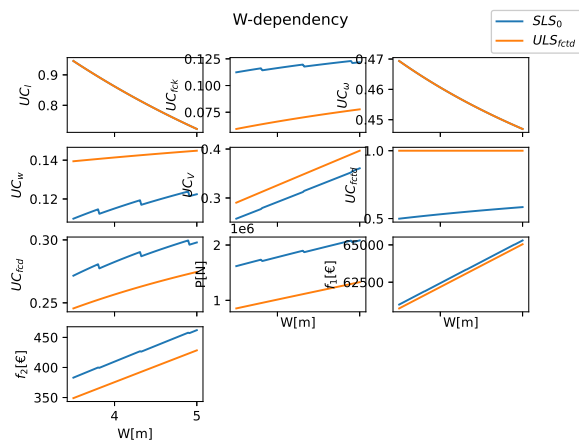
Figure E.1: Scenario (A): W-dependency
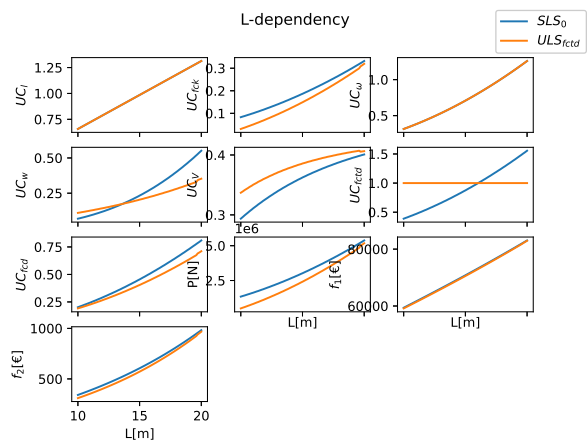
Figure E.2: Scenario (A): L-dependency
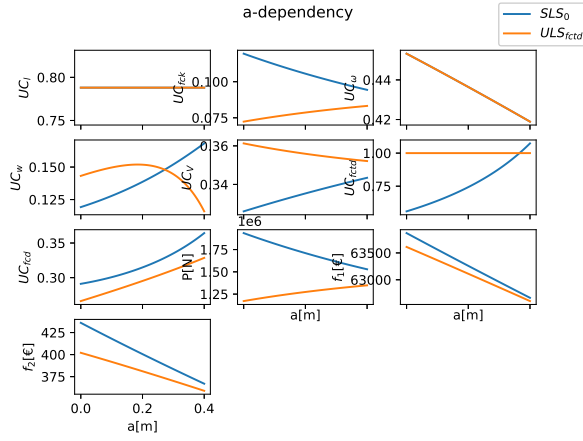
Figure E.3: Scenario (A): a-dependency
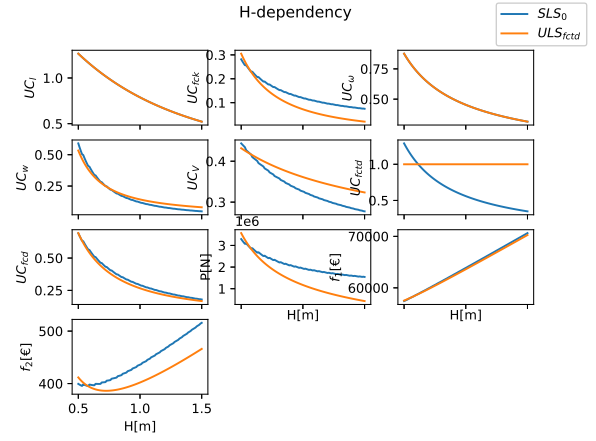
Figure E.4: Scenario (A): H-dependency
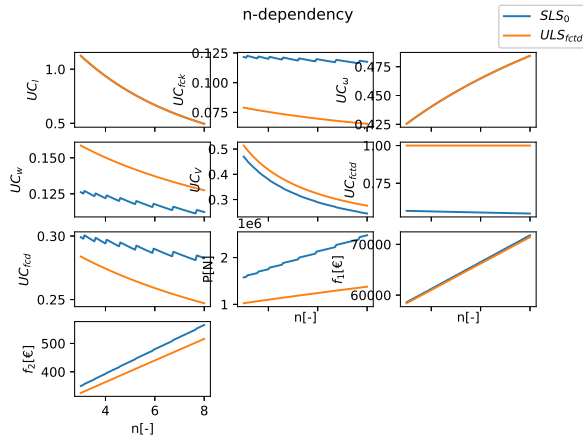
Figure E.5: Scenario (A): n-dependency
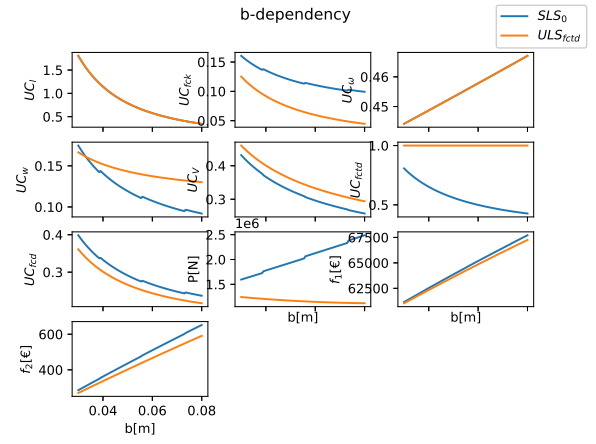
Figure E.6: Scenario (A): b-dependency
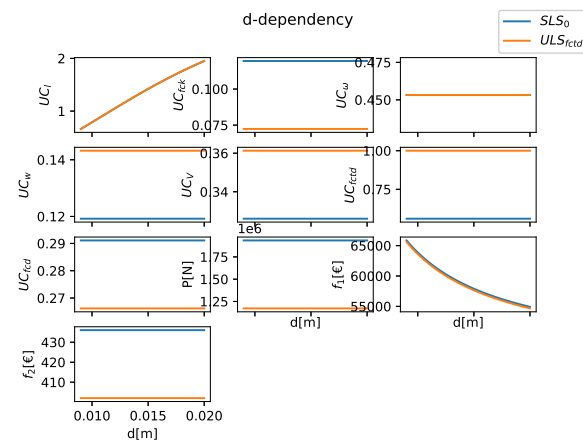
Figure E.7: Scenario (A): d-dependency
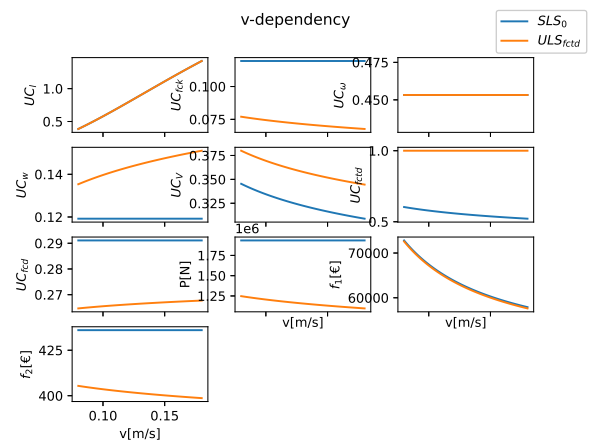
Figure E.8: Scenario (A): v-dependency
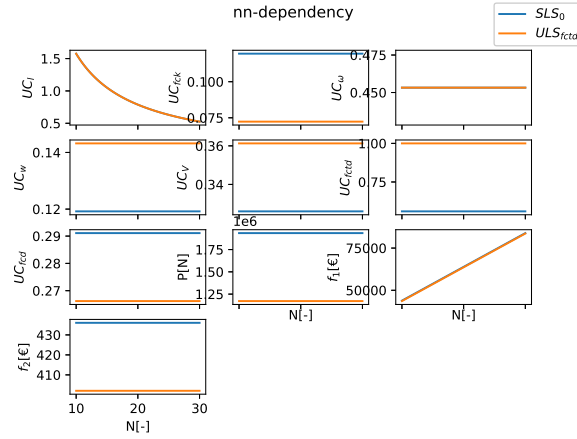
Figure E.9: Scenario (A): N-dependency

E.1.2. Scenario (B): zero joint-strength

In this section, the preliminary sensitivity analysis are presented, based on the assumption that the joint strength is zero. This means that when reaching a tensile stress, the joints will start to open, yielding a kinematic mechanism. In table E.2 an overview of the response characteristics is presented. This is important information for the subsequent analyses.

Table E.2: Model characteristics for scenario (B): + = monotonically increasing; - = monotonically decreasing; / = non-monotonic; L = linear; NL = non-linear; 0 = no influence; nc: non-continuous.

|	UC_l	$UC_{f_{ck}}$	UC_ω	UC_w	UC_V	UC_M	UC_P	$UC_{f_{cd}}$	P	f_1	f_2
W	L -	nc +	NL -	nc +	nc +	nc +	nc +	nc +	L +	nc +	
L	L +	NL +	NL +	NL +	NL +	NL +	NL -	NL +	NL +	L +	NL +
a	0	NL -	NL -	NL +	NL +	NL -	0	NL -	NL -	L -	L -
H	NL -	nc -	NL -	nc -	nc -	nc -	nc +	nc -	nc -	L +	nc /
n	NL -	nc -	NL +	nc -	nc -	nc -	nc -	nc -	nc +	L +	nc +
b	NL -	nc -	L +	nc -	nc -	nc -	nc -	nc -	nc +	L +	L +
d	NL +	0	0	0	0	0	0	0	0	NL -	0
v	L +	0	0	0	NL -	0	0	0	0	NL -	0
N	NL -	0	0	0	0	0	0	0	0	L+	0
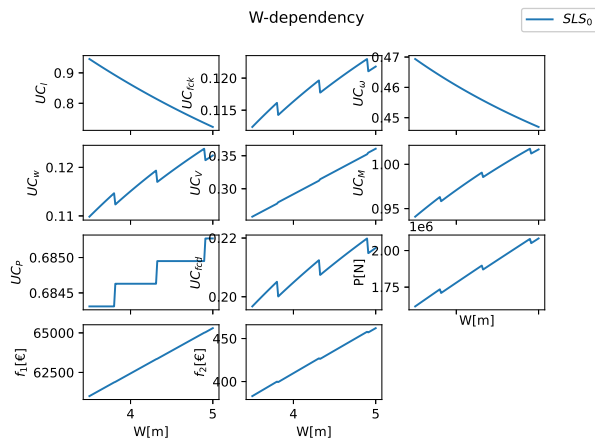
Figure E.10: Scenario (B): W-dependency
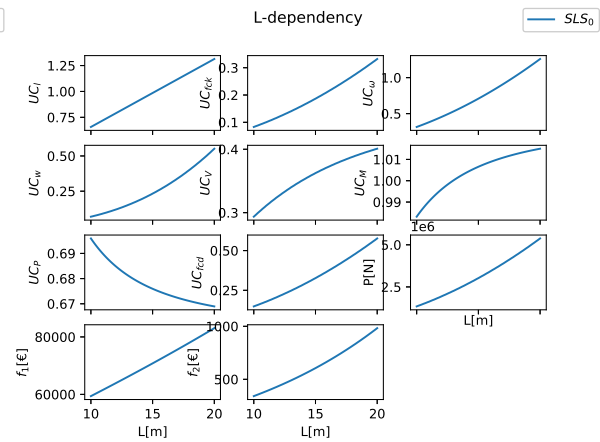
Figure E.11: Scenario (B): L-dependency
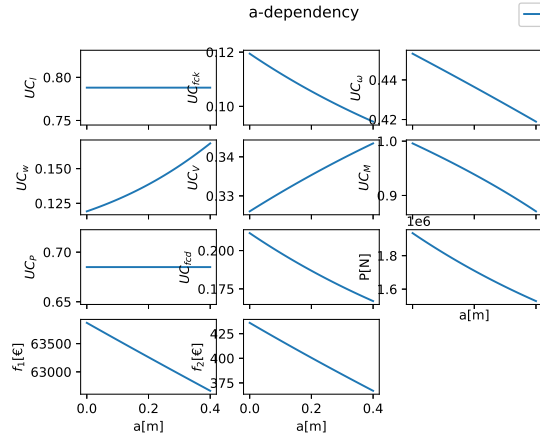
Figure E.12: Scenario (B): a-dependency
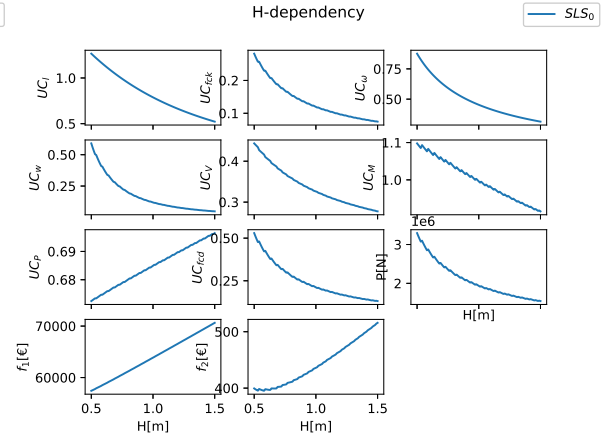
Figure E.13: Scenario (B): H-dependency
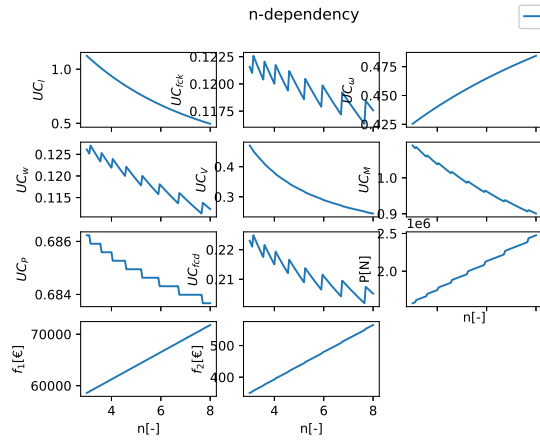
Figure E.14: Scenario (B): n-dependency
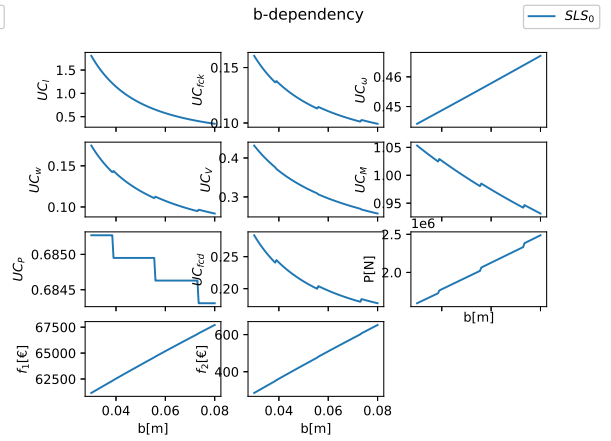
Figure E.15: Scenario (B): b-dependency
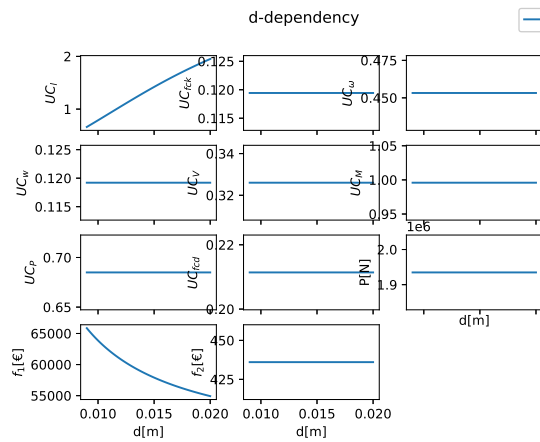
Figure E.16: Scenario (B): d-dependency
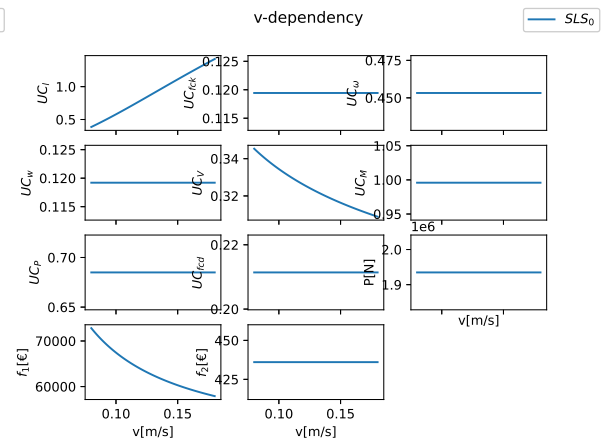
Figure E.17: Scenario (B): v-dependency
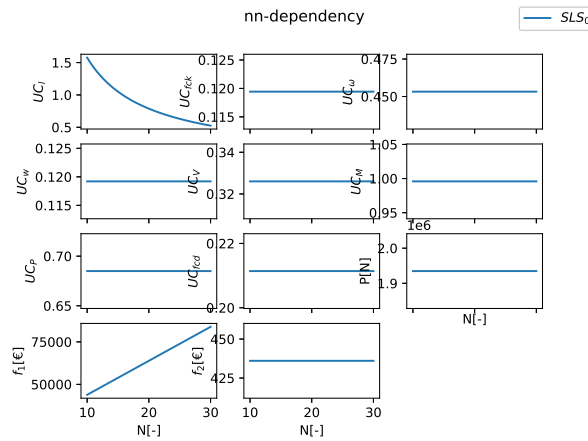
Figure E.18: Scenario (B): N-dependency

E.2. Uncertainty analysis: histograms of output quantities
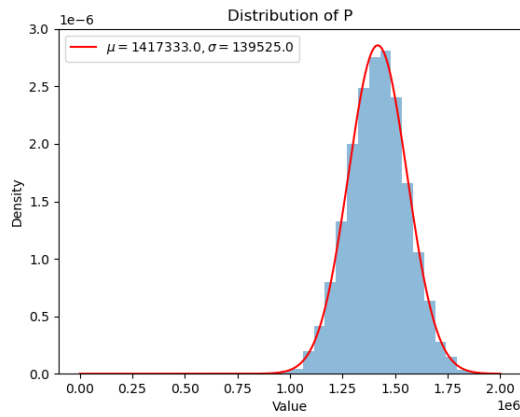
Figure E.19: Distribution of model output P for input uncertainty parameters
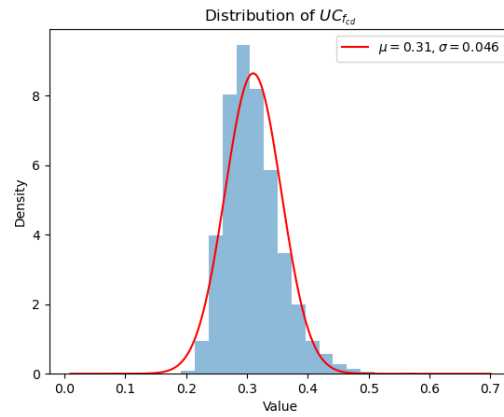
Figure E.20: Distribution of model output UC_{fcd} for input uncertainty parameters
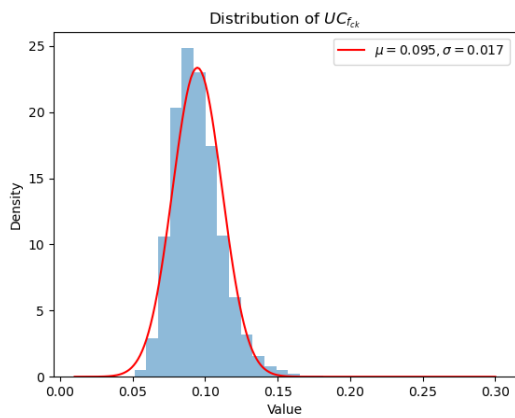

Figure E.21: Distribution of model output UC_{fck} for input uncertainty parameters
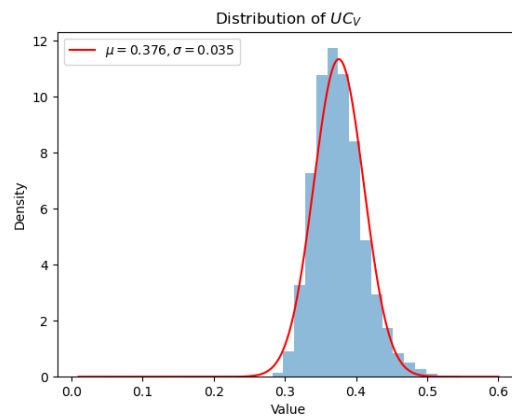
Figure E.22: Distribution of model output UC_V for input uncertainty parameters
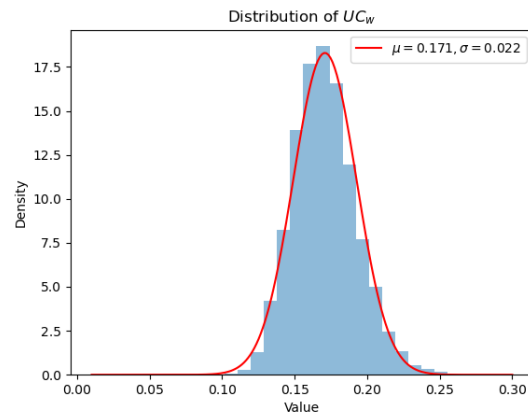
Figure E.23: Distribution of model output UC_w for input uncertainty parameters

Material data analysis

F.1. Description of data

In total, 647 samples have been printed. On the start and end of each production day (in total: 30) a set of 12 samples were printed (one a single production day, one concrete batch was used) resulting into 24 samples per day. Per direction, one sample was tested after 7 days and three samples were tested after 28 days, each of them once on flexural strength and twice on compressive strength. In this research, focus is on the 28 day test results. In total, 647 flexural tests have been performed and 1294 compression tests. The three different test directions are depicted in fig. F.1.

	A	1	Flexural vertical to the print direction
		2	Compression vertical to the print direction
	B	3	Flexural horizontal to the print direction
		4	Compression horizontal to the print direction
	C	5	Flexural horizontal perp. to the print direction
		6	Compression horizontal perp. to the print direction

Figure F.1: Three different test directions

F.2. Analysis: directional dependency

First, it has been analysed if there is a significant difference between the three different test-directions by a sequence of t-tests. All data per direction is used, so no distinction is made between the different days. This means that the population per direction is equal to 180, for the flexural test and both compression tests. To be able to use a t-test, the data must be normally distributed. This can be done by using the normality tests developed by D'Agostino and Pearson's which is built into the scipy.stats package of Python. The following null-hypothesis is tested for each sample direction:

"The measurement data per test direction comes from a normal distribution."

The normality test results are given in fig. F.2. Assuming a confidence level of 99%, yields that 3 of the 9 samples are not normally distributed, since the null-hypothesis was rejected. Given that the majority of the direction is normally distributed, all samples are treated as such.

F_A	0.03212	C1_A	0.00229	not normal	C2_A	0.00079	not normal
F_B	0.50901	C1_B	0.3694		C2_B	0.37862	
F_C	0.18995	C1_C	0.00298	not normal	C2_C	0.01493	

Figure F.2: Results of normality tests for the directions A, B and C for the flexural tests (F) and two compression tests (C1 and C2). Green: H0 is rejected, red: H0 cannot be rejected.

For determining the directional dependency of the data, the following null-hypothesis is tested

F	A	B	C
A		0.51611	0.07372
B			0.01706
C			

C1	A	B	C
A		0.03156	0.1058988
B			0.000132
C			

C2	A	B	C
A		0.44083	0.00283
B			0.01407
C			

Figure F.3: T-values for testing the directional dependency. Green: H0 is rejected, red: H0 cannot be rejected.

"The averages of the two directions are not significantly different."

This is done using a two-sided t-test assuming two related samples, available in the scipy package. The results are given in fig. F.3 and assuming a confidence level of 99%, it can be concluded that the flexural strength does *not show* a directional dependency. The compressive strength however shows a directional dependency between direction A-C (C1) and B-C (C2). If a confidence level of 95% would be used, a higher directional dependency of C would be obtained. Because the results are not convincing, it is assumed that the null-hypothesis cannot be rejected, meaning that the directions are not dependent.

This means that both the flexural-strength and compressive-strength dataset are sufficiently large, being 492 and 984 respectively. In table F.1 the means and standard deviations per direction and of the directions on average are reported.

Table F.1: Average values per direction and on average. Each value is based on 162 data points (after removing NaNs).

	flexural [MPa]	**compr. 1** [MPa]	**compr. 2** [MPa]
A	10.17 +/-1.38	56.00 +/- 7.97	55.43 +/- 8.07
B	10.22 +/- 1.38	54.34 +/- 8.14	56.09 +/- 7.19
C	9.97 +/- 1.43	57.13 +/- 7.73	57.87 +/- 7.62
total	10.13 +/- 1.40	55.83 +/- 8.01	56.46 +/- 7.69
		56.15	

G

Optimisation: back-ground information

G.1. Derivative information

Calculation of 1$^{\text{st}}$-order derivatives

The trust-constrained optimisation algorithm requires first- and second-order derivative information. The gradient information of the multi-variate function can be described using the Jacobi matrix:

$$J_i = \left[\frac{\partial f_i}{\partial x_1} \cdots \frac{\partial f_i}{\partial x_n} \right] \tag{G.1}$$

where i = 1,2, corresponding to f_1 and f_2 as a function of the n$^{\text{th}}$ variable. These first-order derivatives are calculated using central finite differences as follows:

$$\frac{\partial f}{\partial x}(x) = \frac{f(x+h) - f(x-h)}{2h} \tag{G.2}$$

in which h is the perturbation step size. A suitable perturbation step-size should be determined by a sensitivity analysis, since too small or too large step-sizes yield numerical noise. Therefore, the derivatives of the objective functions and gradient function are plotted against the perturbation step size ranging from 10e-10 to 10e-1. An example of such function is given in fig. G.1, showing large numerical noise for step-sizes smaller than 10e-7. For brevity, the other derivative vs. perturbation step-size graphs are omitted here. It was concluded that a step-size between 10e-6 and 10e-3 is suitable for the derivative calculation of all functions.

Calculation of 2$^{\text{nd}}$-order derivatives
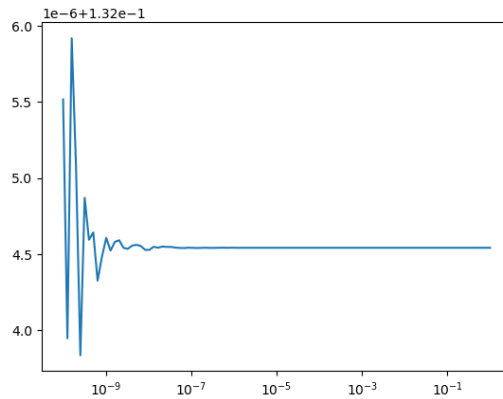
Figure G.1: Partial derivative of UC_l to b, for varying perturbation sizes.

The local curvature of the multivariate function can be described using the Hessian matrix, defined as follows, provided that the gradient of the function is continuous:

$$\mathbf{H} = \begin{bmatrix} \dfrac{\partial^2 f}{\partial x_1^2} & \dfrac{\partial^2 f}{\partial x_1\, \partial x_2} & \cdots & \dfrac{\partial^2 f}{\partial x_1\, \partial x_n} \\[2ex] \dfrac{\partial^2 f}{\partial x_2\, \partial x_1} & \dfrac{\partial^2 f}{\partial x_2^2} & \cdots & \dfrac{\partial^2 f}{\partial x_2\, \partial x_n} \\[2ex] \vdots & \vdots & \ddots & \vdots \\[2ex] \dfrac{\partial^2 f}{\partial x_n\, \partial x_1} & \dfrac{\partial^2 f}{\partial x_n\, \partial x_2} & \cdots & \dfrac{\partial^2 f}{\partial x_n^2} \end{bmatrix}$$

or

$$H_{i,j} = \frac{\partial^2 f}{\partial x_i \partial x_j}. \tag{G.3}$$

However, the evaluation of the Hessian is difficult to implement and computationally intensive. Therefore, the quasi-Newton method BFGS is used to approximate the Hessian, using the available gradient information. This strategy is adopted for calculating both the Hessian of the objective- and constraint functions.

G.2. Implementation

The precoded algorithms provided in the SciPy package for Python are used for the BFGS update strategy and Trust-Constrained optimisation. The first order gradient information is programmed manually using eq. (G.2). The settings are set to default. For each optimisation run, an initial design variable set x_0 must be provided, which is set to $\mathbf{x} = [0.7, 5, 0.05, 0.01, 0.12, 10]$.

H
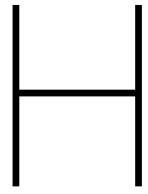
Scripts

H.1. Diana FEA Python definition

```python
###############################################################################
# DianaIE 10.2 update 2017-12-20 17:53:44
# Python  3.6.1
# Session recorded at 2020-01-28 11:34:51
###############################################################################

#INITIALIZE PROJECT
newProject( "../Desktop/Afstuderen/Phase2 - Create and validate
model/model/3d_val/3d_F", 100 )
setModelAnalysisAspects( [ "STRUCT" ] )
setModelDimension( "3D" )
setDefaultMeshOrder( "LINEAR" )
setDefaultMesherType( "HEXQUAD" )
setViewPoint( "ISO1" )
fitAll(  )


#SET GEOMETRY
#variable dimensions in [m]
b = 0.05; #layer thickness
W = 5.0; #width
H = 1.00 #height
L = 10.0;
n = 3; #number of bays

w_n = (W-(n)*2*b)/(n);
e_p = 0.1 #from bottom
P = 355281*0.8

createSheet( "Sheet 1", [[ 0, 0, 0 ],[ W, 0, 0 ],[ W, 0, H ],[ 0, 0, H ]] )
createSheet( "Sheet 2", [[ b, 0, b ],[ b+w_n, 0, b ],[ b+w_n, 0, H-b ],[ b, 0, H-b]] )
arrayCopy( [ "Sheet 2" ], [ w_n+2*b, 0, 0 ], [ 0, 0, 0 ], [ 0, 0, 0 ], (n-1) )

subtract_list = []
for i in range(n):
    subtract_list.append("Sheet "+str(i+2))

subtract( "Sheet 1", subtract_list[:], False, True )

extrudeProfile( [ "Sheet 1" ], [ 0, L, 0 ] )

createBlock( "toplayer", [0,0,H],[W,L,0.09])

createSheet( "Sheet 7", [[ 0.5, 0, H ],[ W-0.5, 0, H ],[ W-0.5, L, H ],[ 0.5, L, H]] )
imprintIntersection( "toplayer", "Sheet 7", True )
removeShape( [ "Sheet 7" ] )

createBlock( "Block 1", [ 0, -0.3, 0 ], [ W, 0.3, H+0.09 ] )
addMaterial( "concrete", "CONCDC", "EN1992", [ "TOTCRK" ] )
setParameter( "MATERIAL", "concrete", "EC2CON/NORMAL/CLASS", "C30/37" )
setElementClassType( "SHAPE", [ "Block 1", "toplayer" ], "STRSOL" )
assignMaterial( "concrete", "SHAPE", [ "Block 1","toplayer" ] )
arrayCopy( [ "Block 1" ], [ 0, L+0.3, 0 ], [ 0, 0, 0 ], [ 0, 0, 0 ], 1 )

createPointBody( "Vertex 1", [ 0, -0.3, 0 ] )
translate( [ "Vertex 1" ], [ (w_n/2)+b, 0, e_p ] )

arrayCopy( [ "Vertex 1" ], [ (w_n+2*b), 0, 0 ], [ 0, 0, 0 ], [ 0, 0, 0 ], (n-1) )
vertex_list = ["Vertex 1"]
for i in range(n*2-1):
    vertex_list.append("Vertex "+str(i+2))

mid = n
arrayCopy( vertex_list[0:mid], [ 0, L+2*0.3, 0 ], [ 0, 0, 0 ], [ 0, 0, 0 ], 1 )

for i in range(0,mid):
    imprintIntersection( "Block 1", vertex_list[i], True )
```

```python
67
68      for i in range(mid,n*2):
69          imprintIntersection( "Block 2", vertex_list[i], True )
70
71      removeShape( vertex_list[:] )
72
73
74
75      addMaterial( "3DPC", "CONCR", "LEI", [] )
76      setParameter( "MATERIAL", "3DPC", "LINEAR/ELASTI/YOUNG", 3e+10 )
77      setParameter( "MATERIAL", "3DPC", "LINEAR/ELASTI/POISON", 0.3 )
78      setParameter( "MATERIAL", "3DPC", "LINEAR/MASS/DENSIT", 2120 )
79
80      setElementClassType( "SHAPE", [ "Sheet 1" ], "STRSOL" )
81      assignMaterial( "3DPC", "SHAPE", [ "Sheet 1" ] )
82
83
84      #DEFINE SUPPORTS
85      addSet( "GEOMETRYSUPPORTSET", "pinned" )
86      createLineSupport( "pinned", "pinned" )
87      setParameter( "GEOMETRYSUPPORT", "pinned", "AXES", [ 1, 2 ] )
88      setParameter( "GEOMETRYSUPPORT", "pinned", "TRANSL", [ 1, 1, 1 ] )
89      setParameter( "GEOMETRYSUPPORT", "pinned", "ROTATI", [ 0, 0, 0 ] )
90      attach( "GEOMETRYSUPPORT", "pinned", "Block 1", [[ W/2, L, 0 ]] )
91
92      addSet( "GEOMETRYSUPPORTSET", "roller" )
93      createLineSupport( "roller", "roller" )
94      setParameter( "GEOMETRYSUPPORT", "roller", "AXES", [ 1, 2 ] )
95      setParameter( "GEOMETRYSUPPORT", "roller", "TRANSL", [ 0, 0, 1 ] )
96      setParameter( "GEOMETRYSUPPORT", "roller", "ROTATI", [ 0, 0, 0 ] )
97      attach( "GEOMETRYSUPPORT", "roller", "Sheet 1", [[ W/2, L, 0 ]] )
98
99
100     #DEFINE WHEEL CONTACT POINTS
101     createSheet( "Sheet 20", [[ W/2+1.75/2, L/2+3/2, H+0.09 ],[ W/2+1.75/2, L/2+3/2-0.25,
        H+0.09  ],[ W/2+1.75/2-0.25, L/2+3/2-0.25, H+0.09  ],[ W/2+1.75/2-0.25, L/2+3/2,
        H+0.09 ]] )
102     mirror( [ "Sheet 20" ], [ W/2, 0, 0 ], [ True, False, False ], True )
103     mirror( [ "Sheet 20", "Sheet 21" ], [ 0, L/2, 0 ], [ False, True, False ], True )
104     translate( [ "Sheet 20", "Sheet 21", "Sheet 22", "Sheet 23" ], [w_n/2,0,0])
105     projection( "toplayer", [ "Sheet 20", "Sheet 21", "Sheet 22", "Sheet 23" ], [ 0, 0, -1
        ], True )
106     removeShape( [ "Sheet 20", "Sheet 21", "Sheet 22", "Sheet 23" ] )
107
108     #DEFINE LOADS
109     addSet( "GEOMETRYLOADSET", "q_sw" )
110     createModelLoad( "q_sw", "q_sw" )
111
112
113     #UNCOMMENT IF NO TOP-LAYER IS PRESENT
114     #addSet( "GEOMETRYLOADSET", "q_perm" )
115     #createSurfaceLoad( "q_perm", "q_perm" )
116     #setParameter( "GEOMETRYLOAD", "q_perm", "FORCE/VALUE", -3000 )#[N/m2]
117     #setParameter( "GEOMETRYLOAD", "q_perm", "FORCE/DIRECT", 3)
118     #attach( "GEOMETRYLOAD", "q_perm", "toplayer", [[ 3.0810785, 6.6534468, H+0.09 ]] )
119
120     addSet( "GEOMETRYLOADSET", "q_var" )
121
122     #UNCOMMENT 123-126 FOR A DISTRIBUTED VARIABLE LOAD
123     #createSurfaceLoad( "q_var", "q_var" )
124     #setParameter( "GEOMETRYLOAD", "q_var", "FORCE/VALUE", -5000 ) #[N/m2]
125     #setParameter( "GEOMETRYLOAD", "q_var", "FORCE/DIRECT", 3 )
126     #attach( "GEOMETRYLOAD", "q_var", "toplayer" , [[ 3.0810785, 6.6534468, H+0.09 ]])
127
128     #UNCOMMENT 129-132 TO DEFINE POINT-LOADS FROM THE SERVICE VEHICLE
129     createSurfaceLoad( "wheelload", "q_var" )
130     setParameter( GEOMETRYLOAD, "wheelload", "FORCE/VALUE", -200000 )
```

```
131    setParameter( GEOMETRYLOAD, "wheelload", "FORCE/DIRECT", "NORMAL" )
132    attach( GEOMETRYLOAD, "wheelload", "toplayer", [[ W/2+1.75/2-0.25/2+w_n/2,
       L/2+3/2-0.25/2, H+0.09   ],[ W/2-1.75/2+0.25/2+w_n/2, L/2+3/2-0.25/2, H+0.09   ],[
       W/2+1.75/2-0.25/2+w_n/2, L/2-3/2+0.25/2, H+0.09   ],[ W/2-1.75/2+0.25/2+w_n/2,
       L/2-3/2+0.25/2, H+0.09   ]] )
133
134    createPointLoad( "prestress_front", "prestress")
135    createPointLoad( "prestress_back", "prestress" )
136    setParameter( "GEOMETRYLOAD", "prestress_front", "FORCE/VALUE", P/n )
137    setParameter( "GEOMETRYLOAD", "prestress_front", "FORCE/DIRECT", 2 )
138    setParameter( "GEOMETRYLOAD", "prestress_back", "FORCE/VALUE", -P/n )
139    setParameter( "GEOMETRYLOAD", "prestress_back", "FORCE/DIRECT", 2 )
140
141    x = []
142    for i in range(0,mid):
143        x.append(0)
144        x[i] = w_n/2+b+(i)*(w_n)+(2*i)*b
145        x[0] = w_n/2+b
146
147    point_list_front=[]
148    point_list_back=[]
149    for i in range(0,mid):
150        point_list_front.append([x[i], -0.3, e_p])
151        point_list_back.append([x[i], L+0.3, e_p])
152    attach( "GEOMETRYLOAD", "prestress_front", "Block 1", point_list_front[:] )
153    attach( "GEOMETRYLOAD", "prestress_back", "Block 2", point_list_back[:] )
154
155
156    setDefaultGeometryLoadCombinations(  )
157    #FC1
158    setGeometryLoadCombinationFactor( "Geometry load combination 1", "q_var", 0.6 )
159    setGeometryLoadCombinationFactor( "Geometry load combination 1", "q_perm", 1.35 )
160    setGeometryLoadCombinationFactor( "Geometry load combination 1", "q_sw", 1.35 )
161    setGeometryLoadCombinationFactor( "Geometry load combination 1", "prestress", 1 )
162    setGeometryLoadCombinationFactor( "Geometry load combination 2", "q_var", 0.6 )
163    setGeometryLoadCombinationFactor( "Geometry load combination 2", "q_sw", 1.35 )
164    setGeometryLoadCombinationFactor( "Geometry load combination 2", "q_perm", 1.35 )
165    setGeometryLoadCombinationFactor( "Geometry load combination 2", "prestress", 0 )
166    #FC2 (LC3 is governing)
167    setGeometryLoadCombinationFactor( "Geometry load combination 3", "q_var", 1.35 )
168    setGeometryLoadCombinationFactor( "Geometry load combination 3", "q_sw", 1.2 )
169    setGeometryLoadCombinationFactor( "Geometry load combination 3", "q_perm", 1.2 )
170    setGeometryLoadCombinationFactor( "Geometry load combination 3", "prestress", 1 )
171    setGeometryLoadCombinationFactor( "Geometry load combination 4", "q_var", 1.35 )
172    setGeometryLoadCombinationFactor( "Geometry load combination 4", "q_perm", 1.2 )
173    setGeometryLoadCombinationFactor( "Geometry load combination 4", "q_sw", 1.2 )
174    setGeometryLoadCombinationFactor( "Geometry load combination 4", "prestress", 0 )
175
176
177    generateMesh( [] )
178
179    setElementSize( [ "Sheet 1", "Block 1", "Block 2", "toplayer" ], 0.1, -1, True )
180    setMesherType( [ "Sheet 1" ], "HEXQUAD" )
181    generateMesh( [] )
182
183    addAnalysis( "3d_F" )
184    addAnalysisCommand( "3d_F", "LINSTA", "Structural linear static" )
185    renameAnalysisCommand( "3d_F", "Structural linear static", "Structural linear static" )
186    runSolver( "3d_F" )
187    showView( "RESULT" )
188
189
```

H.2. Main calculation model: Python definition

```python
# -*- coding: utf-8 -*-
"""
Created on Wed Apr 29 13:59:22 2020

@author: Maartje
"""

def
main(X,bc,material,printing=False,config=['linear',None],top="box",scenario='A',preq='
ULSfctd',tdparams=[50,20,28,7],Q=[320,5,350,2000]):
    '''
    W = bc[0]
    L = bc[1]
    a = bc[2]
    H = x[0]
    n = x[1]
    b = x[2]
    d = x[3]
    v = x[4]
    nn = x[5]

    Parameters
    ----------
    X : list
        variables [H,n,b,d,v,N]
    bc : list
        boundaryconditions [W,L,a]
    material : list or dict
        list[materialtype,degree] or specified manually in dict
    printing : boolean, optional
        print to screen. The default is False.
    config : list, optional
        ['linear' or 'kinked',None or l_p]. The default is ['linear',None].
    top :string, optional
        "box" (Default) or "bottle", referring to the cross-section topologies.
    scenario : string
        'A' (Default): joints are stronger than concrete; 'B': joints have 0 strength
    preq : string
        requirement to design the prestress. 'ULSfctd' (Default): requires a
        limitation of tension in ULS to f_ctd; 'SLS0': requires zero tension in SLS.
    tdparams : list
        [RH, T, t_0, t_s] = [ambient RH [%], ambient T [C], age at loading [days],
        age at drying[days]]. The default is [50%,20C,28d,7d].
    Q : list
        the prices for [M, P, T, J] respectively. Default is [320,5,350,2000]

    Returns
    -------
    named tuple
        UC_fcd,UC_fctd,UC_shear,UC_w,UC_li,M,P,T,V_c,M_p,e_p,s_b_p,s_t_p
    '''

    if scenario=='B' and preq=='ULSfctd':
        print('This is not possible, as the concrete cannot deliver any strength for
        any tensile stress at the bottom')

    if type(material) == dict:
        mat = material
        deg = mat.get("deg")

    if type(material) == list:
        mat = matdict.get(material[0])
        deg = material[1]

    rho_f = mat.get("rho_f")
    E_0 = mat.get("E_0")
    slope_E = mat.get("slope_E")
    sigma_0 = mat.get("sigma_0")
    slope_sigma = mat.get("slope_sigma")
    C_0 = mat.get("C_0")
    slope_C = mat.get("slope_C")
    phi = mat.get("phi")
```

```python
68          f_ck = mat.get("f_ck")
69          f_ctk = mat.get("f_ctk")
70          rho = mat.get("rho")
71          E = mat.get("E")
72
73          W = bc[0]
74          L = bc[1]
75          a = bc[2]
76          H = X[0]
77          n = X[1]
78          b = X[2]
79          d = X[3]
80          v = X[4]
81          nn = X[5] #nr of bridge elements, called N in report! but name N is already
            taken here
82
83          N = int((L/dx+1))
84          H0 = H
85
86          file = open(r"C:\Users\Maartje\Desktop\Afstuderen\2_modelling\model\lengths.txt")
87          lengths=file.readlines()
88
89
90          A,Iy,ez_top,ez_bot,H,H_n,W_bot,W_top = ([] for i in range(8))
91
92          if top == "box":
93              for x in range(0,N):
94                  W_n = (W-(n)*2*b)/n
95                  H.append(H0 -(((-4*a*(x*dx)**2)/(L**2)+4*a*(x*dx)/L)))
96                  H_n.append((H[x]-2*b))
97                  A.append(W*H[x]-n*W_n*H_n[x]) #crosec area [m2]
98                  Iy.append(W*1/12*H[x]**3-n*1/12*W_n*H_n[x]**3) #moment of inertia [m4]
99                  ez_top.append((H[x])/2)
100                 ez_bot.append(-(H[x])/2)
101                 W_bot.append(Iy[x]/-ez_bot[x]) #positive value
102                 W_top.append(Iy[x]/ez_top[x]) #positive value
103             b_w = (n)*2*b
104             S_c = (b*W*(ez_top[0]-b/2))+(((ez_top[0]-b)*b_w)*(ez_top[0]-b)/2) #[m3] top
                part of cross-section
105             S = 2*(W-b) + (2*n)*(H[0]-b) #[m] total printpath length
106             S2 = float(lengths[0]) #[m] print-path length via Grasshopper calculation
107
108         if top=="bottle":
109             file =
                open(r"C:\Users\Maartje\Desktop\Afstuderen\2_modelling\model\bottle.txt")
                #read Grasshopper output
110             bottle=file.readlines()
111             A0 = float(bottle[0])
112             Iy0 = float(bottle[1])
113             ez0 = float(bottle[2])
114             for x in range(0,N):
115                 H.append(H0) #height [m], determined via Grasshopper calculation
116                 A.append(A0) #crosec area [m2], determined via Grasshopper calculation
117                 Iy.append(Iy0) #moment of inertia [m4], determined via Grasshopper
                    calculation
118                 ez_top.append(ez0)
119                 ez_bot.append(-H0+ez0)
120                 W_bot.append(Iy[x]/-ez_bot[x]) #positive value
121                 W_top.append(Iy[x]/ez_top[x]) #positive value
122             A_top = float(bottle[3])
123             Iy_top = float(bottle[4])
124             e_top = float(bottle[5])
125             b_w = 2*n*b
126             S_c = A_top*(e_top-ez0)
127             S = float(lengths[1]) #[m] print-path length via Grasshopper calculation
128
129         ti = S/v #[s] layer interval time
130         M = (sum(A[:])/len(A))*L*rho #[kg]
131         V_c = (sum(A[:])/len(A))*L #concrete volume[m3]
132
133         q_1_SLS, q_2_SLS, q_3_SLS, q_1_ULS, q_2_ULS, q_3_ULS, FC1, FC2,q_sw,V_Edx= ([]
            for i in range(10))
```

```python
134         sigma_bot_p,sigma_top_p,moments_p = ([] for i in range(3))
135         moments,sigma_bot,sigma_top = ([] for i in range(3))
136
137         N = int((L/dx+1))
138         xx = np.linspace(0,L,N)
139         ms = int(len(xx)/2+1) #determine mid-span position
140
141         #decrease tensile strength with increasing layer interval time
142         def bond_ti(ti,deg):
143             if deg==0: #no decrease
144                 f = 1
145             if deg==1: #moderate decrease
146                 f = -0.151*np.log(ti) + 0.9811 #input ti in [min]
147             if deg==2: #high decrease
148                 f = 0.8642*ti**(-0.45) #input ti in [min]
149             return f
150
151         f_ctd = f_ctk/1.5*0.8*(bond_ti(ti/60,deg)) #[MPa], design tensile stress
152         f_cd = f_ck/1.5*0.8 #[MPa]
153         f_cm = f_ck+8 #3.1.2 EC2
154
155         '''DYNAMICS CHECK'''
156         k = 48*E*1E6*Iy[0]/(L**3)
157         omega_n = np.sqrt(k/M)/(2*np.pi)
158
159         UC_omega = 5/omega_n
160
161         '''CALCULATE NORMAL STRESSES AND P'''
162         #stage0: self-weight only
163         #stage1: self-weight+prestressing (off-site)
164         #stage2: self-weight+prestressing+toplayers (on-site, after casting
         concrete+asphalt)
165         #stage3: self-weight+prestressing+toplayers+variableload (use-phase)
166         #DEFINE LOADS AND LOAD COMBINATIONS
167
168         rho = rho*g/1000 #[kN/m3]
169
170         for x in range(0,N):
171             #permanent karakteristiek
172             q_sw.append(rho*A[x])    #self-weight [kN/m]
173             q_perm = (5)*(W-1) #compr.layer+wear layer+integrated parapet [kN/m]
174
175             #veranderlijk karakteristiek
176             q_var = 5*(W-1) #variable load, works on width minus one meter [kN/m]
177             q_wind = 0.5*(W) #windload [kN/m]
178             q_sn = 0.56*(W) #snowload [kN/m]
179
180             if CC == "CC_1":
181                 gamma_G1 = 1.2
182                 gamma_Q1 = 1.35
183                 gamma_Q1_t = 1.2 #lower value for traffic loads
184                 gamma_G2 = 1.1
185                 gamma_Q2 = 1.35
186                 gamma_Q2_t = 1.2#lower value for traffic loads
187
188             if CC == "CC_2":
189                 gamma_G1 = 1.2
190                 gamma_Q1 = 1.5
191                 gamma_Q1_t = 1.35 #lower value for traffic loads
192                 gamma_G2 = 1.35
193                 gamma_Q2 = 1.5
194                 gamma_Q2_t = 1.35 #lower value for traffic loads
195
196
197             q_1_SLS.append(q_sw[x])#SLS: characteristic/frequent self-weight only,
         governing for maximum prestress
198             q_2_SLS.append(q_sw[x]+q_perm+q_var+0.3*q_wind+0*q_sn)#SLS: characteristic,
         for deformations (temperature is favourable so 0)
199             q_3_SLS.append((q_sw[x]+q_perm)+0.8*q_var+0*q_wind+0*q_sn)#SLS: frequent,
         for crack width (temperature is favourable so 0)
200
201             q_1_ULS.append(gamma_G1*(q_sw[x]+q_perm)) #ULS: permanent loads only
```

```python
202             q_2_ULS.append(gamma_G1*(q_sw[x]+q_perm)) #NOT USED HERE
203
            FC1.append(gamma_G1*(q_sw[x]+q_perm)+gamma_Q1_t*q_var+gamma_Q1*(0.3*q_wind+0*q
            _sn))#eq. 6.10b (temperature is favourable so 0)
204
            FC2.append(gamma_G2*(q_sw[x]+q_perm)+gamma_Q2_t*q_var*0.4+gamma_Q2*(0.3*q_wind
            +0*q_sn))#eq. 6.10a (temperature is favourable so 0)
205             q_3_ULS.append(max([FC1[x],FC2[x]])) #ULS: full load
206
207         q_list = [q_1_SLS, q_2_SLS, q_3_SLS, q_3_ULS,q_1_ULS]
208
209     #calculate moments and stresses along beam
210     for i in range(len(q_list)):
211         moments.append([])
212         sigma_bot.append([])
213         sigma_top.append([])
214         for x in range(len(xx)):
215             moments[i].append(q_list[i][x]*(x*dx)/2*(L-(x*dx))) #[kNm]
216             sigma_top[i].append(-q_list[i][x]*(x*dx)/2*(L-(x*dx))/(W_top[x])/1000)
                #[N/mm2], negative because compression at the top
217             sigma_bot[i].append(q_list[i][x]*(x*dx)/2*(L-(x*dx))/(W_bot[x])/1000)
                #[N/mm2]
218             V_Edx.append(-(x*dx)*q_list[3][x] + q_list[3][x]*L/2) #[kN]
219
220     gamma_P = 1.0
221
222     if config[0]=='linear':
223         #for linear tendon profile
224         #e_edge = max(0.1,a) #minimum 100mm from bottom edge OR the offset a
225         e_edge = 0.1 #assume we can 'cut' the bridge at the bottom
226
227         e_p = []
228         for x in range(0,len(xx)):
229             e_p.append(H[0]-ez_top[x]-e_edge)
230
231         if preq == 'SLS0': #calculate P, based on no tension in SLS (characteristic
        load combination)
232             ten_tol = 0 #maximum allowed tensile stress in SLS
233             P =
            ((ten_tol*1E6-sigma_bot[2][ms]*1E6)/((-e_p[ms])/(W_bot[ms])-1/A[ms]))/0.8
            #P in [N]! this is P_0
234             sigma_top_p_crit = ((sigma_top[0][0] - P/A[0]*1E-6 +
            (P*e_p[0]/W_top[0])*1E-6)) #check if no tension is present at support
            level
235
236             #iterate and decrease e_p until no high tension at top anymore at SLS
237             count=0
238             while sigma_top_p_crit > 0:
239                 count+=1
240                 if count==100:
241                     break
242                 for x in range(0,len(xx)):
243                     e_p[x] -= 0.01
244                 P =
                ((ten_tol*1E6-sigma_bot[2][ms]*1E6)/((-e_p[ms])/(W_bot[ms])-1/A[ms]))/
                0.8 #P in [N]! this is P_0
245                 sigma_top_p_crit = ((sigma_top[0][0]*0.9 - P/A[0]*1.1*1E-6 +
                (P*e_p[0]*1.1/W_top[0])*1E-6))
246
247         if preq == 'ULSfctd': #calculate P, based on limited tension in ULS
248             ten_tol = f_ctd #maximum allowed tensile stress in ULS
249             P =
            ((ten_tol*1E6-sigma_bot[3][ms]*1E6)/((-e_p[ms])/(W_bot[ms])-1/A[ms]))/0.8
            #P in [N]! this is P_0
250             sigma_top_p_crit = ((sigma_top[0][0]*0.9 - P/A[0]*1.1*1E-6 +
            (P*e_p[0]*1.1/W_top[0])*1E-6)) #check if no tension is present at
            support level
251
252             #iterate and decrease e_p until no high tension at top anymore at SLS
253             count=0
254             while sigma_top_p_crit > f_ctd:
255                 count+=1
```

```python
                            if count==100:
                                break
                            for x in range(0,len(xx)):
                                e_p[x] -= 0.01
                            P = ((ten_tol*1E6-sigma_bot[3][ms]*1E6)/((-e_p[ms])/(W_bot[ms])-1/A[ms]))/0.8 #P in [N]! this is P_0
                            sigma_top_p_crit = ((sigma_top[0][0]*0.9 - P/A[0]*1.1*1E-6 + (P*e_p[0]*1.1/W_top[0])*1E-6))


            sigma_bot_p = []
            sigma_top_p = []
            #calculate all stresses with prestress, after losses!
            for j in range(0,len(q_list)):
                sigma_bot_p.append([])
                sigma_top_p.append([])
                for i in range(0,len(xx)):
                    sigma_bot_p[j].append((sigma_bot[j][i] - P*0.8/A[i]*1E-6 - (P*0.8*e_p[i]/W_bot[i])*1E-6))
                    sigma_top_p[j].append((sigma_top[j][i] - P*0.8/A[i]*1E-6 + (P*0.8*e_p[i]/W_top[i])*1E-6))

            if P<0:
                P = 0

            #make plot of cross-section, optional
            plot = False
            if plot:
                plt.plot(xx,(((-4*a*(xx)**2)/(L**2)+4*a*(xx)/L)), 'k')
                plt.plot(xx,H[0]-ez_top, 'g--', label='c.a.')
                plt.hlines(H[0],0,L, 'k')
                plt.hlines(e_edge,0,L, 'b',label='P')
                plt.axvline(0,color='k')
                plt.axvline(L,color='k')
                plt.ylim(0,H[0]+0.01)
                plt.grid()
                plt.legend()
                plt.savefig('cro-sec')

        if config[0]=='kinked':
            #for linear tendon profile
            #e_edge = max(0.1,a) #minimum 100mm from bottom edge OR the offset a
            e_edge = 0.1 #assume we can 'cut' the bridge at the bottom
            l_p = config[1] #distance over which the tendon profile is sloped, measured from outside
            e_p = H[0]/2-e_edge
            a_p = np.arctan(e_p/l_p)

            #calculate P, based on no tension in SLS (characteristic load combination))
            if preq == 'SLS0': #calculate P, based on no tension in SLS (characteristic load combination)
                ten_tol = 0 #maximum allowed tensile stress in SLS
                P = ((ten_tol*1E6-sigma_bot[2][ms]*1E6)/((-np.sin(a_p)*l_p)/(W_bot[ms])-1/A[ms]))/gamma_P/0.8 #P in [N]! this is P_0
            if preq == 'ULSfctd': #calculate P, based on limited tension in ULS
                ten_tol = f_ctd #maximum allowed tensile stress in ULS
                P = ((ten_tol*1E6-sigma_bot[2][ms]*1E6)/((-np.sin(a_p)*l_p)/(W_bot[ms])-1/A[ms]))/gamma_P/0.8 #P in [N]! this is P_0

            sigma_bot_p = np.zeros((len(q_list),len(xx)))
            sigma_top_p = np.zeros((len(q_list),len(xx)))
            #calculate all stresses with prestress, after losses!
            for j in range(0,len(q_list)):
                for i in range(0,len(xx)):
                    if xx[i]>l_p and xx[i]<(L-l_p):
                        sigma_bot_p[j][i] = ((sigma_bot[j][i] - P*0.8/A[i]*1E-6 - (P*0.8*-np.sin(a_p)*l_p/W_bot[i])*1E-6))
                        sigma_top_p[j][i] = ((sigma_top[j][i] - P*0.8/A[i]*1E-6 + (P*0.8*-np.sin(a_p)*l_p/W_top[i])*1E-6))
```

```python
                    if xx[i]>0 and xx[i]<l_p:
                        sigma_bot_p[j][i] = ((sigma_bot[j][i] - P*0.8/A[i]*1E-6 -
                        (P*0.8*-np.sin(a_p)*xx[i]/W_bot[i])*1E-6))
                        sigma_top_p[j][i] = ((sigma_top[j][i] - P*0.8/A[i]*1E-6 +
                        (P*0.8*-np.sin(a_p)*xx[i]/W_top[i])*1E-6))

            if P<0:
                P = 0
            e_p = np.ones((x))*e_p

        #calculate required prestress area, assuming sigma_p0 = 1395 N/mm2
        A_p = P/1395 #[mm2]
        M_p = A_p/1e6*L*7850 #[kg]

        """SHEAR"""
        if config[0] == 'linear':
            V_Ed = abs(V_Edx[0])
        if config[0] == 'kinked':
            V_Ed = abs(V_Edx[0])

        #NEN-EN 1992-1-1 eq. 6.2b
        k = 1
        v_min = 0.035*k**(3/2)*f_ck**0.5 #[N/mm2]
        k1 = 0.15
        sigma_cp = abs(P/A[0])*1E-6*0.9 #[N/mm2], voorspanning werkt gunstig
        sigma_cp = min(sigma_cp,0.2*f_ck)
        V_Rdc1 = (v_min+k1*sigma_cp)*1E6*b_w*(H[0]/2-b)/1000 #[kN] 'effectieve hoogte'
        is hier H-2*b --> moet dit niet halve hoogte zijn?

        #NEN-EN 1992-1-1 eq 6.4
        alpha_l = 1 #nagerekt staal
        V_Rdc2 = (Iy[0]*b_w/S_c)*np.sqrt((f_ctd**2+alpha_l*sigma_cp*f_ctd))*1000 #[tkN]

        #NEN-EN 1992-1-1 eq 12.6.3 (unreinforced concrete)
        tau_cp = 1.5*V_Ed*1000/A[0]*1e-6 #[N/mm2] eq12.4
        sigma_cp = abs(P/A[0])*1E-6 #[N/mm2] eq 12.3

        sigma_clim = f_cd-2*(f_ctd*(f_ctd+f_cd))**0.5 #[N/mm2] eq 12.7
        if sigma_cp <= sigma_clim:
            f_cvd = np.sqrt(f_ctd**2+sigma_cp*f_ctd) #[N/mm2] eq 12.5
        if sigma_cp > sigma_clim:
            f_cvd = np.sqrt(f_ctd**2+sigma_cp*f_ctd - ((sigma_cp-sigma_clim)/2)**2)
            #[N/mm2] eq 12.6

        UC_3 = tau_cp/f_cvd
        V_Rd12 = max(V_Rdc1,V_Rdc2)
        UC_12 = V_Ed/V_Rd12

        #creep coefficient at t=inf
        RH = tdparams[0]
        t_0 = tdparams[2] #[days], assumption
        t_inf = 365*100 #life-span is 100 years
        A_c = A[0]
        u_phi = 2*W+2*H[0] #is deze perimeter niet veel groter?
        h_phi = 2*A_c/u_phi*1000
        alpha_1 = (35/f_cm)**(0.7)#[-]
        alpha_2 = (35/f_cm)**(0.2)#[-]
        alpha_3 = (35/f_cm)**(0.5)#[-]
        phi_RH = (1+(1-RH/100)/(0.1*h_phi**(1/3))*alpha_1)*alpha_2
        beta_fcm = 16.8/(f_cm**(0.5))
        beta_t0 = 1/(0.1+t_0**0.2)
        beta_H = min((1.5*h_phi*(1+(1.2*RH/100)**(18))+250*alpha_3),1500*alpha_3)
        beta_cinf = ((t_inf-t_0)/(beta_H+(t_inf-t_0)))**(0.3)
        phi_0 = phi_RH*beta_fcm*beta_t0
        phi_inf = phi_0*beta_cinf
        e_ccinf = P/A[0]/(E*1000000)*phi_inf*1000

        #shrinkage at t=inf
        t_s = tdparams[3]
        beta_RH = 1.55*(1-(RH/100)**3)
        alpha_ds1 = 6 #klasse R
        alpha_ds2 = 0.12 #klasse R
```

```python
383         e_cds0 = 0.85*((220+110*alpha_ds1)*np.exp(-alpha_ds2*f_cm/10))/1000000*beta_RH
384         beta_dsinf = ((t_inf-t_s)/(0.035*h_phi**2+(t_inf-t_s)))**0.5
385         e_cdsinf = e_cds0*beta_RH*beta_dsinf*1000
386         alpha_as = 600
387         e_cas0 = -alpha_as*((f_cm/10)/(6+f_cm/10))**(2.5)/1000000
388         beta_asinf = 1-np.exp(-0.2*t_inf**(1/2))
389         e_casinf = e_cas0*beta_asinf*1000
390         e_csinf = e_cdsinf+e_casinf
391         dP = A_p*(e_csinf*E_p + 0.8*dsigma_pr +
            E_p/E*phi_inf*sigma_cqp)/(1+E_p/E*A_p/A[0]*(1+A[0]/Iy[0]*e_p[0])*(1+0.8*phi_inf))
392
393         '''DEFINE UNITY CHECKS '''
394         UC_fck = ((P/A[0])/1E6)/(0.6*f_ck)
395
396         E_eff = E/(1+phi_inf)
397         w = (5.0/384.0*q_list[1][ms]*1000*L**4 -
            1/8*P*0.8*e_p[ms]*L**2)/(E_eff*1E6*Iy[ms]) #under characteristic LC
398         w_max = L/250.0
399         UC_w = w/w_max
400
401         UC_shear = max(UC_12,UC_3)
402
403         if scenario=='A':
404             UC_fcd = abs(sigma_top_p[3][ms])/f_cd #- add the UC for maximum compression
                at mid-span --> calculate compression zone
405             UC_fctd = (sigma_bot_p[3][ms])/f_ctd #check stress at mid-span in ULS
406
407         if scenario=='B': #kinematic mechanism
408             if P==0:
409                 UC_fcd = abs(sigma_top_p[3][ms])/f_cd
410                 UC_P = 0
411                 UC_M = 0
412             if P>0:
413                 E_p = 195000 #[MPa]
414                 delta = 0.01 #[m], deflection
415                 dL = delta/(L/2)*2*(ez_top[ms]-delta+e_p[ms])
416                 dP = dL/L*E_p*A_p #[N]
417                 N_c = P+dP#[N]
418                 eps_c = 3.5 #[promille]
419                 sigma_pinf = 0.8*P/(A_p)#[MPa]
420                 dsigma_p = dP/(A_p)
421                 if sigma_pinf + dsigma_p <= 1522:
422                     eps_p = (sigma_pinf+dsigma_p)/E_p #[promille]
423                 if sigma_pinf+ dsigma_p >1522:
424                     E_p2 = (1691-1522)/(35-7.81)*1000
425                     eps_p = 1522/E_p + (sigma_pinf+dsigma_p-1522)/E_p2*1000#[promille]
426                 x_u = 3.5*(ez_top[ms]-delta+e_p[ms])/(eps_p+3.5)#[m]
427                 A_xu = W*b+(n*2)*b*(x_u-b)
428                 UC_fcd = (N_c/A_xu/1e6)/f_cd
429                 UC_P = (sigma_pinf+dsigma_p)/1691
430                 UC_M =
                    (moments[3][ms]-P/1000*0.8*e_p[ms])/(N_c/1000*(ez_top[ms]-delta+e_p[ms]-x_
                    u/2))
431
432         '''FRESH CONCRETE FAILURE'''
433         l_dot = d*v/S #[m/s]
434
435         #PLASTIC COLLAPSE
436         #Mohr-Coulomb failure criterion
437         tau_0 = C_0
438         A_tau = slope_C + rho_f*g*l_dot*np.tan(phi)
439         l_ps = tau_0/(rho_f*g/np.sqrt(3) - A_tau/l_dot)
440
441         #compressive failure
442         l_pc = sigma_0/(-slope_sigma/l_dot + rho_f*g)
443
444         l_p = min(l_pc,l_ps)
445         if l_p<=0:
446             l_p = L
447
448         #ELASTIC BUCKLING
449         cur_El = slope_E/E_0
```

```python
450        D_0 = E_0*b**3/(12*(1-mu**2))
451        cur_El_d = (D_0/(rho_f*g*b))**(1/3)*cur_El/l_dot
452        s = max((H[0]-b),((W-b)/n))
453        s_d = ((rho_f*g*b)/(D_0))**(1/3)*s
454
455        def l_cr_d_lss(x,s_d):
456            #simply supported wall, read from design graphs, so low accuracy
457            s_d = int(s_d)
458            if s_d<=4 or s_d >= 4 and s_d<5:
459                f = 10.211*x**2+10.884*x+4.48
460            if s_d >= 5 and s_d<6:
461                f = 18.79*x**2-1.5061*x+2.8905
462            if s_d >= 6 and s_d<7:
463                f = 59.115*x**5-142.99*x**4+124.25*x**3-44.483*x**2+7.5387*x+2.5
464            if s_d >= 7 and s_d<8:
465                f = 3.2229*x**4-9.2019*x**3+8.7629*x**2-1.2838*x+2.5
466            if s_d >= 8 and s_d<9:
467                f = 0.5979*x**4-2.1482*x**3+2.4279*x**2+0.6015*x+2.3134
468            if s_d >= 9 and s_d<10:
469                f = 0.1111*x**3-0.2333*x**2+1.3841*x+2.1357
470            if s_d >= 10 and s_d<20:
471                f = 0.0714*x**2+1.0643*x+2.1286
472            if s_d >= 20:
473                f = -0.0667*x**2+1.0486*x+2.0281
474            return f
475
476        def l_cr_d_lf(x,beta):
477            # closed-form expression assuming free wall
478            f = 1.98635+(0.996+2.328*beta+0.268*beta**2)*x**(0.793+1.3*(1-np.exp(-2.762*beta))
                )#x = dimensionless curing rate
479            return f
480
481        l_cr_d_lf = l_cr_d_lf(cur_El_d,2.5)
482        l_cr_lf = l_cr_d_lf/((rho_f*g*b/D_0)**(1/3))
483
484        l_cr_d_lss = l_cr_d_lss(cur_El_d,s_d)
485        l_cr_lss = l_cr_d_lss/((rho_f*g*b/D_0)**(1/3))
486
487        l_cr = l_cr_lf #assume free wall
488
489        l_i = min(l_p,l_cr) #maximal possible element height
490
491        N_i = ((L/nn)/d) #aantal laagjes per element
492
493        UC_li = (L/nn)/l_i
494
495        T = N_i*ti*nn #total print time [s]
496
497        '''CALCULATE PERFORMANCE INDICATORS '''
498        # price_M = q[0] #€/ton
499        # price_P = q[1] #€/kg
500        # price_T = q[2] #€/h
501        # price_J = q[3] #€/joint
502
503        T_t = T/3600 #[h]
504        M_c = M/1000 #[tons]
505        J = nn-1 #[-] number of joints
506
507        q=Q
508        f1 = q[0]*M_c + q[1]*M_p + q[2]*T_t + q[3]*J
509        f2 = 32.39*V_c + 0.66*M_p
510
511
512        if printing:
513            print('A = ', A[0])
514            print('Iy = ', Iy[0])
515            print('W_top = ', W_top[0])
516            print('W_bot = ', W_bot[0])
517            print('f_ctd = ', f_ctd)
518            print('tensile stress at support [MPa] = ', sigma_top_p_crit)
519            if scenario=='A':
```

```python
520              print('UC_fck = ' , UC_fck, '\nUC_fcd = ', UC_fcd, '\nUC_fctd = ',
                    UC_fctd, '\nUC_shear = ', UC_shear, '\nUC_w = ', UC_w, \
521                  '\nUC_omega = ', UC_omega, '\nUC_li = ', UC_li, '\nM = ', M, '\nP = ',
                    P, '\nA_P = ', A_p,  '\nT = ', T, '\ne_p = ', e_p[0])
522          if scenario=='B':
523              print('UC_fck = ' , UC_fck, '\nUC_fcd = ', UC_fcd, '\nUC_M = ', UC_M,
                    '\nUC_P = ', UC_P,'\nUC_shear = ', UC_shear, '\nUC_w = ', UC_w, \
524                  '\nUC_omega = ', UC_omega, '\nUC_li = ', UC_li, '\nM = ', M, '\nP = ',
                    P, '\nA_P = ', A_p,  '\nT = ', T, '\ne_p = ', e_p[0])


527      if scenario=='A':
528          output =
                namedtuple('output','UC_fck,UC_fcd,UC_fctd,UC_shear,UC_w,UC_omega,UC_li,M,P,T,
                V_c,M_p,e_p,s_b_p,s_t_p,M_ULS,A_c,Iy,f1,f2,l_i')
529          return
                output(UC_fck=UC_fck,UC_fcd=UC_fcd,UC_fctd=UC_fctd,UC_shear=UC_shear,UC_w=UC_w
                ,UC_omega=UC_omega,UC_li=UC_li,M=M,P=P,T=T,V_c=V_c,M_p=M_p,e_p=e_p[0],\
530
                        s_b_p=sigma_bot_p[3][ms],s_t_p=sigma_top_p[3][ms],M_ULS=moments[
                        -1][ms],A_c=A[0],Iy=Iy[0],f1=f1,f2=f2,l_i=l_i)
531      if scenario=='B':
532          output =
                namedtuple('output','UC_fck,UC_fcd,UC_P,UC_M,UC_shear,UC_w,UC_omega,UC_li,M,P,
                T,V_c,M_p,e_p,s_b_p,s_t_p,M_ULS,A_c,Iy,f1,f2,l_i')

534          return
                output(UC_fck=UC_fck,UC_fcd=UC_fcd,UC_P=UC_P,UC_M=UC_M,UC_shear=UC_shear,UC_w=
                UC_w,UC_omega=UC_omega,UC_li=UC_li,M=M,P=P,T=T,V_c=V_c,M_p=M_p,e_p=e_p[0],\
535
                        s_b_p=sigma_bot_p[3][ms],s_t_p=sigma_top_p[3][ms],M_ULS=moments[
                        -1][ms],A_c=A[0],Iy=Iy[0],f1=f1,f2=f2,l_i=l_i)
```
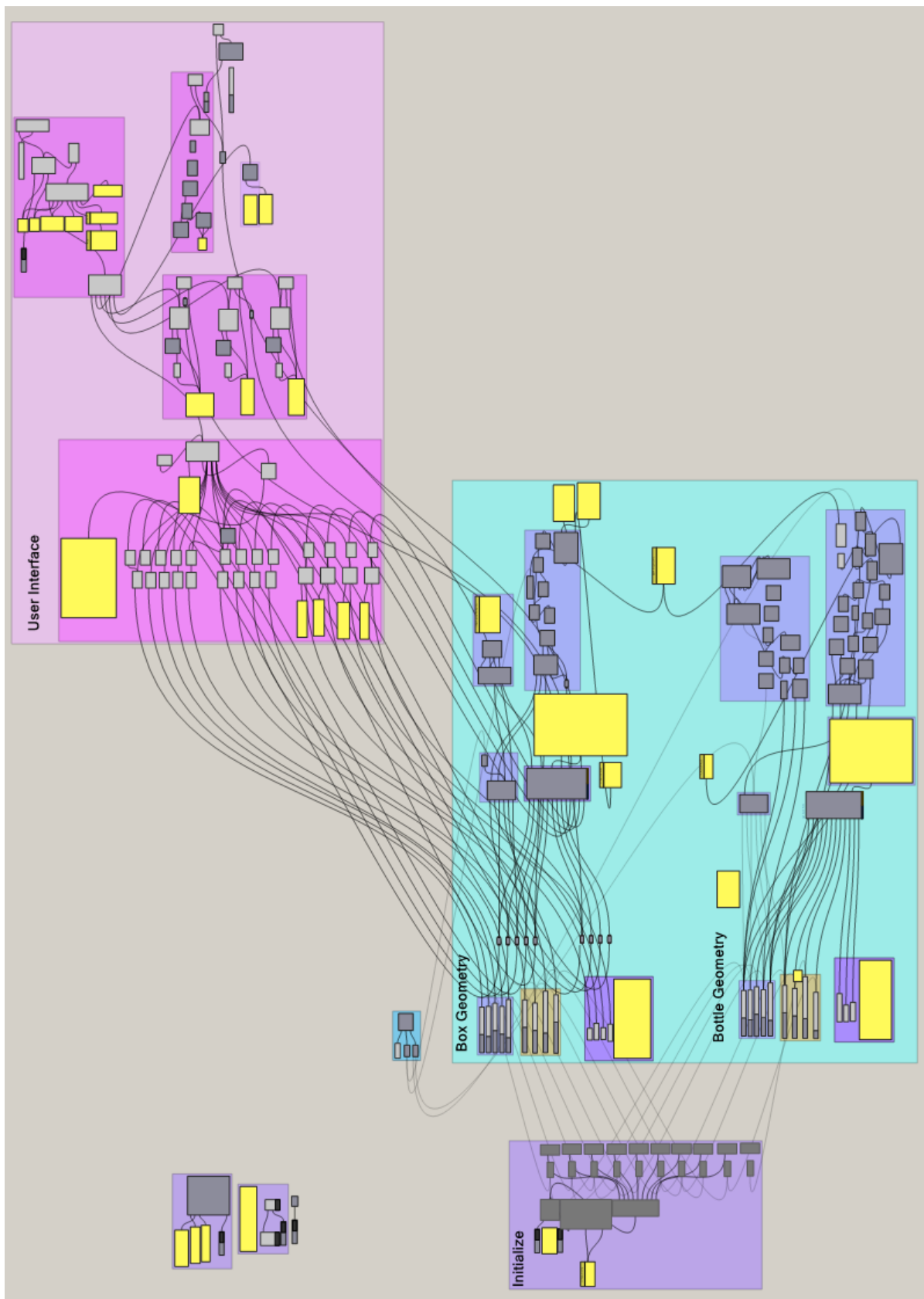
H.3. Grasshopper script

Figure H.1: Overview of Grasshopper script containing a geometry definition (in which the Python script is called) and the construction of the User Interface.